August 2020

Development of Solid Sampling Modalities for the Liquid-Sampling Atmospheric Pressure Glow Discharge Microplasma

Htoo Paing
Clemson University, Htoo2222@gmail.com

DEVELOPMENT OF SOLID SAMPLING MODALITIES FOR THE LIQUID-SAMPLING ATMOSPHERIC PRESSURE GLOW DISCHARGE MICROPLASMA

A Dissertation
Presented to
the Graduate School of
Clemson University

In Partial Fulfillment
of the Requirements for the Degree
Doctor of Philosophy
Chemistry

---

by
Htoo Wai Paing
August 2020

Accepted by:
R. Kenneth Marcus, Committee Chair
Jeffery Anker
George Chumanov
Brian Powell

ABSTRACT

Fast pretreatment of samples, low resource consumption, and high analytical throughput makes direct solid sampling techniques an attractive choice for a wide range of applications. Currently there are a plethora of analytical techniques capable of solid sampling. However, no commercial technique is available that is capable of taking advantage of the key concepts of solid samplings. General disadvantages amongst the current solid sampling instrumentation are high cost of operation, limited analyte choice, and reduced analytical performance. In that regard, it is important to develop a source that has low operation cost as well as the capability to analyze a diversity of analytes. An added benefit would be if the source is comparable in analytical performance to that of solution based instruments. One potential source is the liquid sampling – atmospheric pressure glow discharge (LS-APGD) microplasma that is utilized primarily for solution analysis.

The analytical merits of the LS-APGD overlaps with that of direct solid sampling. The LS-APGD provides a multi-faceted approach to analytical instruments by providing a variety of information from a compact ionization/excitation source. Unique amongst the tools in the analytical toolbox, the LS-APGD is capable of not only ionizing elements but also molecular species. Beyond that, the LS-APGD also operate in a total consumption mode, i.e no solvent waste, with solution flow rates under 100 µL min^{-1} as well as less than 1.0 L min^{-1} of helium gas flow. These analytical merits of low cost and abundance of information coincide with the key advantages of direct solid sampling. Presented in this dissertation is efforts on adding and improving solid sampling modalities to this ionization/excitation source. The dissertation discusses the influence of plasma parameters

on optical emission though ambient desorption as well as the implication of those trends on underlying mechanism. On the sample preparation side, an effective means of preparing residues for analysis via intelligent substrate choice as well as co-adding dopant is provided. Finally, two sampling methods coupled to the LS-APGD is described. A novel solvent extraction method for heat sensitive samples as well as coupling to a laser ablation system for comprehensive atomic, molecular, and spatial analysis.

DEDICATION

This dissertation is dedicated to my family and friends. This journey could not have been completed without their support. To my father, Myo Thwin, and my mother, Yin Mya, who through their own tough times never failed to go out of their way to give me comfort when I needed it most. To my sister, Marika Thwin, who never let me get too big for my own head. To my partner and personal grammar editor, Katja Hall, for putting up with me. Your love and support throughout these years is far more than I deserve.

To my friends Anthony Tipton, John Wilson, and Jordan Livingston. Thank you for teaching me that it's okay to let loose and enjoy life once in a while. To my friends Tony Scavuzzo and Morgan Lange. Thank you for reminding me that I should stop letting loose and get back to work. To my fellow student Lei Wang, for years of close friendship throughout my graduate student life. To Dr. Jian He for introducing me to scientific research growing single crystals and also for being a great role model on the soccer field.

I believe that we are a product of our environment and I'm forever grateful to be surrounded by loving, intelligent, and hardworking family and friends.

ACKNOWLEDGMENTS

I would like to acknowledge my research advisor Dr. R. Kenneth Marcus. Not only for the research opportunities but for teaching me to be a better researcher, scientist, writer, and critical thinker. He was tough to me when I needed it and kind to me when I needed it. His support and assistance were indispensable in my graduate career.

I would also like to thank my committee members Dr. Jeffery Anker, Dr. George Chumanov and Dr. Brian Powell for providing me with assistance in research as well as their encouragement and support throughout my graduate career.

Finally, I would like to acknowledge my past and current lab mates as well as graduate students from Dr. Anker and Dr. Chumanov's lab for years of camaraderie that made this journey possible.

TABLE OF CONTENTS

Page

LIST OF TABLES

LIST OF FIGURES

List of Figures (Continued)

Figure Page

List of Figures (Continued)

Figure Page

List of Figures (Continued)

Figure Page

CHAPTER I

INTRODUCTION

1.1 Introduction to solid sampling

Since the age of alchemy, the process of calcination and dissolution of matter was known to be the most burdensome step in the ambitious goal to create the philosopher's stone.[1] To this day, the process of digestion, dilution, and chemical separation as a precursor for analytical analysis of a sample is usually the rate-limiting step.[2-4] The digestion techniques typically require the use of caustic reagents and high energy sources. To complicate matters more, different digestion methods are required for a variety of sample types, whereby the employment of an incorrect method will lead to an unreliable or false analytical result. Of course, the use of digestion methods has its benefits. With the digestion of a sample, homogeneity is more readily achieved, and any individual injection is representative of the whole sample. However, by digesting the sample, all information regarding spatial distributions of analytes is lost. Even with the disadvantages of time, cost, and loss of information, liquid sampling techniques are at the forefront of trace and ultra-trace molecular and elemental analysis.

Techniques such as inductively coupled plasma (ICP) – mass spectrometry (MS)/ optical emission spectrometry (OES) and high-performance liquid chromatography (HPLC) – MS are considered the gold standard for both trace elemental and molecular analysis due to their unrivaled sensitivity. However, this sensitivity is offset by the fact that real-world samples are often digested then diluted. Direct solid sampling is a term given

for obtaining chemical information from a sample without the need for harsh chemical treatment and with little to no sample preparation.[3]

By eliminating the intensive sample preparation step, certain practical advantages are gained. In the solid sampling modalities, the speed of analysis is increased, less sensitivity from instruments are required, cost is reduced in terms of sample size and reagents used, and spatial information is retained.[5]

Whether it is the United States Food and Drug Agency testing foodstuffs for possible contaminates or a computer chip manufacturer determining the purity of their latest batch of silicon chips, the speed in which chemical information is obtained is of great importance. By eliminating lengthy digestion/pretreatment procedures, samples are analyzed, and results are obtained within minutes as opposed to hours. This advantage is further amplified by the fact that there is usually a shorter transit time from the sample to the detector. In the case of portable instruments, the instrument can be taken to the sample thus the sample collection and transport processes are eliminated. Increasing speed of analysis even further.

Additionally, because sample is not diluted in the preparation process, solid sampling can take full advantage of highly sensitive detectors. Alternatively, solid sampling allows the utilization of a less sensitive, more economical instrument while to obtaining the necessary information.

Because solid sampling is a direct measurement without transport, the addition of reagents, or waste generation[3], solid sampling fits the criteria for “ideal” green chemistry. The retainment of analytes during sampling also makes the technique a logical choice for

samples that are difficult to acquire. While the major advantage of aqueous analysis is the confidence in homogeneity of the sample, real samples are rarely homogeneous. In fact, the knowledge of both chemical and spatial information is becoming increasingly important due to the substantial insight into function and failures about various systems brought about by this information.[6] Mapping/imaging has provided insight into everything from our biological understanding[7, 8] to the function of electronics.[9, 10] Uniquely, solid sampling is capable of providing this information.

1.2 Brief overview of current solid sampling techniques

The previously described advantages of solid sampling have led to the development of multiple traditional analytical techniques designed to directly sample solids. Techniques such has arc/spark OES,[11] glow discharge (GD)[12], and x-ray fluorescence (XRF)[13] can provide elemental information directly from solid samples. Meanwhile, techniques such as Raman spectroscopy,[14] desorption electrospray ionization (DESI)[15] and direct analysis in real-time (DART) – MS[16] provide molecular information from solid samples. Along with analytical techniques that are developed for solid sampling, recent development in instrumentation, particularly those of laser ablation (LA), have allowed for the advancement of solid sampling modalities to be added to the traditionally liquid sampling instruments such as LA-ICP-OES/MS,[17, 18] and LA-electrospray ionization (ESI).[19] As with all analytical techniques, those previously mentioned all have their share of advantages and disadvantages.

1.2.1 Elemental solid sampling techniques

Arc/spark OES has long been utilized for direct analysis of solid samples. The ablation of sample is carried out by an electrical discharge between an electrode and the conducting material. While this technique has practical capabilities such as multielement determination in less than 30 s,[20] it has fallen to the wayside to techniques such as ICP-OES/MS.[2] When compared with ICP based techniques, the analytical performance of arc/spark sources is significantly worse. Arc/spark ablation can be used as sample introduction for ICP-OES/MS; however, LA and GD sources have better reproducibility. Even so, arc/spark ablation is utilized routinely in the metallurgical industry due to its low cost and maintenance requirements when compared to other systems such as LA.[2]

GD sources, paired with OES or MS, have been considered powerful and versatile tools for the analysis of bulk, surface, and interface analysis.[21] Historically, this technique was also limited to conducting samples but recent development in radio frequency (rf) power has allowed GD sources to analyze nonconductive surfaces such as organic coatings.[12] New developments in instrumentation such as atmospheric pressure glow discharges have extended the analytical portfolio of this classic instrument. Low power, mechanical ruggedness, sample diversity i.e. bulk and trace, and quality of data produced make these devices an attractive choice for solid sampling. A major benefit of GD sources is the capability to analyze samples in an atomic "layer-by-layer" manner, allowing for depth profiling of solids. Of course, GD plasmas are not without disadvantages. Non-flat samples cannot be directly mounted onto GD devices and require special extensions.

Beyond that, GD-OES/MS has limited lateral resolution and miniaturization for solid sampling remains difficult due to vacuum requirements.

XRF techniques can be a quick and efficient method of solid sampling. A wide range of different techniques are available such as wavelength dispersive (WD)-XRF, energy dispersive (ED)-XRF, total reflection (T)XRF, and micro (μ)XRF, with each having its own degree of instrument complication, size, and analytical capability. The main advantage of all XRF techniques is the capability to analyze samples non-destructively and without generating any solvent waste. XRF is routinely utilized in all fields where fast profiles of metallic and nonmetallic constituents are of value.[3] For field-based studies where ease of use and high throughput is desired, portable XRF can also be purchased. Among the main disadvantages of XRF are the higher limit of detection, limited elemental choice, and influences from the matrix effects.

LA techniques include the likes of laser-induced breakdown spectroscopy (LIBS), LA-ICP-MS, and LA-ICP-OES. Simply described, in LA techniques a pulsed laser beam is guided by mirrors and lenses onto the sample surface. In the case of LIBS, photons emitting from the ablated sample are measured directly from the surface. The ablated mass can also be transported toward an ICP by a carrier gas where either ions or photons are analyzed, as is the case for LA-ICP-MS/OES. In terms of direct solid sampling analytical performance, LA techniques are highly regarded for their low LOD, and high spatial resolution. LIBS and LA-ICP-MS/OES have been routinely used for elemental analysis of everything from silicon wafers[22] to bioimaging of animal tissues.[23] Still, LA techniques are

not utilized routinely due to the strong influence of the laser-surface interaction on analytical response.

1.2.2 Molecular solid sampling techniques

Raman spectroscopy is a powerful technique capable of identifying a variety of molecules based on their Raman spectra. In Raman spectroscopy, monochromatic radiation is focused onto a sample and the Raman shift measured. Today, Raman instrumentation can detect molecules down to ppm levels in matter of minutes. Alternatively, less sensitive, portable instrumentations can also be purchased. Due to the non-destructive nature of Raman spectroscopy, it is often utilized in the surface analysis of artworks. Raman spectroscopy can provide information about the authenticity of the art as well as a previous restoration effort.[24] Along with its non-destructive nature, Raman spectroscopy also requires a small mass of samples, reducing cost. The low intensity of Raman scattering with potential fluorescence from background molecules often leads to low sensitivity in the instruments. Also, the technique is limited to non-metal containing molecules.

For analyzing samples from their native environment spray-based ambient desorption ionization (ADI) techniques, such as DESI, have been widely utilized. In DESI, charged solvent droplets are generated by forcing solvent though a small capillary while a high electric potential is applied to the capillary. These charged droplets are then diverted towards the sample where they desorb, transport, and ionize analytes from the sample surface. While the exact mechanism for sampling and ionization is unknown, it is theorized to be a two-step process.[25] First, the surface of the sample is prewetted by initial solvent droplets from DESI. Second, subsequent droplets impact the analyte-solvent layer and

generate droplets with the dissolved analytes. Ionization is believed to have occurred due to either charge transfer or proton donation. DESI is a widely utilized ambient ionization technique for surface analysis due to its capability to ionize analytes in their native conditions. Both small and large molecules can be analyzed with similar sensitivity to those of conventional ESI. The analytical response from DESI is heavily reliant on the angles between the source, the sample, and the mass spectrometer inlet.[25] Due to this reliance, rough surfaces tend to generate irreproducible results.

Another ambient molecular detection technique is the plasma-based DART. In DART, long-lived excited-state neutral atoms and molecules are generated in the afterglow region of a plasma away from the sample. Once these atoms and molecules are generated in the DART source, they initiate Penning ionization of N_2, water and other atmospheric molecules which then ionizes the analytes desorbed from the sample surface. This type of ionization has been performed on a variety of surfaces from human skin[26] to concrete.[27] The capability of DART to characterize both polar and nonpolar organic compounds means it is routinely employed for real-time analysis reaction monitoring in drug discovery.[28] Due to the thermal nature of the desorption mechanism, only small molecules (< ~1 kDa) can be sampled by DART.

For analysis of larger organic molecules, matrix-assisted laser desorption ionization (MALDI) – MS is traditionally utilized. Here a matrix, which must absorb at the laser wavelength, is either sprayed on top of the sample or mixed together. The laser energy is absorbed by the matrix which causes the matrix and the solid sample to evaporate into the gas phase. In this phase, the matrix is a mixture of neutral molecules and ions. The gas-

phase analytes are then typically ionized though proton transfer and/or cation/anion transfer.[29] Similar in many respects to LA-ICP-MS, MALDI-MS is a highly sensitive instrument capable of low detection limits and high spatial resolution. MALDI-MS has been used determine not only molecular information but also the distribution of molecules for various applications.[30,31] Compared to other solid sampling techniques MALDI requires intensive sample preparation and is costly to operate in terms of resource consumption.

Presented in this dissertation are various solid sampling modes coupled to a microplasma source that is capable of excitation of atoms as well as ionization of atoms and molecules.

1.3 The liquid sampling - atmospheric pressure glow discharge microplasma

The idea of solid sampling is based around the key concepts of low resource consumption, ease of use, and abundance of information from the analysis. In that regard, the variety of analytical techniques provided in the previous section fail to take full advantage of direct solid sampling. Common weaknesses among them are the cost of operation (i.e. LA-ICP-MS, MALDI), narrow choice of analyte (i.e. XRF, Raman), and reduced analytical performance (arc/spark, DESI). Not only that, but current solid sampling also be categorized into either elemental or molecular analysis. Thus, to obtain complete information, one must use multiple techniques. This is in conflict with one of the tenants of solid sampling which is to reduce resource consumption. In that respect, it would be ideal to have an instrument capable of simultaneously obtaining elemental and molecular

information, while not sacrificing other important concepts of solid sampling such as low cost and ease of use.

Towards this end, atmospheric pressure glow discharge (APGD) plasmas appear to be an attractive option due to its low cost, ruggedness, and ease of use.[32] Many APGD sources are based upon an initial design by Cserfalvi and Mezei called electrolyte-as-cathode discharge (ELCAD).[33] One source in particular, the liquid sampling (LS)-APGD developed by Marcus and Davis,[34] is fit for solid sampling. Initially developed as an elemental excitation source for OES, the LS-APGD has expended its capability toward elemental and organic MS. The LS-AGPD microplasma, ~ 2 mm in length, is sustained between a metal counter electrode and an electrolyte solution electrode. The LS-APGD configuration utilized in MS modalities is shown in Fig 1.1. Unlike the ELCAD designs,[35, 36] the LS-APGD operates in total-consumption mode (no liquid waste). This advantage coincides with waste reduction by solid sampling. Finally, the LS-APGD is proven capable of analyzing a wide range of analytes from isotopes[37] to proteins.[38] The diversity of accessible analyte combined with its low cost, and low resource consumption makes it a logical choice for direct solid sampling development.

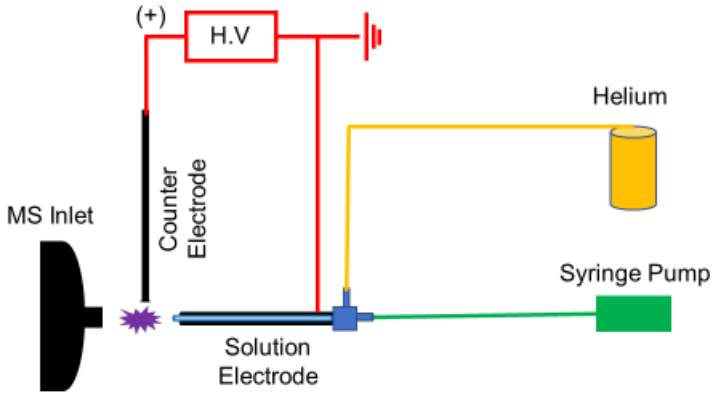

Figure 1.1 The LS-APGD ion source for analysis of aqueous sample - mass spectrometry.

The LS-APGD was previously utilized as an ADI-MS source for molecular analysis from surfaces.[39] To change the mode of operation from liquid sampling MS to ADI-MS, the solution cathode is angled towards the sample as seen in Fig. 1.2. This mode of the LS-AGPD was mounted onto a Thermo Finnigan LCQ Advantage MAX without modifications to the instrument outside of removing the ESI source. The initial work describes the influence of plasma parameters on analytical response of caffeine residues. Described in the aforementioned paper is the importance of source geometry for the analysis of solid sample. The versatility of the source is shown here through the analysis of organic molecules from green tea extracts, coffee beans, dried tobacco leaves, an analgesic tablet, and paper currency. This diversity also indicates that perhaps the ADI-LS-APGD is less sensitive towards surface topography than other spray sources such as DESI. In its ADI-MS application, the source's ionization mechanism appears to be a combination of electrospray ADI sources (DESI) and plasma-based ADI sources (DART) whereby

solvent droplet, thermal energy and kinetic energy desorb analytes off of a surface and analytes are ionized through proton transfer, Penning ionization and ion adducts.

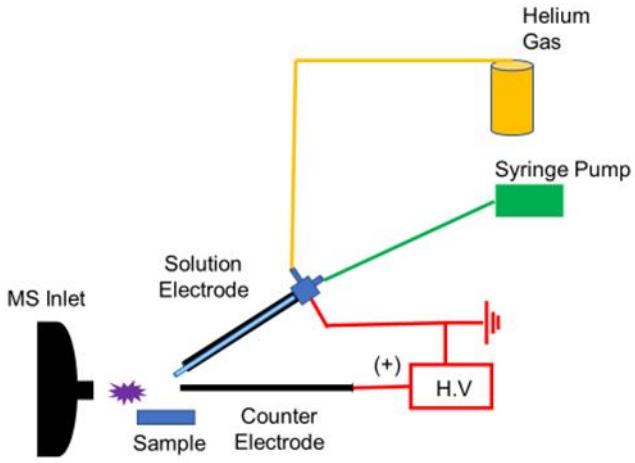

Figure 1.2 The LS-APGD ion source for ADI-MS of solid samples.

Unique to the LS-APGD, the concept of ambient desorption OES has been described by Marcus *et al.* for elemental analysis.[40] Optical methods have an advantage of instrument simplicity, lower cost of operation, and portability when compared to those of mass spectrometric analysis. In this proof-of-concept work, the LS-APGD was used to volatilize and excite copper, nickel, and silver from diverse sample forms (metallic thin films, dried solution residues, and bulk metals). Emissions were detected from natural atoms. The photons emitted from the plasma were analyzed via a bench-top monochromator with a photomultiplier tube. While the work was qualitative in nature, it shows a high signal to background ratio (~ 2 orders of magnitude) particularly when analyzing copper and silver thin films.

The LS-AGPD-OES has also been utilized as alternative to an ICP in the detection of laser-produced particles for elemental analysis. In this modality, the LS-APGD utilizes

a similar geometry to those used for liquid sampling OES analysis. Here, the counter electrode and the solution electrode are 180° with respect to each other as shown in Fig. 1.3. A hollow counter electrode was used as a means of introducing laser-ablated particles into the plasma via helium as a carrier gas.[41] In the manuscript by Quarles *et al.*, the plasma source was optimized utilizing a one-variable at a time method. Afterward, a brass sample with a known ratio of zinc to copper was analyzed and results were compared to that of LIBS. The intensity ratios of Zn(I) to Cu(I) was found to be linear with the elemental composition ratios of the brass sample for both LA-LS-APGD-OES and LIBS. Furthermore, the Zn(I) and Cu(I) intensity trends were found to be similar to those reported by LA-ICP-MS method.[42] This work demonstrated that LA-LS-APGD-OES is comparable to other, more established LA methods while requiring less capital and lower resource consumption.

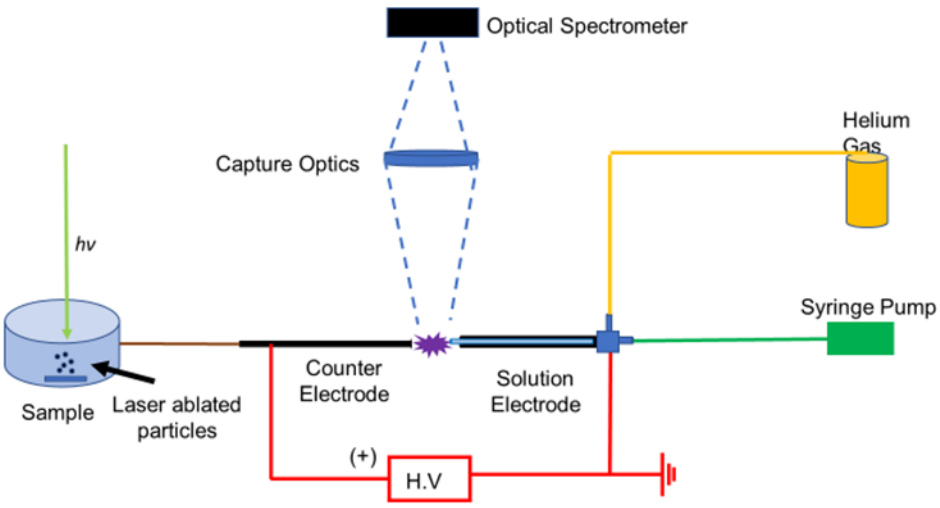

Figure 1.3 The LS-APGD ion source for LA-OES of solid samples.

A comprehensive design-of-experiment (DoE) was utilized by Manard *et al*. to further study the influence of plasma parameters on the emission response and the plasma's robustness upon laser ablation particle introduction.[43] Influence of various plasma parameters, such as discharge current, helium carrier gas flow rate, and electrode separation distance on Cu(I) emission intensities was studied. The best emission responses were detected at high-discharge currents, low helium carrier gas flow, and small interelectrode gaps. In that work the rotational temperature was determined via emission from the N_2 molecular emission band and the robustness value of the plasma was determined as a ratio of Mg(II) to Mg(I). While the introduction of strontium and calcium particles results in a slight increase of rotational temperature from ~1000 K to ~1200 K, the introduction of strontium and calcium does not affect the robustness of the plasma in an appreciable manner. It does appear though, that the introduction of calcium slightly improves the ionization power of the plasma. The authors attribute the immunity of the LS-APGD from LA particle-induced matrix effects to the long residence times and high-power densities (10 W mm^{-3}) of the LS-APGD.

Laser ablated particles can also be ionized by the LS-APGD for elemental analysis as described by Carado *et al*.[44] Here, 100 nm particles produced by a femtosecond laser were carried by argon carrier gas towards the LS-APGD where it is atomized then ionized. The LS-APGD was configured in a similar manner to those of aqueous sample MS analysis. The solution and counter electrode were placed at 40° relative to each other due to the change in the aerodynamic flow brought about by the introduction of the carrier gas. Mass analysis was performed by an orbitrap mass analyzer. Oxygen free copper shard,

solder, and a one-cent U.S. coin were sampled. Copper was detected in all samples, while zinc was also detected in the U.S. coin and lead and tin were detected in solder. The 10 µm copper cladding was resolvable from the zinc core during a depth-profile experiment of the U.S. coin. This shows the diversity of applications for the LS-APGD. The various plasma condition for the different LS-APGD modalities are summarized in Table 1.1.

The unique capability of the LS-APGD to perform elemental AD-OES has not been emulated by other sources at the time of this writing. This mode was progressed further through investigation of current, interelectrode gap, sample displacement, angle of incidence, sheath gas flow rate, counter gas flow rate, electrolyte solution flow rate, and optical sampling position on analytical response as presented in Chapter 2. A means of improving the plasma sensitivity for AD-OES from metal residues through improved matrix choice as determined by DoE is presented in Chapter 3. In the case where the AD modality causes samples to burn and LA methods are too time-consuming; a novel solvent extraction method can be coupled and is presented in Chapter 4. Presented in Chapter 5 is description of the LA-LS-APGD for comprehensive analysis, where atomic, molecular and spatial information can be acquired from a single technique. For the improvement of the solution mode LS-APGD-OES, a method of excluding ambient atmosphere is presented in Chapter 6.

Table 1.1 Plasma operating parameters for different LS-APGD modalities. Organic (molecular) analysis[a] .Angle is between electrode and sample surface[b]. Counter gas flow is the carrier gas[c]. Argon gas[d].

LS- APGD Modality	Solution Identity	Solution Flow Rate ($\mu L\ min^{-1}$)	Electrode Angle (°)	Counter Gas Flow Rate ($L\ min^{-1}$)	Sheath Gas Flow Rate ($L\ min^{-1}$)	Electrode Gap (mm)	Current (mA)
Solution – OES [45]	5% HNO_3	25	180	0.3	0.6	2	60
Solution – MS [46]	2% HNO_3	25	90	0.0	0.2	1	30
Solution – MS[a] [38]	70:30 MeOH:H_2O	15	90	0.0	0.7	N/A	15
AD – OES[b] [47]	5% HNO_3	100	70	0.2	0.7	4	60
ADI – MS[ab] [39]	~ 5% HNO_3	30	30 - 40	0.0	0.0011	~ 1	15
LA – OES[c] [41]	5% HNO_3	10	180	0.3	0.3	~ 1 - 2	60
LA – MS[bcd] [44]	5% HNO_3	10	40	1.0	1.0	~ 1	18

1.4 List of publications

The following chapters in this dissertation are based on these papers:

Chapter II: Reproduced from Ref. H. W. Paing and R. K. Marcus, J. Anal. At. Spectrom., 2017, 32, 931 with permission from The Royal Society of Chemistry

Chapter III: Reproduced from Ref. H. W. Paing and R. K. Marcus, *Analyst*, 2018, **143**, 1417 with permission from The Royal Society of Chemistry

Chapter IV: Reproduced with permission from Ref. H.W.Paing, B.T. Manard, B.W. Ticknor, J. R. Bills, K.A. Hall, D.A. Bostick,P. Cable-Dunlap, R. K. Marcus, *Anal. Chem.* 2020, 92, 12,8591-8598. Copyright 2020 American Chemical Society.

Chapter V: In preparation with intent to submit to *Analytical Chemistry*.

Chapter VI: Reproduced from Ref. H. W. Paing, K. A. Hall, and R. K. Marcus, *Spectrochim Acta B*, 2019, **155**, 99 with permission from Elsevier

1.5 References

1. M. A. Belarra, M. Resano, F. Vanhaecke and L. Moens, *Trac-Trend Anal. Chem.*, 2002, **21**, 828-839.
2. C. Bendicho, I. Lavilla, F. Pena-Pereira and V. Romero, *J. Anal. At. Spectrom.*, 2012, **27**, 1831-1857.
3. R. C. Machado, D. F. Andrade, D. V. Babos, J. P. Castro, V. C. Costa, M. A. Speranca, J. A. Garcia, R. R. Gamela and E. R. Pereira, *J. Anal. At. Spectrom.*, 2020, **35**, 54-77.
4. M. de la Guardia, in *Green Analytical Chemistry*, 2011, **ch. 4**, pp. 59-86.
5. C. Petibois, *Anal. Bioanal. Chem.*, 2010, **397**, 2051-2065.
6. L. Jolivet, M. Leprince, S. Moncayo, L. Sorbier, C. P. Lienemann and V. Motto-Ros, *Spectrochim. Acta B*, 2019, **151**, 41-53.
7. B. Busser, S. Moncayo, J. L. Coll, L. Sancey and V. Motto-Ros, *Coordin. Chem. Rev.*, 2018, **358**, 70-79.
8. C. G. Weisener and T. Reid, *Surf. Interface. Anal.*, 2017, **49**, 1416-1421.
9. M. Wolf, B. M. May and J. Cabana, *Chem. Mater.*, 2017, **29**, 3347-3362.
10. A. Flessa, E. Ntemou, M. Kokkoris, E. Liarokapis, M. Gloginjic, S. Petrovic, M. Erich, S. Fazinic, M. Karlusic and K. Tomic, *J. Raman. Spectrosc.*, 2019, **50**, 1186-1196.
11. Z. D. Zhou, K. Z. Zhou, X. D. Hou and H. Luo, *Appl. Spectrosc. Rev.*, 2005, **40**, 165-185.
12. J. Pisonero, J. M. Costa, R. Pereiro, N. Bordel and A. Sanz-Medel, *Anal. Bioanal. Chem.*, 2004, **379**, 17-29.
13. M. West, A. T. Ellis, C. Streli, C. Vanhoof and P. Wobrauschek, *J. Anal. At. Spectrom.*, 2017, **32**, 1629-1649.
14. R. S. Das and Y. K. Agrawal, *Vib. Spectrosc.*, 2011, **57**, 163-176.
15. D. R. Ifa, C. P. Wu, Z. Ouyang and R. G. Cooks, *Analyst*, 2010, **135**, 669-681.
16. J. H. Gross, Anal Bioanal Chem, 2014, 406, 63-80.
17. D. Oropeza, J. Gonzalez, J. Chirinos, V. Zorba, E. Rogel, C. Ovalles and F. Lopez-Linares, *Appl. Spectrosc.*, 2019, **73**, 540-549.
18. D. Pozebon, G. L. Scheffler and V. L. Dressler, *J. Anal. At. Spectrom.*, 2017, **32**, 890-919.
19. J. K. Roman, C. M. Walsh, J. Oh, C. E. Dana, S. Hong, K. D. Jo, M. Alleyne, N. Miljkovic and D. M. Cropek, *Anal. Bioanal. Chem.*, 2018, **410**, 1911-1921.
20. V. B. E. Thomsen and J. L. Spencer, *Spectroscopy-Us*, 2011, **26**, 18-21.
21. B. Fernandez, R. Pereiro and A. Sanz-Medel, *Anal. Chim. Acta*, 2010, **679**, 7-16.
22. C. K. Yang, P. H. Chi, Y. C. Lin, Y. C. Sun and M. H. Yang, *Talanta*, 2010, **80**, 1222-1227.
23. E. Moreno-Gordaliza, C. Giesen, A. Lazaro, D. Esteban-Fernandez, B. Humanes, B. Canas, U. Panne, A. Tejedor, N. Jakubowski and M. M. Gomez-Gomez, *Anal. Chem.*, 2011, **83**, 7933-7940.
24. K. S. Andrikopoulos, S. X. Daniilia, B. Roussel and K. Janssens, *J. Raman Spectrosc.*, 2006, **37**, 1026-1034.

25. D. J. Weston, *Analyst*, 2010, **135**, 661-668.
26. A. Mess, B. Enthaler, M. Fischer, C. Rapp, J. K. Pruns and J. P. Vietzke, *Talanta*, 2013, **103**, 398-402.
27. R. B. Cody, J. A. Laramee and H. D. Durst, *Anal. Chem.*, 2005, **77**, 2297-2302.
28. C. Petucci, J. Diffendal, D. Kaufman, B. Mekonnen, G. Terefenko and B. Musselman, *Anal. Chem.*, 2007, **79**, 5064-5070.
29. M. Karas and R. Kruger, *Chem. Rev.*, 2003, **103**, 427-439.
30. L. J. Sparvero, A. A. Amoscato, C. E. Dixon, J. B. Long, P. M. Kochanek, B. R. Pitt, H. Bayir and V. E. Kagan, *Chem. Phys. Lipids*, 2012, **165**, 545-562.
31. J. Nakamura, T. Morikawa-Ichinose, Y. Fujimura, E. Hayakawa, K. Takahashi, T. Ishii, D. Miura and H. Wariishi, *Anal. Bioanal. Chem.*, 2017, **409**, 1697-1706.
32. J. A. C. Broekaert and K. G. Reinsberg, *Spectrochim. Acta B*, 2015, **106**, 1-7.
33. P. Mezei and T. Cserfalvi, *Appl. Spectrosc. Rev.*, 2007, **42**, 573-604.
34. R. K. Marcus, B. T. Manard and C. D. Quarles, *J. Anal. At. Spectrom.*, 2017, **32**, 704-716.
35. M. R. Webb and G. M. Hieftje, *Anal. Chem.*, 2009, **81**, 862-867.
36. A. J. Schwartz, S. J. Ray, E. Elish, A. P. Storey, A. A. Rubinshtein, G. C. Y. Chan, K. P. Pfeuffer and G. M. Hieftje, *Talanta*, 2012, **102**, 26-33.
37. E. D. Hoegg, C. J. Barinaga, G. J. Hager, G. L. Hart, D. W. Koppenaal and R. K. Marcus, *J. Am. Soc. Mass. Spectr.*, 2016, **27**, 1393-1403.
38. L. X. Zhang and R. K. Marcus, *J. Anal. At. Spectrom.*, 2016, **31**, 145-151.
39. R. K. Marcus, C. Q. Burdette, B. T. Manard and L. X. Zhang, *Anal. Bioanal. Chem.*, 2013, **405**, 8171-8184.
40. R. K. Marcus, H. W. Paing and L. X. Zhang, *Anal. Chem.*, 2016, **88**, 5579-5584.
41. C. D. Quarles, J. Gonzalez, I. Choi, J. Ruiz, X. L. Mao, R. K. Marcus and R. E. Russo, *Spectrochim. Acta B*, 2012, **76**, 190-196.
42. O. V. Borisov, X. L. Mao, A. Fernandez, M. Caetano and R. E. Russo, *Spectrochim. Acta B*, 1999, **54**, 1351-1365.
43. B. T. Manard, J. J. Gonzalez, A. Sarkar, M. R. Dong, J. Chirinos, X. L. Mao, R. E. Russo and R. K. Marcus, *Spectrochim. Acta B*, 2014, **94-95**, 39-47.
44. A. J. Carado, C. D. Quarles, A. M. Duffin, C. J. Barinaga, R. E. Russo, R. K. Marcus, G. C. Eiden and D. W. Koppenaal, *J. Anal. At. Spectrom.*, 2012, **27**, 385-389.
45. K. A. Hall and R. K. Marcus, *J. Anal. At. Spectrom.*, 2019, **34**, 2428-2439.
46. T. J. Williams and R. K. Marcus, *J. Anal. At. Spectrom.*, 2019, **34**, 1468-1477.
47. H. W. Paing and R. K. Marcus, *J. Anal. At. Spectrom.*, 2017, **32**, 931-941.

CHAPTER II

PARAMETRIC EVALUATION OF AMBIENT DESORPTION OPTICAL EMISSION SPECTROSCOPY UTILIZING A LIQUID SAMPLING-ATMOSPHERIC PRESSURE GLOW DISCHARGE MICROPLASMA

2.1 Abstract

An evaluation of the parametric dependence of emission responses for ambient desorption optical emission spectroscopy utilizing a liquid sampling-atmospheric pressure glow discharge (AD-OES-LS-APGD) microplasma is described. The influence of optical sampling position, acid type, sample matrix, solution flow rate, discharge current, sample displacement, angle of solution electrode interelectrode separation, and gas flow rates on the emission response of copper as the model matrix and analyte are investigated. The type of acid plays a major role in the emission response of copper suggesting a possible reaction based desorption process on the surface of the sample. The physical make-up of the matrix (bulk or thin film) has no major effect on the emission response. The incidence angle between the solution electrode and the target surface is shown to have a major influence on emission response, indicating that the momentum of the sheath gas plays some role in desorption or transport of vaporized material to the plasma. There is positive correlation between solution flow rate, electrode distance, and emission response while only a minor emission dependence is seen from sheath gas flow rate. A region of intense emission is observed in spatial profiling experiments. Further development will be directed towards a field deployable ambient source for analysis of solid samples with no requirement of sample preparation

2.2 Introduction

The development of miniaturized sources for elemental analysis that are operated in real time have received significant interest over the past couple of decades, not only in terms of instrumentation but also sample preparation.[1–3] Compact and portable instruments with lower operating costs for analysis of remote or online samples are needed. Miniaturization of an analytical instrument (with the target size range of a suitcase or a book bag), would allow the instrument to be brought to the sample instead of the sample to the instrument. This is especially useful in cases where transport of the sample to the laboratory is too dangerous or time consuming based on the analytical challenges. Along with miniaturization, ambient desorption/ionization (ADI) sources have also been an active field with the target being the capability to analyze materials in their native form, without manipulation of the sample.[4,5] As a complementary pair, miniaturized instrumentation and ADI methods of sampling and analysis offer great advantages for those applications where sample perturbation can occur from manipulation, transport, and storage. There are a multitude of ADI sources that are mentioned in literature for ambient sample analysis.[6,7] The most developed of these approaches have been desorption electrospray ionization (DESI)[8] and direct analysis in real-time (DART).[4] The former is a variant on the common ESI-MS approach used in organic mass spectrometry (MS), while the latter is one of many forms of electrical discharges that have been applied in ADI-MS.[9] Furthermore, these approaches have primarily focused on the ionization of molecular species desorbed from a surface. Many applications of these devices are seen in fields for pharmaceuticals, agricultures, and forensics. As a practical matter, it may be advantageous in some instances

of in-field elemental analysis that optical emission spectroscopy (OES) would be preferable over mass spectrometry. To our knowledge, none of the aforementioned ADI-MS sources has been applied for elemental/atomic MS analysis, neither has any been shown applicable to OES analysis. As a matter of principle, laser-induced breakdown spectroscopy (LIBS) provides for solid sampling without the need for sample manipulation.[10,11] Modern laser technology allows for miniaturization of LIBS instrumentation,[12] with hand-held systems now commercially available. In many respects, though, the use of laser sampling may be too returned, as the analysis is absolutely defined by the precise location of the laser/surface interaction. The analysis of solution residues and powders/particulates requires the overhead of imaging optics.

Turning back to the concept of using plasma-based devices for AD analysis, there are indeed a plethora of miniaturized plasmas applied solely for the analysis of liquid samples by OES.[13,14] In general, these sources operate on a united concept of a liquid electrolyte carrier of the sample into an ambient atmosphere plasma operating in the glow discharge (GD) regime. These sorts of devices achieve improvements in terms of the size scale of the source as well as the supporting utilities versus the laboratory standard inductively-coupled plasma (ICP). The Clemson University laboratory has substantially developed one such spectrochemical source, the liquid sampling-atmospheric pressure glow discharge (LS-APGD) microplasma. The LS-APGD operation differs in some substantive ways from the other devices, as recently reviewed.[15] The breadth of application is its most remarkable feature as samples can be introduced in either the solution, gaseous, or particle phases, with laser ablation sampling[16,17] employed to generate the particulate aerosols. While initially

developed for OES analysis,[18,19] the microplasma has also been employed as an ionization source for both elemental[20,21] and molecular[22,23] species MS, a completely unique feature among the various GD microplasma and ADI-MS sources. In an effort to map out additional sampling modalities, the LS-APGD was shown to be viable approach for ADI-MS molecular analysis.[24] In that mode, the microplasma is simply placed 1–2 mm above the target surface (either a solid or a solution residue), directed downward toward the surface, and the product ions sampled by the vacuum into the mass spectrometer. In these cases, mass spectra representative of the original elemental/ molecular sample composition were readily obtained. Keeping in mind the objectives of a field-deployable elemental analysis instrument, the small footprint, low weight, and low operational overhead, and sampling diversity of the LS-APGD suggests many options. The ability to be interfaced to various OES/MS detectors is also an advantage. To that end, the concept of ambient desorption-optical emission spectroscopy was recently demonstrated using the microplasma, AD-LS-APGD-OES.[25] The potential scope of application was demonstrated for bulk metals, metallic thin films formed via vapor deposition, and solution residues. Surely the advancement of a technique capable of analyzing various surfaces with little sample preparation warrants further investigation. The present article focuses on the effects of different operational parameters on the intensity of analyte emission responses in hopes to better understand the cumulative mechanisms of how analyte is desorbed from the surface, transported into the excitation volume, and analytical signals generated. While the previous efforts illustrated the capacity to desorb a variety of metals,[25] emphasis here is on metallic copper as a means of focusing solely on the plasma effects, separate from matrix

induced interferences. Presented here are the effects of optical sampling position, acid type, sample matrix form, solution flow rate, discharge current, sample displacement, angle of solution electrode interelectrode separation, and gas flow rates for a bulk copper target. The effect of these parameters on the intensity provides insight into the operable mechanisms and allows initial optimization of the source. While much work is necessary for quantitative analysis utilizing the AD-OES-LS-APGD, the potential utility of the system as part of a field-deployable platform suggests that greater development is warranted.

2.3 Materials and methods

2.3.1 Instrumentation

The design of the AD-OES-LS-APGD has little in variation in terms of components from the previous ADI-MS and AD-OES implementations.[24,25] Depicted in Fig. 2.1 a, the plasma is sustained between two 500 mm i.d. x 700 mm o.d. stainless steel capillaries. The solution electrode also houses a 75 μm i.d. x 125 mm o.d. fused silica capillary which protrudes 1 mm from the end. Electrolytic solution is pumped through the silica capillary to sustain the plasma discharge due to its conductivity, with the solution serving as the anode (though grounded) in the diode GD geometry. The solution is transported via a syringe pump (NE1000, New Era Pump System, Inc., Farmington, NY) and the discharge is sustained via a Bertan Model 915 series power supply (Hickville, NY) operating in a constant current mode of 45 mA. A 10 kΩ ballast resistor is placed in series between the supply output with the powered counter electrode, which serves as the cathode. Helium sheath gas flows between the steel and fused silica capillaries for the solution electrode and

through the steel capillary forming the counter electrode. The parameters investigated in this study were rate of electrolyte solution flow, the rates of sheath/ counter gas flows, solution electrode-to-counter electrode separation distance, solution electrode-to-sample distance, lens focus point, electrolytic solution type, and electrode angle dependencies. The initial operational parameters, based on the initial communication,[25] were a 70° solution electrode pitch relative to the sample, a solution capillary-to-counter electrode separation of 2 mm, a displacement of the sample surface 2 mm below the solution capillary tip, 0.7 L min^{-1} sheath gas flow, 0.2 L min^{-1} counter electrode gas flow, and 50 mL min^{-1} electrolyte solution flow rate. Optical sampling involved focusing of the plasma region near the counter electrode onto the spectrometer entrance slit. A CVI Laser (Albuquerque, NM) Digikrom 240 0.24 monochromator system equipped with a Hamamastsu (Bridgewater, NJ) R928 photomultiplier tube (PMT) was used to obtain optical emission spectra. CVI Spectra AD III software, acquired from Spectral Products (Putnam, CT), was used to control the functions of both the monochromator and the PMT. The emission from the source was focused onto the a 50 mm-wide entrance slit of the monochromator by a 75 mm focal length fused quartz lens. Spectral scans were performed at a rate of 100 nm min^{-1}, with a signal integration time of 6 ms per 0.01 nm wavelength step. All optical transient measurements were assimilated at a rate of 10 points per second.

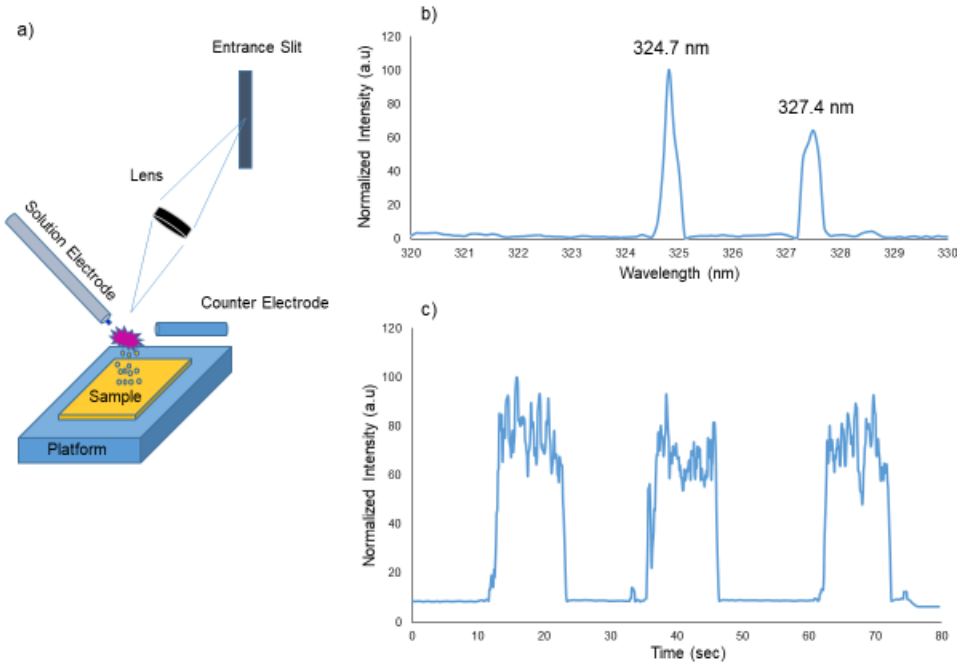

Figure 2.1 a) Diagrammatic representation of the AD-LS-APGD-OES source components. b) Representative OES spectrum in the region of the Cu I transition. c) Representative transient responses of Cu I 324.7 nm for three engagements/disengagements of Cu target with the microplasma.

2.3.2 Materials

Solid copper of stock grade was cut into approximately 8 mm square plates with 0.005 mm thickness for sampling. All electrolytic solutions were purchased from VWR (West Chester, PA) and diluted to 0.84 M concentration with deionized Milli-Q water (DI-H2O) (18.2 MΩ cm^{-1} , NANOpure Diamond Barnstead/Thermolyne Water System (Dubuque, IA)). All thin films were produced via a home-built vapor deposition system using high purity metal sources. The thin films were 100 nm thick on mica substrates (PELCO Mica, grade V5, 10 x 10 mm, Ted Pella Inc., Redding, CA) or standard microscope slides (Fisherbrand, plain microscope slides, 25 x 75 x 1 mm, Fisher Scientifc, Pittsburgh, PA).

2.3.3 Methods

Methods The parameter of interest was varied while the remaining ones were maintained as those described above. An appropriate spectral background scan, inclusive of the Cu I transition, from 320 nm to 330 nm was first taken without any copper metal in the proximity of the plasma. Next, the copper metal of stock grade was placed under the plasma and a wavelength scan taken within the appropriate boundaries five times. The value of the most intense analyte peak was normalized to 100 and the standard deviation of the peak heights calculated. Fig. 2.1b displays a representative wavelength spectrum in the analysis of bulk copper and Fig. 2.1c displays the transient signals obtained at a single wavelength with the sample engaged and disengaged three times to display the stability of the emission response. All variables and the order of testing were produced by Microsoft Excel random number generator within appropriate boundary conditions (Table 2.1) to minimize time and order bias in the analysis.

Table 2.1 Boundary conditions for the AD-LS-APGD OES parameters evaluated

Parameter	**Lower Limit**	**Upper Limit**
Current (mA)	40	60
Inter electrode gap (mm)	1	11
Sample displacement (mm)	1	4
Angle of incident (°)	40	90
Sheath gas flow rate (L min^{-1})	0.4	1.0
Counter gas flow rate (L min^{-1})	0.1	0.35
Solution flow rate (µL min^{-1})	20	115
Optical sampling position (mm)	0	2

2.4 Results and discussion

The entirety of the processes involved in producing analytically relevant optical emission responses from species desorbed from solid substrates likely depend on a number

of experimental variables. It is clear that the 300 °C microplasma is not sufficiently "hot" to affect thermal desorption of bulk metals. By the same token, no mechanism involving momentum transfer (i.e., sputtering) would be expected. Therefore, some form of surface layer dissolution is likely at play, and thus operational parameters that affect the density and types of chemical species impacting the solid are relevant. Following desorption, variables that control the transport of analyte to the active plasma environment will determine the atom density therein. Finally, the conditions within the microplasma will dictate the extent of analyte excitation and the product emission responses. Clearly, the deconvolution of these various processes is complicated and not straight forward and the parametric dependencies are interrelated. The following discussion is arranged in terms of optimization of optical sampling, and studies of those parameters affecting desorption and those involving transport and excitation/emission.

2.4.1 Spatial distribution of analyte and background optical emission

As with virtually all spectrochemical sources,[26,27] the LS-APGD is inhomogeneous in terms of the spatial location of various emitting species, be they analyte or background components.[19,28] The same is true in other solution glow discharge systems.[29] In assessing the AD-OES use of this microplasma, it is necessary to understand where desorbed analyte species must be transported for effective emission monitoring. Fig. 2.2 presents the optical emission response for Cu I emission as well as that for the OH^* band head, representative of background species. In this experiment, the spectrometer was translated such that the entrance slit sampled different portions of the focused plasma image. Based on its serving as the cathode of the diode discharge, the negative glow region is visually the most intense

portion of the plasma. This is born out in the spatial profiles for both of the monitored species. A clear segregation is observed, wherein the analyte is most efficiently excited in the near-cathode region, with the solution-related species responses being more diffuse. This response is exactly what would be expected for the case if the analyte were introduced through the cathode, but is indeed the same as seen when LA-produced particles are introduced and the solution is acting as the cathode.[17] The negative glow region is the location of highest kinetic temperature, electron density and energy, and so is the position where atomic species are most effectively excited. In referring to the insert of the figure, both the desorbed analyte and the solution species must be transported to that region of the plasma from the direction of the solution electrode. While the desorbed Cu species evolve from the target located in between the electrodes, that material must be carried in the vapor phase to the proximity of the counter electrode for effective detection. Thus, the spatial distribution here sets the most advantageous optical sampling position as well as lends insights into the processes occurring in the device.

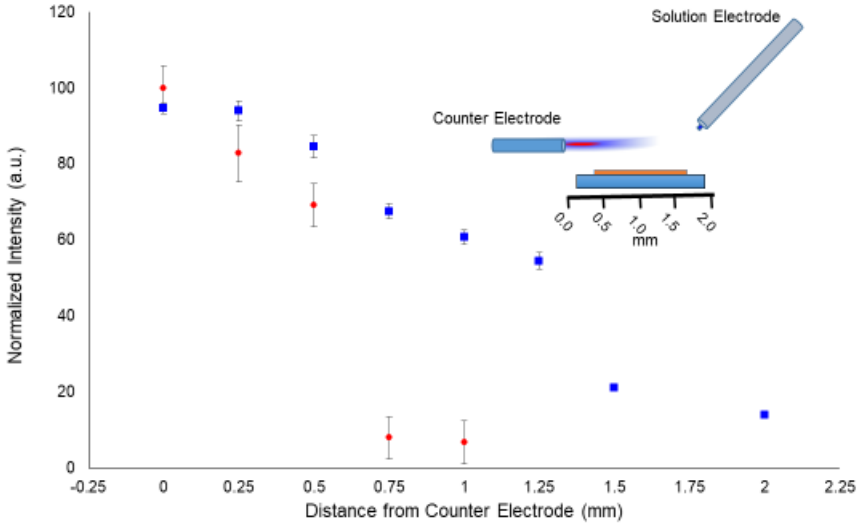

Figure 2.2 Spatial distribution of Cu I 324.7 nm (blue) and OH^* band 309.2 nm (red) emission for the sampling of a bulk copper target. Discharge current = 40 mA, electrolyte flow = 50 µL min-1, inter-electrode gap = 2 mm, sample displacement = 2 mm, angle of incidence = 70°, sheath gas flow = 0.7 L min-1, counter gas flow = 0.2 L min-1.

2.4.2 Influence of acid type, matrix form, and electrolyte solution flow on analyte emission response

As demonstrated in the earliest of the LS-APGD works, the feed solution identity was of lesser importance than the actual ionic strength of the electrolyte in terms of emission responses of solution-based samples.[18,30] In the case of the AD-OES implementation, the role of the electrolyte would likely be far more complex in terms of contributions to analyte vaporization/ desorption. Three different acids (nitric (HNO_3), hydrochloric (HCl), and formic (HCO_2H)) and two inorganic salts (Li and Na as chlorides) were tested as the electrolytic solution and their respective effect on the intensity of the Cu I emission responses measured in the sampling of a bulk copper matrix. Nitric acid is the standard electrolytic solution used in previous designs of the LS-APGD and readily dissolves copper.[31] Hydrochloric acid is a strong acid that does not readily react with copper. Formic acid is a weak acid with reducing properties and does not dissolve copper

to an appreciable extent. As Fig. 2.3a shows, the HNO3 and HCl-based electrolytes yield the highest intensities, while the response for formic acid was significantly weaker. There is 10% difference in emission responses between nitric acid and hydrochloric acid, while there is 70% decrease between nitric acid and formic acid. The Cu I emission response from nitric acid is not surprising as Cu readily dissolves in oxidizing agents such as nitric acid. However, for hydrochloric acid to display similar intensities is surprising as Cu metal is far less soluble due to its higher reduction potential. The solubility of copper is enhanced, though, in the presence of oxygen,[32] and it is not unreasonable to assume that applied energy in the form of heat, the ambient plasma environment, or indeed the electrons in the plasma could easily activate the HCl ability to volatilize the copper. While the dissolution of bulk Cu by formic acid is not favorable, the corrosion of the metal with the formation of copper formate tetrahydrate ($Cu(HCO_2)_2(H_2O)_4$) has been reported in the presence of formic acid vapor. This species could be dissolved and desorbed into the excitation environment.[33] These points taken in whole, suggest that the LS-APGD microplasma is a hot, water-based plasma environment that is far more oxidizing than the aqueous-form

acids, and that these processes normalize the native effects of the acids to yield an unexpectedly homogeneous response.

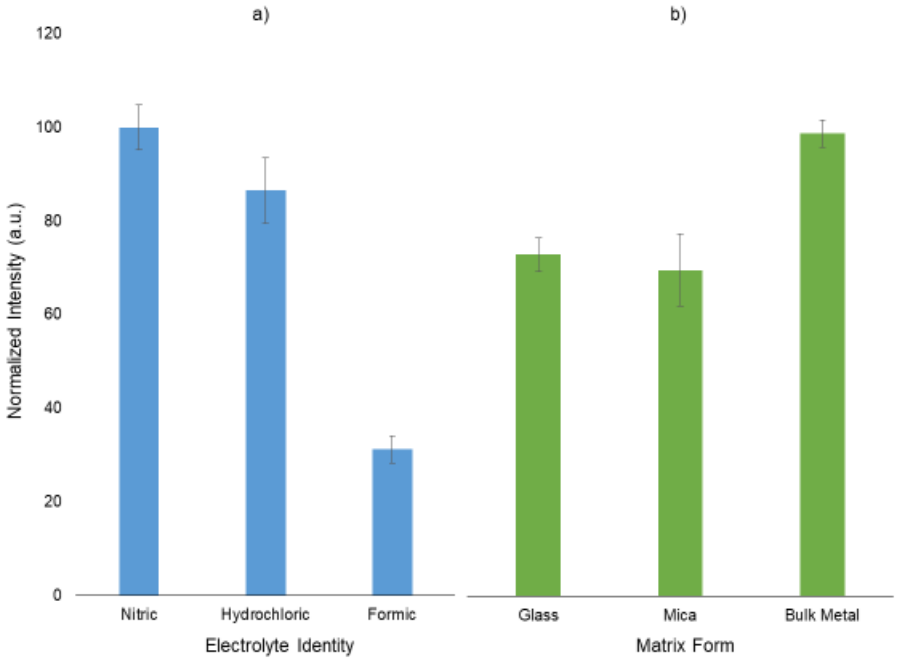

Figure 2.3 Normalized Cu I 324.7 nm emission response of bulk copper target as a function of a) acid identity and b) matrix type. Discharge current = 40 mA, electrolyte flow = 50 µL min^{-1}, inter-electrode gap = 2 mm, sample displacement = 2 mm, angle of incidence = 70°, sheath gas flow = 0.7 L min^{-1}, counter gas flow = 0.2 L min^{-1}.

While previous studies demonstrated that the type of the electrolytic species had only minimal effects on the operation of the LS-APGD and the product optical emission of solute analytes,[34] there may indeed be some influence in the AD-OES implementation of the device. As in those previous efforts, the operational parameters (e.g., current–voltage characteristics) of the microplasma here were not appreciably different for the three protic acid types, but optical emission representative of desorbed Cu target material was virtually non-existent. Even in the case of running salt concentrations across a broad range of concentrations (0.04–0.84 M), the lone effect on the target surface was the creation of a (presumed) metal salt layer. The dramatic difference in AD-OES responses between the

family of acids and the salts points clearly to the fact that the modality of analyte release is akin to a DESI process, wherein the solid is removed via a chemical process (still to be defined), versus a thermal one.

Different forms of solid copper samples were analyzed (bulk, thin film on mica, thin film on glass) to further gain insight on the operation mechanism of the plasma. As seen in Fig. 3b, the analyte evolving from the bulk copper matrix results in the most intense emission, but overall there is very little difference in intensity between the matrix types. There is 20% difference in emission response among the different matrices, with the Cu I response for the mica-deposited layer having the highest deviation amongst the matrix types. This is not surprising as the density of atoms in the bulk copper metal should be far greater than those of the vapor-deposited thin films of mica and glass substrates.[35] To be clear, the emission measurements were taken while still within the layer, and not as the layer was completely depleted. Inhomogeneous deposition is likely the source of higher variability of responses for the glass and mica as compared to that of bulk metal. In general, though, the type of matrix has a minimal effect on the copper emission. It can be assumed that thermal desorption plays a smaller part or none at all, as glass has a much lower heat capacity than bulk solid, thus one would expect glass to produce the most intense in the case of thermal deposition.

In the normal OES operation of the LS-APGD, the electrolyte solution flow rate controls the delivery rate of injected analyte as well as the solvent loading of the microplasma. As such, the analyte emission transients sharpen with increases in flow rate from 0.1 to 0.3 mL min^{-1}, but degrade in integrated intensity as delivery rate is increased.[36]

At typical operation currents of 40 mA, the plasma under these conditions can still operate in a total consumption mode of the electrolyte solution, but solution □ow rates of >0.5 mL min $^{-1}$ can result in drippage of the bulk solution from the inner capillary tip. Operation at higher currents raises the operational flow rates before onset of this effect. The effect of the electrolyte solution (5% HNO_3) flow rate on the Cu I emission response is presented in Fig. 2.4 for discharge currents of 40, 50, and 60 mA. For each of the discharge currents, it is generally observed that as the solution flow rate increases, so to does the analyte response. However, in each group of responses, a maximum response level is seen, beyond which increases in electrolyte flow do not yield greater responses. In fact, as seen most pronounced at the lowest current, the yield decreases. In the extreme, electrolyte collects at the end of the silica capillary and drips onto the sample surface. As in the standard OES case, the plasma energetics are insufficient to vaporize the entire solvent load. Previous studies by Manard *et al.*[37] revealed a minor increase in gas-rotational (T_{rot}) and excitation temperatures (T_{exc}) with increases in discharge current at a fixed solution delivery rate. This was manifest in a positive correlation between discharge current and emission intensity as described by Konegger-Kappel *et al.*, [34] as solvent is more effectively vaporized and atoms subsequently excited in the discharge volume. However, in the AD configuration of the LS-APGD the role of discharge current at a fixed electrolyte delivery rate is far less significant. There is no significant difference in intensities for flow rate at 70–80 mL min^{-1} between 50 mA and 60 mA, suggesting that the solution plays a more significant role in the vaporization step in the ambient desorption than other forms of LS-APGD. It is interesting that, the relative deviation amongst the emission responses greatly

decreases at higher solution flow rates at a given current, indicating a more reproducible desorption/transport process. Thus, it appears that optimum performance is seen at the highest flow rate allowed for a given discharge current, prior to the onset of incomplete solution vaporization at the capillary tip. Thus, it would be of interest to increase the discharge current to facilitate higher solution flow rates, but this is counterbalanced by potential melting of the fused silica capillary and fouling of the counter electrode.

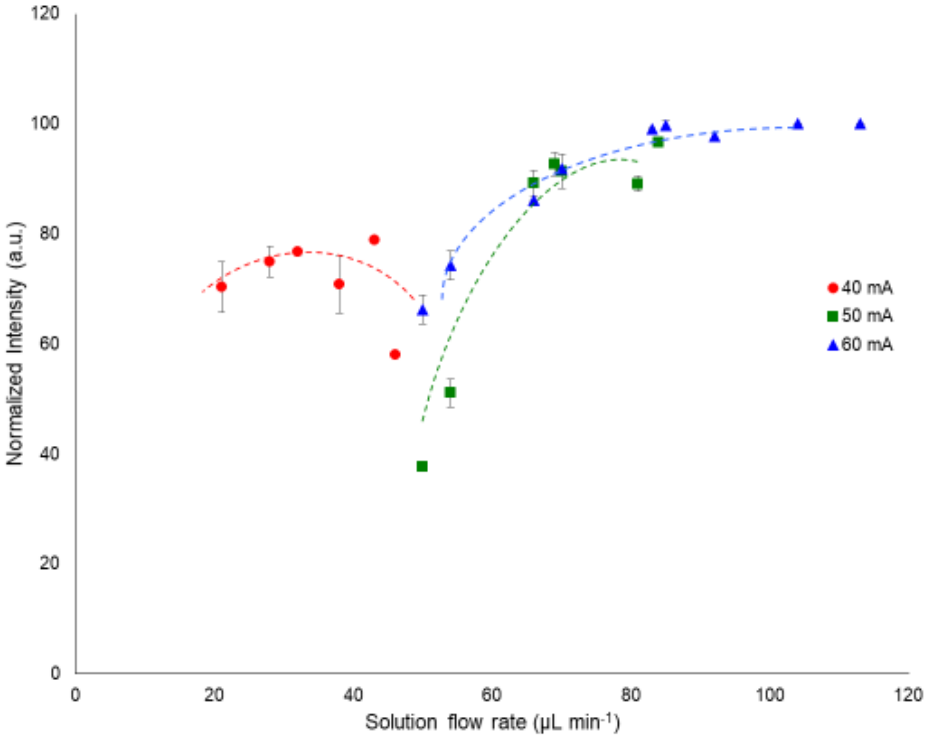

Figure 2.4 Normalized Cu I 324.7 nm emission response of bulk copper target as a function of solution flow rates and discharge current. Electrolyte flow = 50 µL min^{-1}, inter-electrode gap = 2 mm, sample displacement = 2 mm, angle of incidence = 70°, sheath gas flow = 0.7 L min^{-1}, counter gas flow = 0.2 L min^{-1}. Trend lines added to guide the eye, not representative of mathematical fit.

2.4.3 Influence of electrode positioning on analyte emission response

As with other forms of glow discharge, the most luminous region of the LS-APGD microplasma is the negative glow region adjacent to the cathode, in this case, the counter

electrode. Thus, desorbed analyte must be transported towards the cathode for subsequent excitation. Under the assumption that some form of acid initiated dissolution of the solid takes place, analyte may be thermally vaporized from the solution phase or may be introduced in a "splashing" induced by the water vapors impinging on the surface or through sheer originating from the high velocity gas flows from the counter (20 m s^{-1}) or solution (100 m s^{-1}) electrodes. These modes of release have been implicated and studied in detail for DESI.[8] Variations in the positioning between the solution electrode tip and the sample surface would be expected to affect the density of the hot acidic electrolyte arriving at the surface. In addition, changes in the distance between the sample surface and the active plasma region would also affect the efficiency of desorbed species transport to that region. Thus, the distance between the solution electrode and the solid sample would be expected to affect both the vaporization and transport phenomena. As depicted in Fig. 2.5a, as the distance between the sample and the solution electrode tip is increased, the intensity of the emission is significantly decreased, with the measurement variability increasing. At this point, the trend cannot be unambiguously attributed to effects related to either the vaporization or transport processes. Future studies using atomic absorption measurements of the evolving sample species are expected to bring further insights into these processes. While it would seem that capillary-to-sample distances of less than 1 mm might yield greater responses, the sample begins to draw discharge current when it is placed at shorter distances, causing the plasma to extinguish.

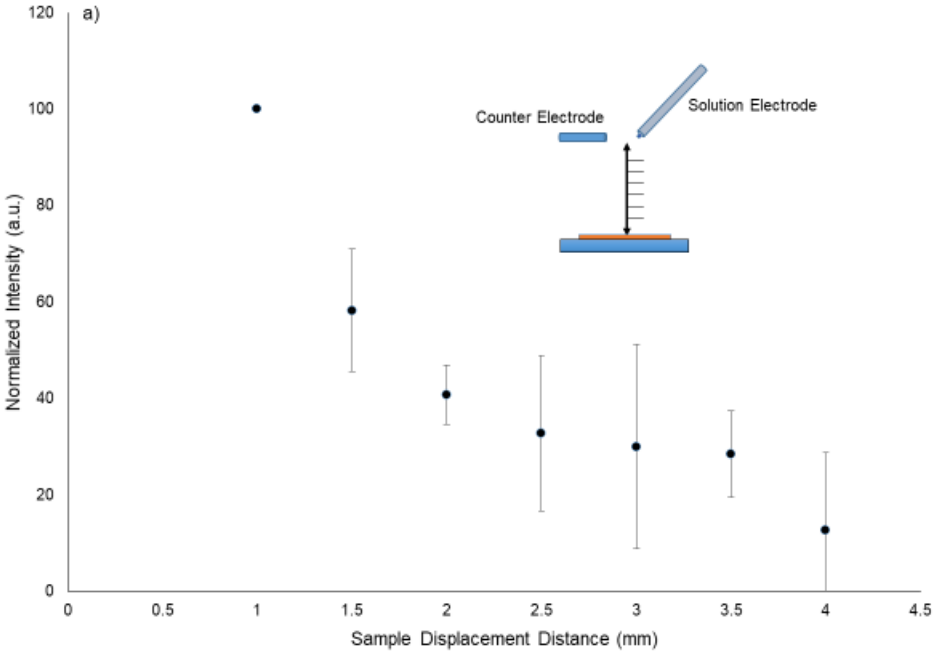
a)
Counter Electrode
Solution Electrode
Normalized Intensity (a.u.)
Sample Displacement Distance (mm)
0
20
40
60
80
100
120
0
0.5
1
1.5
2
2.5
3
3.5
4
4.5

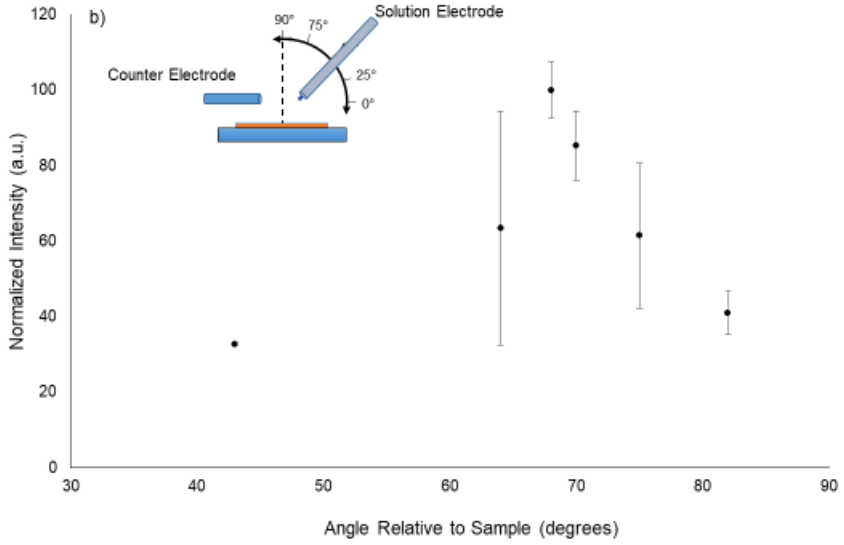
b)
Solution Electrode
90°
75°
25°
0°
Counter Electrode
Normalized Intensity (a.u.)
Angle Relative to Sample (degrees)
0
20
40
60
80
100
120
30
40
50
60
70
80
90

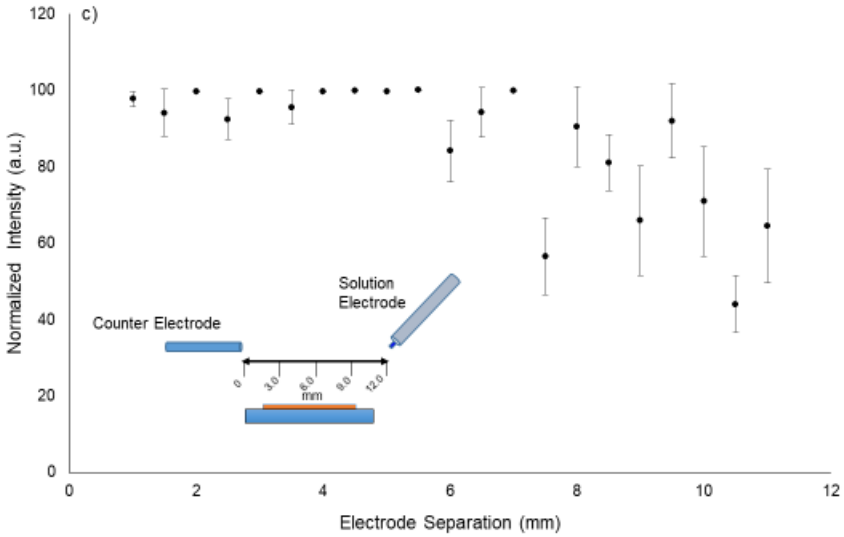

Figure 2.5 Normalized Cu I 324.7 nm emission response of bulk copper target as a function of a) sample displacement beneath the solution electrode capillary, b) angle of incidence of solution electrode, and c) inter-electrode separation. Discharge current = 40 mA, electrolyte flow = 50 µL min^{-1}, inter-electrode gap = 2 mm, sample displacement = 2 mm, angle of incidence = 70°, sheath gas flow = 0.7 L min^{-1}, counter gas flow = 0.2 L min^{-1}.

While the precise mechanism for analyte desorption remains in question, it is clear that material leaving the target surface must successfully reach the microplasma excitation region via some form of convective transport rather than isotropic diffusion into the ambient atmosphere. In the process of the eluate of the solution capillary being a hot vapor of acid, driven in part by the sheath gas flow, there would obviously be an angular dependence wherein the angle of incidence of the vapor flow most readily carries evolving species towards the excitation region. Here again, direct analogies exist with ADI-MS implementations.[8] As depicted in Fig. 2.5b, the angular dependence of the Cu I response is pronounced. Beginning with the case of the acid vapor impinging normal to the sample surface, a relatively low emission yield would be expected as the bulk □ow would literally

impede transport away from the surface, and certainly not in a direction towards the counter electrode. Decreasing the angle of incidence leads to a pronounced maximum in the analytical yield at an angle of 68° falling off as the angle is further decreased. In the most geometrically simplistic case, equivalent angles of incidence and reflectance would produce the maximum response if the process measured a direct reflection off of a surface. In this case, though, a solvent layer is likely formed and the evolving vapor must be swept towards the excitation region. Given the mass of He atoms versus vapor drops, a hypothesis emerges wherein the dense vapor exiting the solution capillary carries evolving surface species to the excitation region close to the counter electrode.

Previous LS-APGD-OES applications in the analysis of solutions and LA-produced particles yielded different results in terms of the effects that the interelectrode separations had on the respective analyte responses. For solution sample introduction, very short (less than 0.5 mm) gaps yield the greatest sensitivity, with increased separation dramatically decreasing the yields.[18] In the case of LA particle introduction through the hollow counter electrode,[38] slightly larger gaps improved performance, with the separation dependence being far less dramatic. It was projected that the longer distances in the LA case allowed for longer residence times for particle vaporization prior to entry into excitation region. As shown in the responses of Fig. 2.5c, a very different situation exists for the AD-OES mode of LSAPGD operation. As the interelectrode gap is increased from 0.5–6 mm, there is virtually no change in the desorbed Cu atom responses, which is counterintuitive on first consideration. To be clear, the position of the plasma focused onto the spectrometer entrance (close to the counter electrode) remained constant while the electrode separation

was varied. The most stable configurations in terms of emission response stability appears to be between 4 and 6 mm electrode gap. These data suggest that the transport of volatilized analyte to the excitation region is very efficient, even over distances of multiple millimeters. Beyond 6 mm in gap, the observed intensities drop and there is a high amount of deviation amongst the emission responses. It is interesting to note that there is a periodicity in the average responses at the extended distances, which implies that there may be some turbulence/eddies present in the flowing, dense molecular (water) vapor. Finally, one might expect that large inter-electrode distances would result in a weaker plasma, or even its extinguishing. In fact, the maintenance voltage increases linearly with the separation distance, which results in a constant power density. In this way, it would be anticipated that the excitation efficiency in the near-cathode region should be fairly consistent, with the observed analyte emission reflecting the flux of analyte atoms to that region.

2.4.4 Influence of sheath and counter electrode gas flows on analyte emission response

The sheath gas flow between the fused silica (solution) and metal capillaries was implemented as a means of allowing high (>40 mA) LS-APGD operation currents with improved stability and minimizing the possibility of melting the silica capillaries.[19,28] The sheath gas acts to cool the silica electrode by carrying away the heat such that the analyte solution does not volatilize within the capillary. By the same token, that heated gas serves to add a thermal component to the solution nebulization. The use of a gas flow emanating from the counter electrode was introduced to transport LA-produced particles to the plasma.[16,17] Since that time, it has been found that the counter flow serves to constrict the

plasma, increase residence times, increase analyte signal-to background ratio, and producing a more stable plasma. In the case of the present AD-OES implementation, it could be expected that the sheath gas flow would help transport desorbed material towards the excitation region near the counter electrode, as suggested by the results presented in the previous sections. The counter gas would be expected to constrict the plasma excitation region and increase residence times

As shown in Fig. 2.6, the respective roles of the sheath and counter flow gases are not as impactful as might be expected. As illustrated in Fig. 2.6a, increases in sheath gas flow rate only lead to minor increase in emission intensity, 10%. This is similar to previous work done with both solution and laser ablated (LA) analyte. This suggests that, unlike previous works,[34,38] the major role of the solution gas may be to cool the solution electrode as the plasma stability is appreciably improved while there appears to be only a minor effect on either desorption, transport, or emission processes. Any positive effects of the counter gas flow rate are also minimal as seen in Fig. 2.6b. Increased flow rate from 0.1 to 0.18 L min^{-1} produces some improvement in emission response, but an appreciable improvement in stability. Further increases in that flow act to suppress the analyte responses, as this likely serves to impede analyte from reaching the excitation region near the cathode. The overall picture appears to go along with the processes where the "bulk" flow of the aqueous vapor evolving from the solution capillary serves to coat the target surface with acidic species, releasing analyte, and carrying those species towards the active microplasma environment.

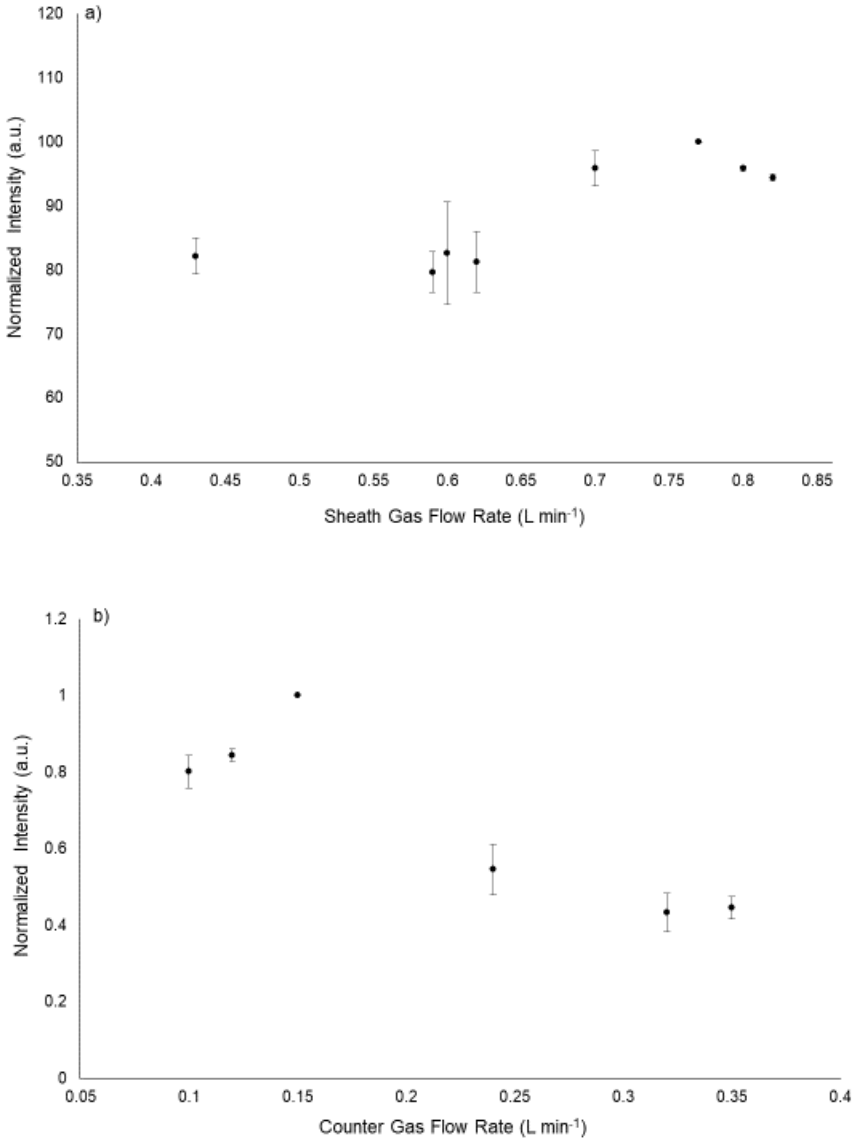

Figure 2.6 Normalized Cu I 324.7 nm emission response of bulk copper target as a function of a) sheath and b) counter electrode gas flow rates. Discharge current = 40 mA, electrolyte flow = 50 µL min^{-1}, inter-electrode gap = 2 mm, sample displacement = 2 mm, angle of incidence = 70°, sheath gas flow = 0.7 L min^{-1}, counter gas flow = 0.2 L min^{-1}.

2.4.5 Realized improvement in analytical performance

The products of a detailed parametric evaluation of a spectrochemical device are two-fold: improved understanding and improved performance. The studies above yield a global understanding into the important parameters and processes affecting the analyte emission in the AD-OES application of the LS-APGD. As in the case of ADI-MS, the plethora of parameters, analytes, and sample matrices pose great challenges in terms of quantitative elemental analysis. That said, parametric evaluations that provide greater analyte sensitivity (response per unit concentration) and better precision are surely steps in the correct direction.

In order to assess the level of improvement (if any) following the parametric evaluation, replicate (n = 5) 100 nm copper films on mica substrates were subjected to analysis using the initial plasma/sampling conditions derived from the inaugural works[25] and those which were realized in the present study. Fig. 2.7 presents representative optical transient signals as the samples were placed in proximity of the microplasma and evolution of the Cu layer to expose the mica substrate. The respective analysis conditions are presented in Table 2.2. In the observed responses, the intensity of the optical emission represents the cumulative desorption/transport/excitation processes, while the time scale of the exhaustion of the layer is a direct reflection of the vaporization rates. Clearly, the OES response is far greater in case of the optimized conditions. But, perhaps surprisingly, the time required to go through the deposited layer is very similar. This leads to the conclusion that the desorption rates under the two sets of conditions are very comparable, while the transport/ excitation processes are far more efficient for the optimized case. More

specifically, the new conditions yielded an average integrated response of 3820 arbitrary units with relative standard deviation of 15%, while the initial conditions yielded an integrate response of 594 units, with a sample-to-sample variability of 63% RSD. Thus, the detailed parametric evaluation yields approximately 6-fold improvement in sensitivity and a 4-fold improvement in reproducibility.

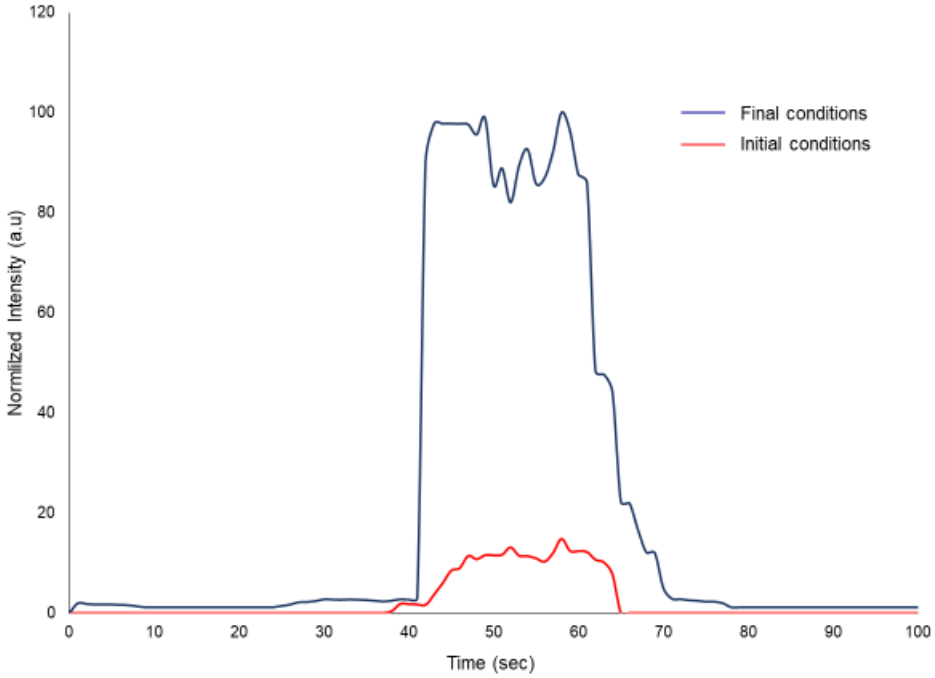

Figure 2.7 Normalized Cu I 324.7 nm emission response of bulk copper target as a function of a) sheath and b) counter electrode gas flow rates. Discharge current = 40 mA, electrolyte flow = 50 µL min^{-1}, inter-electrode gap = 2 mm, sample displacement = 2 mm, angle of incidence = 70°, sheath gas flow = 0.7 L min^{-1}, counter gas flow = 0.2 L min^{-1}.

Table 2.2 Comparison of LS-APGD operation and sampling parameters prior to, and following their optimization

Parameter	**Initial**	**Final**
Current (mA)	45	60
Inter electrode gap (mm)	2	4
Sample displacement (mm)	2	1
Angle of incident (°)	70	70
Sheath gas flow (L min^{-1})	0.7	0.7
Counter gas flow (L min^{-1})	0.2	0.2
Solution flow (µL min^{-1})	50	100
Optical sampling position (mm)	0	0

2.5 Conclusion

The LS-APGD has as its central driving force the ability to address a number of analytical challenges on a small, low cost, low power platform suitable for both in-laboratory and in-field environments. The realization of an ambient desorption optical emission spectroscopy (AD-OES) operation modality opens many new avenues of application in terms of elemental analysis of bulk solids, thin films, and solution residues. Initial efforts had shown that the developed device was capable of probing and analyzing diverse metals, using the standard nitric acid electrolyte, as used commonly in the other implementations of the microplasma.[25] Perhaps surprising, the hot acidic environment was capable of volatilizing metals which themselves are not soluble in the acid at room temperature. The present study focused on the roles of the various operational parameters using bulk copper and thin films as the target. Based on the cumulative results presented here, the desorption process appears to be similar in some respects to those of the DESI where the sample is initially solvated by the sprayed acid solvent, volatilized, and carried by the vapor created by the electrolytic solution to the proximity of the counter electrode (cathode) where the analyte atoms are excited and emit. Future fundamental studies will dissect further the (1) desorption (2) transportation and (3) excitation processes occurring in the AD-OES implementation of the microplasma. Specifically, spatially-resolved atomic absorption spectrophotometry will be implemented to follow analyte desorption and transport through the microplasma. As seen in the previous works by this group, and cited herein, there is no clear relationship between a material's solution phase acid solubility and

the volatilization in the LS-APGD microplasma. Clearly, though, better understanding and mapping of the breadth of matrix applicability is required. Further study is still required for quantitative analysis and the development of practical figures of merit. For the purpose of quantitative analysis, the addition of an internal standard in the primary electrolyte solution is possible. Radio frequency (rf) powering of the microplasma could be potentially advantageous as a means of achieving higher electron densities and energies, and more stable operation.[39] Ultimately, AD-OES should complement well the analysis of solution-based samples and particulates generated by laser ablation of solid samples. The potential to be coupled with MS for elemental and molecular species analysis[23,40] supports the overall development of the LS-APGD as a versatile spectrochemical source for a diverse range of applications.

2.6 Acknowledgements

This work was supported by the Defense Threat Reduction Agency, Basic Research Award #HDTRA1-14-1-0010, to Clemson University.

2.7 References

1. X. D. Hou and B. T. Jones, *Microchem. J*., 2000, **66**, 115–145.
2. Karanassios, *Spectrochim. Acta, Part B*, 2004, **59**, 909–928.
3. R. Costa, *Crit. Rev. Anal. Chem.*, 2014, **44**, 299–310.
4. R. B. Cody, J. A. Laramee and H. D. Durst, *Anal. Chem.*, 2005, 77, 2297–2302.
5. J. T. Shelley and G. M. Hiefije, *J. Anal. At. Spectrom.*, 2011, **26**, 2153–2159.
6. G. A. Harris, A. S. Galhena and F. M. Fernandez, *Anal. Chem.*, 2011, **83**, 4508–4538.
7. R. M. Alberici, R. C. Simas, G. B. Sanvido, W. Romao, P. M. Lalli, M. Benassi, I. B. S. Cunha and M. N. Eberlin, *Anal. Bioanal. Chem.*, 2010, **398**, 265–294.
8. Z. Takats, J. M. Wiseman and R. G. Cooks, *J. Mass Spectrom.*, 2005, **40**, 1261–1275.
9. J. T. Shelley, J. S. Wiley, G. C.-Y. Chan, G. D. Schilling, S. J. Ray and G. M. Hiefije, *J. Am. Soc. Mass Spectrom.*, 2009, **20**, 837–844.
10. R. Russo, X. Mao, H. Liu, J. Gonzalez and S. Mao, *Talanta*, 2002, **57**, 425–451.
11. R. Russo, X. L. Mao, J. J. Gonzalez, V. Zorba and J. Yoo, *Anal. Chem.*, 2013, **85**, 6162–6177.
12. J. Rakovsky, P. Cermak, O. Musset and P. Veis, *Spectrochim. Acta B*, 2014, **101**, 269–287.
13. M. R. Webb and G. M. Hiefije, *Anal. Chem.*, 2009, **81**, 862– 867.
14. P. Jamroz, K. Greda and P. Pohl, *TrAC, Trends Anal. Chem.*, 2012, **41**, 105–121.
15. R. K. Marcus, B. T. Manard and C. D. Quarles, *J. Anal. At. Spectrom.*, 2017, **32**, 704-716
16. A. J. Carado, C. D. Quarles Jr, A. M. Duffin, C. J. Barinaga, R. E. Russo, R. K. Marcus and D. W. Koppenaal, *J. Anal. At. Spectrom.*, 2012, **27**, 385–389.
17. C. D. Quarles, J. Gonzalez, I. Choi, J. Ruiz, X. Mao, R. K. Marcus and R. E. Russo, *Spectrochim. Acta, Part B*, 2012, **76**, 190–196.
18. R. K. Marcus and W. C. Davis, *Anal. Chem.*, 2001, **73**, 2903– 2910.
19. W. C. Davis and R. K. Marcus, *Spectrochim. Acta B*, 2002, **57**, 1473–1486.
20. R. K. Marcus, C. D. Quarles Jr, C. J. Barinaga, A. J. Carado and D. W. Koppenaal, *Anal. Chem.*, 2011, **83**, 2425–2429.
21. E. D. Hoegg, G. L. Hart, G. J. Hager, D. W. Koppenaal, C. J. Barinaga and R. K. Marcus, *J. Am. Soc. Mass Spectrom.*, 2016, **27**, 1393–1403.
22. L. X. Zhang, B. T. Manard, B. A. Powell and R. K. Marcus, *Anal. Chem.*, 2015, **87**, 7218–7225.
23. L. X. Zhang and R. K. Marcus, *J. Anal. At. Spectrom.*, 2016, **31**, 145–151.
24. R. K. Marcus, C. Q. Burdette, B. T. Manard and L. X. Zhang, *Anal. Bioanal. Chem.*, 2013, **405**, 8171–8184.
25. R. K. Marcus, H. W. Paing and L. X. Zhang, *Anal. Chem.*, 2016, **88**, 5579–5584.
26. C. T. J. Alkemade, T. Hollander, W. Snelleman and P. J. T. Zeegers, Metal Vapours in Flames, Pergamon Press, Oxford. 1982.
27. P. W. J. M. Boumans, *Theory of Spectrochemical Excitation*, Hilger & Watts, Bristol. 1966.

28. W. C. Davis and R. K. Marcus, *J. Anal. At. Spectrom.*, 2001, **16**, 931–937.
29. A. J. Schwartz, S. J. Ray, G. C. Y. Chan and G. M. Hiefije, *Spectrochim. Acta, Part B*, 2016, **125**, 168–176.
30. J. L. Venzie and R. K. Marcus, *Spectrochim. Acta, Part B*, 2006, **61**, 715–721.
31. A. M. Szaplonczy, *Anal. Chem.*, 1983, **55**, 2202–2204.
32. J. L. Stickney, C. B. Ehlers and B. W. Gregory, *Langmuir*, 1988, **4**, 1368–1373.
33. A. Lopez-Delgado, E. Cano, J. M. Bastidas and F. A. Lopez, *J. Mater. Sci.*, 2001, **36**, 5203–5211.
34. S. Konegger-Kappel, B. T. Manard, L. X. Zhang, T. Konegger and R. K. Marcus, *J. Anal. At. Spectrom.*, 2015, **30**, 285–295.
35. W. Wainfan, N. J. Scott and L. G. Parratt, *J. Appl. Phys.*, 1959, **30**, 1604–1609.
36. C. D. Quarles, B. T. Manard, C. Q. Burdette and R. K. Marcus, *Microchem. J.*, 2012, **105**, 48–55.
37. B. T. Manard, J. J. Gonzalez, A. Sarkar, M. R. Dong, J. Chirinos, X. L. Mao, R. E. Russo and R. K. Marcus, *Spectrochim. Acta B*, 2014, **94–95**, 39–47.
38. B. T. Manard, S. Konegger-Kappel, J. Gonzalez, J. Chirinos, X. Mao, R. K. Marcus and R. E. Russo, *Appl. Spectrosc*., 2015, **69**, 58–66.
39. D. C. Duckworth and R. K. Marcus, *Anal*. *Chem.*, 1989, **61**, 1879–1886.
40. L. X. Zhang, B. T. Manard, S. K. Kappel and R. K. Marcus, *Anal. Bioanal. Chem.*, 2014, **46**, 7497–7509.

CHAPTER III

INVESTIGATION OF HYDROPHOBIC SUBSTRATES FOR SOLUTION RESIDUE ANALYSIS UTILIZING AN AMBIENT DESORPTION LIQUID SAMPLING-ATMOSPHERIC PRESSURE GLOW DISCHARGE MICROPLASMA

3.1 Abstract

A practical method for preparation of solution residue samples for analysis utilizing the ambient desorption liquid sampling-atmospheric pressure glow discharge optical emission spectroscopy (AD-LS-APGD-OES) microplasma is described. Initial efforts involving placement of solution aliquots in wells drilled into copper substrates, proved unsuccessful. A design-of-experiment (DOE) approach was carried out to determine influential factors during sample deposition including solution volume, solute concentration, number of droplets deposited, and the solution matrix. These various aspects are manifested in the mass of analyte deposited as well as the size/shape of the product residue. Statistical analysis demonstrated that only those initial attributes were significant factors towards the emission response of the analyte. Various approaches were investigated to better control the location /uniformity of the deposited sample. Three alternative substrates, a glass slide, a poly(tetrafluoro)ethylene (PTFE) sheet, and a polydimethylsiloxane (PDMS)-coated glass slide, were evaluated towards the microplasma analytical performance. Co-deposition with simple organic dyes provided an accurate means of determining the location of the analyte with only minor influence on emission responses. The PDMS-coated glass provided the best performance by virtue of it providing a uniform spatial distribution of the residue material. This uniformity yielded an improved limit of detection by approximately 22 x for 20 µL and 4 x for 2 µL over the other two

substrates. The choice of substrate is not only restricted to the LS-APGD but can also be applied to other AD methods such as DESI, DART, or LIBS. Further developments will be directed towards a field-deployable ambient desorption

OES source for quantitative analysis of microvolume solution residues of nuclear forensics importance.

3.2 Introduction

Interest in the development of miniaturized sources for both elemental and molecular analysis has increased in terms improved sample utilization/introduction and transportable/point-of-care instrumentation systems over the past few decades.[1-3] Compact and portable instruments (in the size range of a suitcase or bookbag) would be ideal for analysis at remote sites or for online probing of process-related samples. The utilization of such approaches is especially noted in cases where perturbation of the sample can occur with transport, or when transport is dangerous/time consuming. The development of ambient desorption ionization (ADI) sources in conjunction with miniaturized mass spectrometer platforms provides an excellent example of analytical system designs directed towards diverse sampling capabilities and transportable instrumentation.[4] The primary objective of ADI sources is the ability to analyze materials in their native form, without modification of the sample.[5, 6] When paired, ADI sources and miniaturized MS instruments offer tremendous advantages for applications towards on-site analysis for remote or time sensitive samples.[7] A wide range of ADI sources has been described in literature,[6, 8, 9] One of the more developed of these techniques is desorption electrospray ionization (DESI).[10] This variant of the ESI-MS approach has been focused on the ionization of molecular

species desorbed from a surface. Application of this device has touched fields ranging across pharmaceuticals, agriculture, and forensics.[10-12] The other commonly employed, commercially available, ADI source is the DART (direct analysis in real time) which is based on the use of a glow discharge (GD) operating at atmospheric pressure to vaporize samples with subsequent ionization affected by helium metastable species created in the plasma and formation of proton donors in the gas phase.[5] To be clear, implementation of both of those devices has been directed principally at qualitative identification of organic/molecular constituents of the sample as sampling imprecision and low accuracy have been consistent shortfalls across all ADI-MS methods.[13] The samples most needing of AD methods are found across fields such as forensics,[14] medicine,[15] and archaeology.[16] These same applications might also benefit from field portable instruments capable of on-site elemental analysis. In some instances, in-field elemental analysis via optical emission spectroscopy (OES) could be advantageous over mass spectrometry in terms of system simplicity. To our knowledge, none of the commercial ADI-MS sources have been applied for elemental/atomic MS analysis or have been shown to be applicable for OES analysis. A development of a number of low-power, plasma-based devices applied for the OES analysis of liquid samples has been described, with the goals of potential reductions in OES system overhead or operation at remote locations.[17, 18] Generally, these sources operate based on the concept of utilizing an electrolytic solution as a sample carrier into an ambient atmosphere plasma operating in the GD regime. These devices offer advantages in terms of size and supporting utilities in comparison to the laboratory-standard inductively-coupled plasma (ICP). Many of these devices have been described in a very recent review.[19]

This laboratory has developed one such spectrochemical source, the liquid sampling-atmospheric pressure glow discharge (LSAPGD) microplasma.[20, 21] A key attribute of the LS-APGD is the variety in sample modalities that can be analyzed, including solutions, gases, and particles introduced via laser ablation.[22] The microplasma has not only been employed for OES analysis, but as an ionization source for both elemental[22-24] and molecular species MS.[25, 26]; a differentiating feature amongst the various liquid sampling GD mini/microplasmas. One additional unique capability of the LS-APGD versus the other electrolyte solution GDs is operation is a direct AD mode of sampling, such that molecular and atomic analysis can be affected by mass spectrometry [27] as well as elemental analysis by optical emission spectroscopy.[28, 29] However further development in methodology, particularly in regards to sample preparation, is required to achieve high quality quantitative analysis utilizing the LS-APGD-OES. Here we direct our efforts to the case of sampling of microvolume solution residues. Various critical issues arise when preparing solution residue samples, such as the need to form uniform deposits and the ability to visually identify the product residues as these are both keys to reproducibly sampling the material. Referring back to DESI, various methods have been utilized in sampling of residues such as depositing sample solutions in formats such as 96 well plates,[30] on poly(tetrafluoro)ethylene (PTFE) films/sheets,[31] and on PTFE-printed glass.[32] Those studies point to the advantages of substrates that allow greater control over the sample deposition process, allowing for more repeatable measurements. However, they lack the capability to visualize the residue and the depletion of the residue after analysis. The objective of the present study was to establish a practical method to deposit microvolume

solutions, and the derived solution residues, for AD-LS-APGD-OES analysis. While the capability to desorb various metals (including solution residues, bulk metals, and thin films) and molecules has been demonstrated,[27, 28] there is much to be learned to optimize the method. A recent study focused on the optimization of the operation parameters of the plasma regarding solid (bulk) materials analysis.[29] However, to improve the analysis of residues, the solution deposition step requires further refinement in terms of the droplet composition, volume, and placement/sampling reproducibility, as each effects the analytical performance of the technique. An aqueous solution composed of lead (Pb) as the test analyte is utilized due to its analytical significance across diverse fields of application. Various approaches were investigated to better control the location/uniformity of the deposited sample. Initial efforts involving placement of solution aliquots in wells drilled into copper substrates, (akin to approaches used in MALDI-MS and DESI-MS analysis) proved unsuccessful.[30, 33] Presented here are design-of-experiment (DOE) methods of evaluating the significance of the operational parameters in solution residue analysis by AD-LS-APGDOES. The experimental variables placed in the DOE matrix were the volume of the droplet, analyte concentration in the droplet, solution matrix additives (NaCl, EtOH, HNO_3), and number of times the droplet was applied to the substrate. Addition of an organic dye to the test solutions was evaluated as a means of better visualizing the analyte residue. Finally, a number of deposition substrates were screened for AD analysis, in hopes of yielding better reproducibility of the sample deposition, analytical precision, and analyte responses. While further work remains in the method development for the

quantitative analysis of residue samples, the potential utility of the LS-APGD for a field-deployable platform merits those efforts.

3.3 Materials and methods

3.2.1 Instrumentation

The design of the AD-LS-APGD-OES system has been described in detail in previous works.[28, 29] The plasma is sustained between a solution electrode (acting as the cathode) composed of a 75 µm i.d. x 125 µm o.d. fused silica capillary protruding ~1 mm from within a 500 µm i.d. x 700 µm o.d. stainless steel capillary and a second like sized counter-electrode capillary. A 0.84 M nitric acid solution is pumped through the silica capillary at 100 µL min^{-1} to provide electrolytic conductivity to sustain the plasma discharge at the solution surface. The solution is delivered via a syringe pump (NE1000, New Era Pump System, Inc., Farmington, NY) and the discharge is maintained via a Bertan (Hickville, NY) Model 915 series power supply operating in a constant current mode at 55 mA. A 10 kΩ ballast resistor is placed in series, between the supply output and the powered anode. Helium sheath gas flows between the fused silica and steel capillaries of the solution electrode at 0.7 L min^{-1} and through the capillary forming the counter electrode at 0.2 L min^{-1}. All parameters were set based upon the parametrization previously performed.29 A CVI Laser (Albuquerque, NM) Digikrom 240, 0.24 m focal length monochromator system equipped with a Hamamastsu (Bridgewater, NJ) R928 photomultiplier tube (PMT) was used to obtain optical emission spectra. CVI Spectra AD III software, acquired from Spectral Products (Putnam, CT), was used to control the functions of both the monochromator and the PMT. Emission from the source was focused onto the 50 µm-wide

entrance slit of the monochromator by a 75 mm focal length fused quartz lens. Spectral scans were acquired at a rate of 100 nm min^{-1}, with a signal integration time of 6 ms per 0.01 nm wavelength step. The spectral scans ranged from 395.8 nm to 410.8 nm to cover the Pb I transition. All single-wavelength optical transient measurements were acquired at a rate of 10 points per second. Visual images of droplets and the resulting residues were captured with the 16- megapixel camera of a Samsung Galaxy S6 phone with Android 5.0 as an operating system. The images were analyzed with respect to spot area and circuity measurements utilizing ImageJ (Bethesda, MD) software.[34]

3.2.2 Materials

Concentrated nitric acid was purchased from VWR and diluted to 0.84 M with deionized Milli-Q water (DI-H2O, 18.2 M cm-1) derived from a NANopure Diamond Barnstead/Thermolyne water system (Dubuque, IA)). A 500 µg mL-1 solution of lead was prepared by dissolving lead nitrate ('Baker Analyzed' Reagents, Center Valley, PA) (10099-74-8) in 0.84 M nitric acid solution. A 2 mg mL-1 Reactive Blue 4 dye solution was prepared by dissolving Reactive Blue 4 (Sigma-Aldrich, St. Louis, MO) (13324-20-4) in 0.84 M nitric acid solution. Dyes of other colors were prepared by adding 5 drops of various food colorings (McCormick, Sparks, MD) into 1 mL of 0.84 M nitric acid solution. PTFE sheets of 1.6 mm thickness and oxygen free copper plates of 6.35 mm thickness was purchased from McMaster-Carr (Douglasville, GA) for use as substrates. An array of wells 1 – 5 mm in diameter and depths of 1-3 mm were drilled into the copper plates (10 mm x 10 mm) in-house. Poly(dimethylsiloxane) (PDMS) substrates were prepared by coating a

glass slide with less than 50 µL of PDMS solution (SigmaAldrich, St. Louis, MO) (107-46-0) and placed to dry in an oven at 100 °C for 1 hr.

3.2.3 Methods

To test the viability of using "wells" as a method for constraining deposited microvolumes as utilized in other AD techniques,[35] 1 µL of 500 µg mL^{-1} Pb was deposited into the wells of the copper plate. The deposits were then dried in a simple laboratory oven set to 100 °C for ~ 15 mins. The well was placed directly under the plasma and transient measurements were taken at 405.8 nm, a Pb I transition. This line is chosen due to minor background interferences and high emission response. When the residue location is not bounded by a barrier, i.e. cups, it is highly desirable to visualize the exact location of the residue. To achieve this, residues were prepared using solutions of 500 µg mL^{-1} Pb doped with the various dyes and depositing 1 µL of said solution onto a PTFE substrate, followed by drying in a laboratory oven set to 100 °C for ~ 15 mins. Both the residue and droplet images were taken by a camera at set distances directly above the residue/droplet then analyzed using ImageJ software. Figure 3.1 is a photograph of a number of 2 µL droplets incorporating different dyes, with the perimeter of one of the droplets as identified by the software's "magic wand" function at 25 % tolerance. JMP pro (Cary, NC) statistical software was used to study the significance of the droplet volume, solute concentration, matrix modifiers (NaCl, ethanol), and number of droplets deposited on signal intensity and transient area. A design of experiment (DOE) protocol was executed,[36] including 25 parametric variations as presented in Table 3.1, with each measurement performed in triplicate. Standard least squares with emphasis of the effect screening was used to

determine the significance of the parameters. The analysis is presented in the form of standard Pareto plots36 to demonstrate the magnitude of each parameter and their significance relative to the overall experimental variability and emission response.

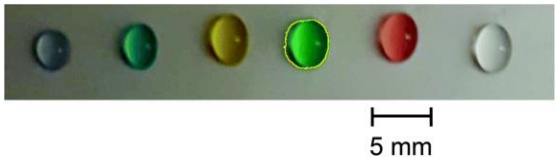

Figure 3.1 Photographic image of 1 µL of 500 mg L-1 droplets doped with various dyes. The yellow outline on the left-most dye is the perimeter of the dye determined by ImageJ software's magic wand function at 25% tolerance.

Table 3.1 Experimental parameter matrix employed in DoE method

Run	Volume (µL)	Concentration (µg mL^{-1})	Co-Deposit	Number of Deposits
1	10	100	NaCl	1
2	10	100	NHO_3	15
3	5	1	NHO_3	10
4	10	100	HNO_3	10
5	5	1000	H_2O	1
6	5	1000	Ethanol	15
7	5	100	Ethanol	10
8	10	1000	HNO_3	1
9	0.5	1000	NaCl	15
10	10	1000	NaCl	10
11	10	1	H_2O	15
12	10	1	NaCl	5
13	0.5	1	HNO_3	15
14	0.5	1000	HNO_3	1
15	5	1	HNO_3	1
16	10	1000	H_2O	10
17	0.5	100	H_2O	5
18	0.5	1000	NaCl	10
19	5	1000	HNO_3	5
20	0.5	1	Ethanol	10
21	0.5	100	Ethanol	1
22	5	100	NaCl	15
23	10	1	Ethanol	1
24	0.5	1	H_2O	15

3.4 Results and discussion

3.4.1 Preliminary evaluation of metallic well structure as an AD-OES support

As found throughout the ambient desorption literature, the ability to obtain accurate and precise quantitative analysis is the ability to control, visual, and sample the position where the sample has been deposited. It is often difficult to determine the exact location of the residue on a substrate to affect the analysis. Various preparation methods can be used to determine the location of a residue, such as marking the location of the droplet before drying or placement in a well structure. With those methods, however, various issues arise. Marking the location of the droplet does not account for the possible changes in shape and location of the residue during the drying process. Also, simply marking the location of the

droplet gives no information about the consumption of the residue as the marking will remain even as the residue is fully consumed. Other issues come into play when placing the droplets in wells. It is natural, by analogy to MALDI-MS, to investigate the use of a metal substrate having small recesses as supports for the AD-LS-APGD-OES method. In this way, sample aliquots can be applied in well-defined, spatially-confined positions to ensure application reproducibility. Likewise, such a format would be advantageous in an automated platform for sequential analyses. Multiple-well arrays consisting of various diameters and depths, prepared on Cu blanks were investigated using 1 µL aliquots of the Pb analyte solutions. Previous studies had shown that metallic Cu was indeed a good general substrate for solution sampling. Unfortunately, under no circumstances of well geometry was Pb I emission observed. The proposed mechanisms of analyte introduction into the LS-APGD microplasma environment involves vaporization and transport based on the respective sheath and counter electrode gas flows.[29] In that work, close proximity (~1 mm) of the electrodes and the support surface was a key parameter. In addition, there is a angular dependence on the placement of the solution electrode with the surface normal. As such, a lack of appreciable response from the analyte deposited in the tested well structures is not surprising. Simply, the path of the analyte towards the plasma is blocked by the sharp rise in topography of the substrate, as the analyte is not carried directly upwards but at an angle towards the plasma. To rule out possible interferences from potential copper-oxide/nitrate formation on the copper substrate, a 1 mL droplet (to ensure visualization/sampling) of 500 µg mL^{-1} Pb solution was deposited onto a flat surface of the copper plate and the transient response measured. A strong emission response was

obtained; thus, a reasonable assumption can be made that the walls of the wells of the substrate are interfering with the analysis of the analyte.

3.4.2 Screening for influential parameters

Given the sampling limitations from well structures, efforts turned towards use of flat substrates and evaluation of how deposition parameters and substrate materials could be optimized towards better analytical performance. The various solution deposition parameters in creating the analytes residues for AD-LS-APGD-OES analysis are easily projected to affect the emission response of the Pb test solute. Thus, a multivariate test was applied to screen for the influences of the various parameters (droplet volume, solute concentration, matrix modifiers, and number of droplets) on the emission response utilizing a glass substrate as had be demonstrated in the initial description of the AD-LS-APGD method.[28] To be clear, these various aspects are manifest in the mass of analyte deposited as well as the size/shape of the product residue. The initial model built with a linear combination of all parameters (Table 3.1) showed that only total mass and residue area yielded significance values of >0.5 as shown in the Perot plot depicted in Fig. 3.2a. Thus, a refined model was built by removing all values below that of 0.5 LogWorth. The cross value of total mass and residue area was then added as surface density. That statistical analysis demonstrated that the area of the residue alone has a minor influence on emission response of the analyte (Fig. 3.2b). However, surface density has a significant effect on the emission response. It is also important to note that the area of sampling for the plasma is ~ 12.5 mm^2, [28] thus, unless total consumption of the residue can be assumed, the response is more accurate for surface concentration than for absolute mass. Figure 3.3a demonstrates

the positive correlation of transient area to surface density describing the importance of measuring the residue area for analytical purposes.

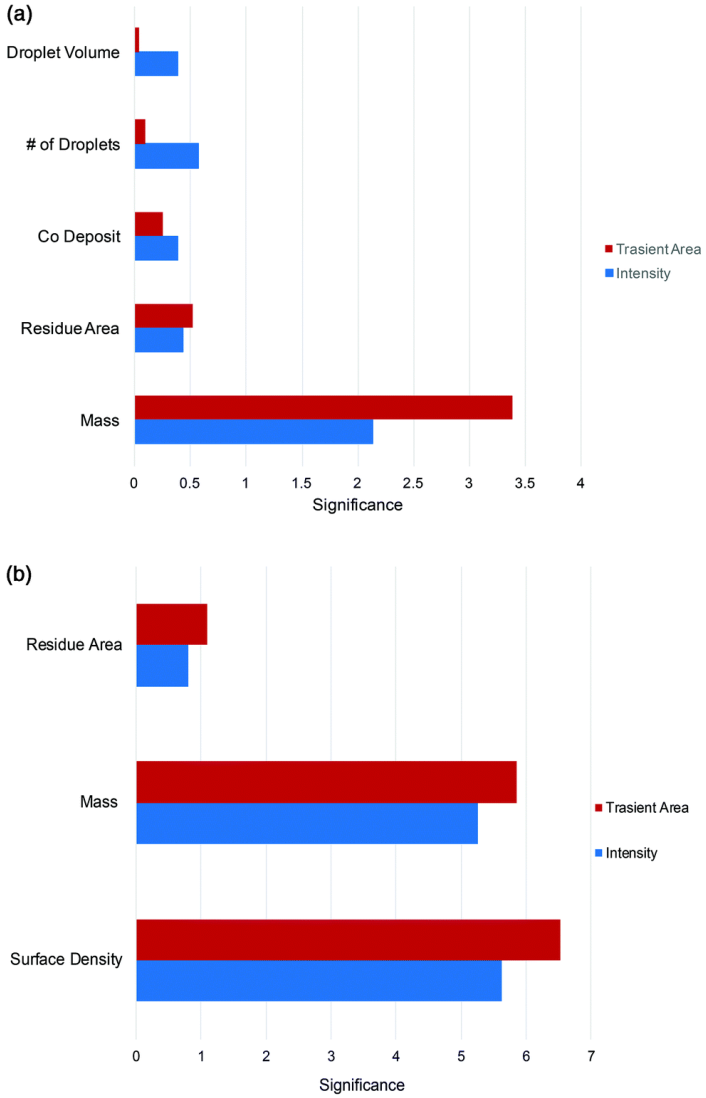

Figure 3.2 A Pareto plot demonstrating the parametric significance a) across the test parameter matrix and b) reduced to droplet area, surface concentration, and mass on transient area (red) and intensity (blue) of emission response.

It should be emphasized that the data making up the figure is extracted from the entirety of the 25- condition matrix, having variations in matrix additions, the solute concentration in each droplet, and the number of droplets leading to the residue, and therefore cannot be thought of as a calibration curve per se. It does strongly demonstrate the physical

relationship between the density of solute residue on the surface and the OES response. That said, for residue areas smaller than 12.5 mm^2 , total consumption may be assumed and thus it is more accurate to assign residue mass as the primary influence. For example, with the responses correlated to solute mass in Fig. 3.3b, the highlighted data point has over 2x the residue area of the plasma sampling size than the point immediately above it which is the same mass is a smaller area. For this reason (i.e., none total consumption) the transient area count is much smaller than one would expect. Therefore, it is important to accurately measure the residue area in hopes of obtaining high analytical quality. As an alternative, sample deposition methods which yield uniform residue sizes are necessary.

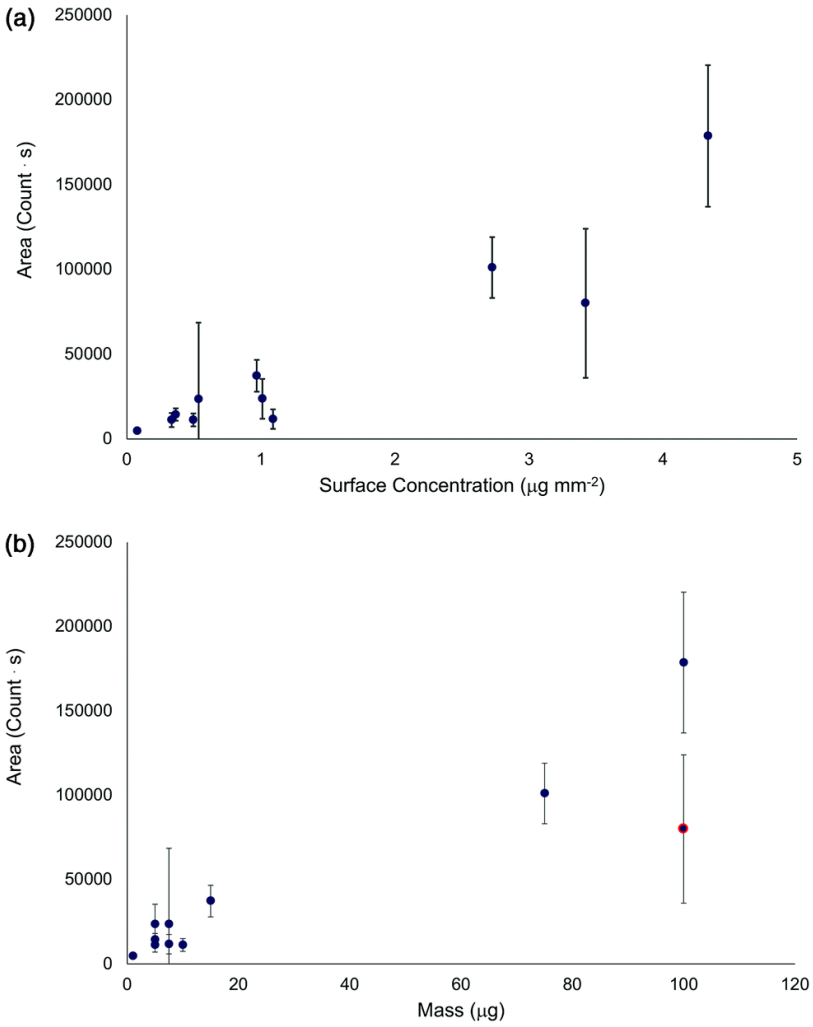

Figure 3.3 A plot demonstrating a linear correlation between a) surface concentration and b) mass and transient area with data acquired from the DOE. The highlighted data point on b) indicates a residue area of ~ 2x that of the sampling area.

3.4.3 Visualization of solution residues

Since the residue area of the sample is indeed a significant factor in residue analysis, a preparation method must either permit visualization of the sample or physical constrain the residue area. A straightforward method of visualizing the location of the analyte is to mix a standard dye with the sample solution as depicted in Fig. 3.1. It would be advantageous, in fact, to be able to visualize the initial application of the sample droplet as

well as the product residue not only for the LS-APGD but other AD sources as well. The PTFE substrate provides a suitable surface to assess the visualization process. Fig. 3.4a represents the droplet and residue area of solutions doped with various dyes as well as the resultant residues, as determined using the cell phone camera and processing software. It should be noted that while the droplet of solution with no dyes added is visible to the camera, it is not possible to determine the location of the residue with substantial certainty due to a lack of contrast with the PTFE substrate. Across the range of added dyes, two distinct groups of responses are seen. In the cases of the reactive blue dye and the green and red food colorings, the determined areas of the droplets and residues are the same, or slightly smaller for the residues. Contraction of the size as the droplet dries makes sense as the droplet condenses in size during the course of solvent evaporation. In the case of the blue and yellow food dyes, there is a significant decrease (>75%) in area once the droplet is dried into a residue. The mechanism of this phenomenon is uncertain but may be caused by the dye crashing out of solution only after large amount of evaporation (meaning they have a high solubility in H_2O) or an interaction between the dye molecules and the constituents of the solution. To test the potential interference of the dyes with the solute (Pb) emission response, residues of 1 µL aliquots doped with various dyes were sampled by the AD-LS-APGD. Figure 3.4b shows that the emission responses from the dye-doped solutions suffer a minor suppression of response from the Pb solute. Potential causes for the lesser responses may include formation of metal-dye conjugates which are not dissociated in the plasma or possible quenching properties of the dyes in the gas phase. Afterwards, the substrate was scanned under the plasma to determine if any measurable

amount of analyte remains after the dyes were no longer visible, however, no emission response can be seen.

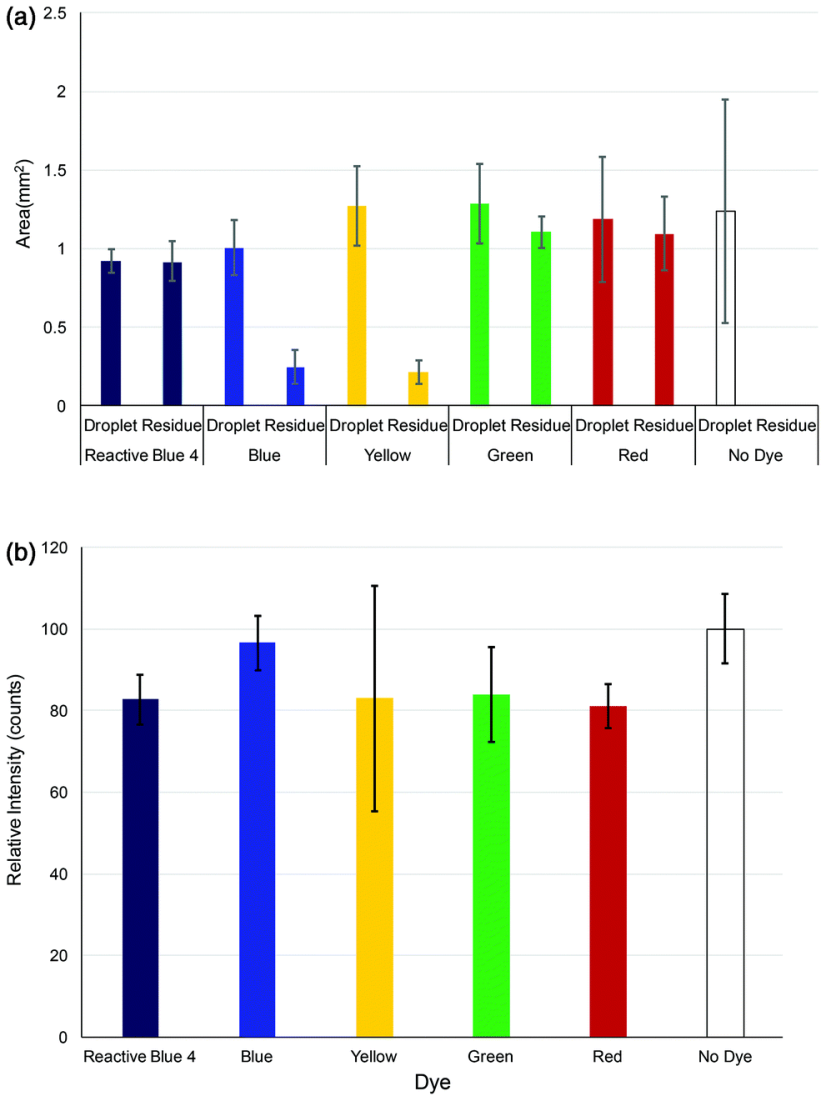

Figure 3.4 a) The area of droplet and dried residue of 1 µL of 500 mg L-1 Pb solution doped with various dyes. b) The emission response from 5 µg of Pb residue doped with various dyes.

3.4.4 Evaluation of the roles of substrate material composition

While simple borosilicate glass, as used in previous studies involving AD-LSAPGD,[27, 28] is a natural substrate choice due to simplicity, cost, and availability, it has inherent disadvantages when preparing residues for microplasma sampling. First, the

surface chemistry of borosilicate glass is appreciably different from PDMS coated glass and PTFE as are often utilized in DESI. [31, 32] As confirmed in the DOE parameter evaluation results depicted in Fig. 3.2b, spatial confinement of equivolume deposits, resulting is greater solute surface densities, is a critical parameter. The role of substrate hydrophobicity in droplet wetting and resultant residue size is graphically depicted in Fig. 3.5a for the glass, PDMS-coated glass, and PTFE substrate. Clearly, the absolute area and rate of area increase with added droplet volumes, is far greater for the glass substrate than the other two. Keeping in mind the need to restrict the dry solute area to values of <12.5 mm^{-2} to assure complete microplasma vaporization, the amount of sample solution applied is clearly limited in the glass substrate case. To prepare a residue for complete consumption, one would have to use a droplet volume of ≤5 μL when depositing onto a glass substrate, while for both PDMS coated glass and PTFE substrate, the droplet volume can be up to ~ 20 μL. In principle, this increase in droplet volumes should allow for greater flexibility in applications needing high sensitivity.

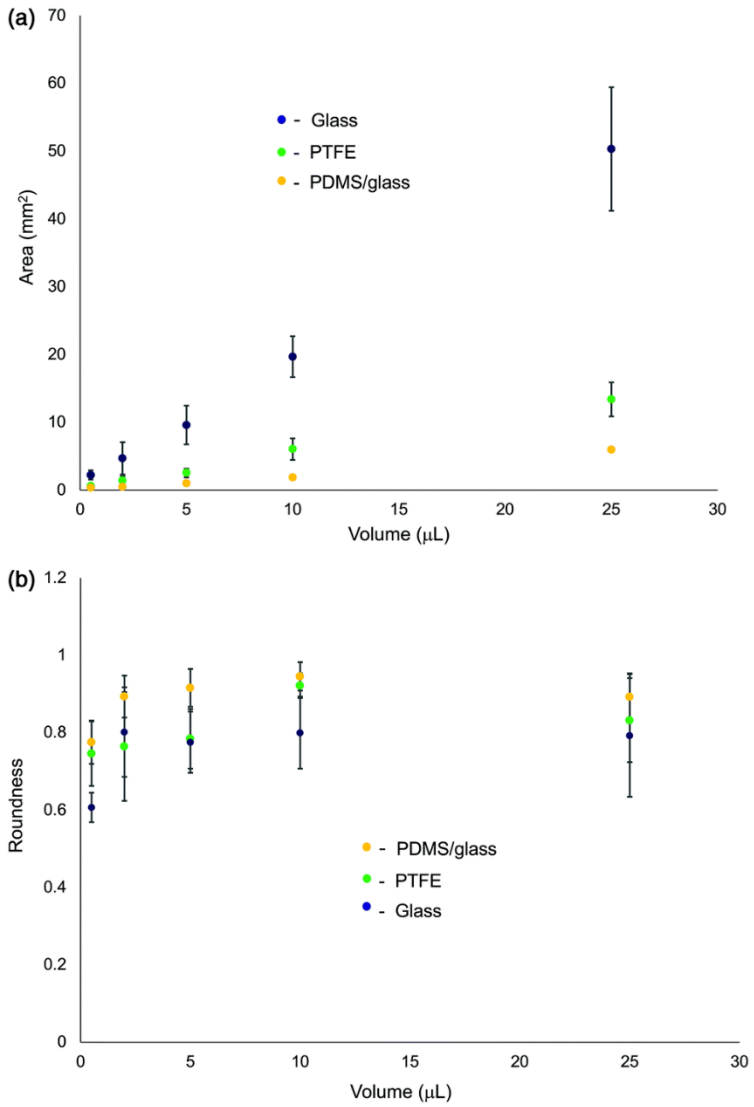

Figure 3.5 The effect of droplet volume on glass (blue), PTFE (green), and PDMS/glass (yellow) pertaining to a) residue area b) roundness.

Another difficulty in utilizing a glass substrate is the spatial uniformity of the product residue. While a sufficiently small residue will be completely desorbed regardless of uniformity, a non-uniform residue similar in size of the plasma sampling area could result in the incorrect assumption of complete sample consumption. The uniformity of the residue is determined by the ImageJ circularity measurement function typically used in

determining the shape of biological cells.[37] The operating equation is given as $S = 4\,\pi * (\frac{Area}{Perimeter})$, where a value of 1.0 indicates a perfect circle. Figure 3.5b depicts the roundness of the residues as a function of the deposited solution volume for the three substrates. In all cases, the PDMS/glass support yields the highest level of roundness, i.e., uniformity. Interestingly, at larger solution volumes the roundness degrades slightly for the two hydrophobic surfaces (PDMS and PTFE), while the quality of the glass deposit remains fairly stable, though with much higher levels of variability as seen in the error bars. Overall, based on the ability to restrict the residues to small, uniform areas, the PDMS is the most effective substrate, particularly at higher sample droplet volumes. It would therefore be expected to yield the best analytical precision of the three materials.

Of course, the quantitative responses of analytes is the primary determining factor in process optimization. Figure 3.6 shows a comparison of the integrated intensities representing a 0.5 µg of Pb residue (1 µL of the 500 µg mL^{-1} stock solution) on the various substrates. This volume was chosen under the assumption that the residues would be totally consumed in each case. As shown, there is a negligible difference between those of the PDMS and non-coated glass substrate, however, there is an ~50% decrease in the emission response off of the PTFE substrate. One possible reason for this phenomenon is the degradation of PTFE at ~300 °C, which can cause structural degradation on the surface of the substrate, which was confirmed by optical micrographs of pristine and post plasma exposure surfaces. This degradation leads to cracks in the substrate where the analyte may

infuse into the substrate. However, further investigation is required to fully deconvolute the suppression of the analyte signal.

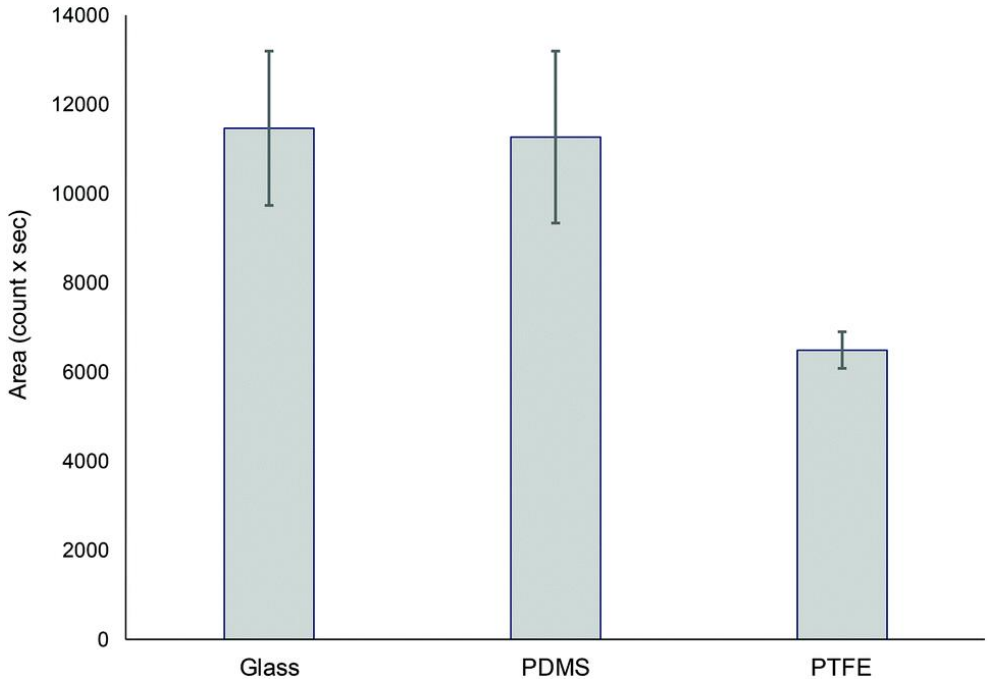

Figure 3.6 Emission response from 5 µg of Pb on different substrates.

As a final test of the potential influences of the substrate material on the quantitative performance of the AD-LS-APGD-OES analysis of solution residues, analytical response curves were created utilizing 2 and 20 µL solutions of various Pb concentrations on the borosilicate glass and PDMS-coated glass targets. The 2 µL volumes created residues of approximately 4.5 mm^2 for glass and 0.4 mm^2 for PDMS coated glass, while the 20 µL volumes created residues of approximately 40 mm^2 on the glass and 11 mm^2 on the PDMS. In the case of the glass support, the smaller volume should ensure complete sampling of the residue, while the larger volume instills a great deal of uncertainty as to the fraction of sample which may be consumed. The two volumes deposited on the PDMS surface would be expected to be effectively sampled,

with the larger volume yielding greater amounts of residue material per unit solution concentration. As shown in Fig. 3.7 (and summarized quantitatively in Table 3.2), the expected increase in sensitivity (slope) is indeed realized using the greater volume of solution on the PDMS substrate. Indeed the 10-fold greater amounts of solute per unit volume is easily realized, albeit with some forfeiture in linearity. Examination of the responses derived from the solutions deposited on plain glass support point to the nonquantitative sampling of the larger sample volume. In this case, the improvement in sensitivity is only factor-of-3 greater in moving from 2 to 20 µL. One might expect, though, that the more complete sampling of the 2 µL residue would be more reproducible. This is the case, but due to overall poor sensitivity, the lowest points of the response curve are just below the detection limit and so yield a strong perturbation on the R^2 -value.

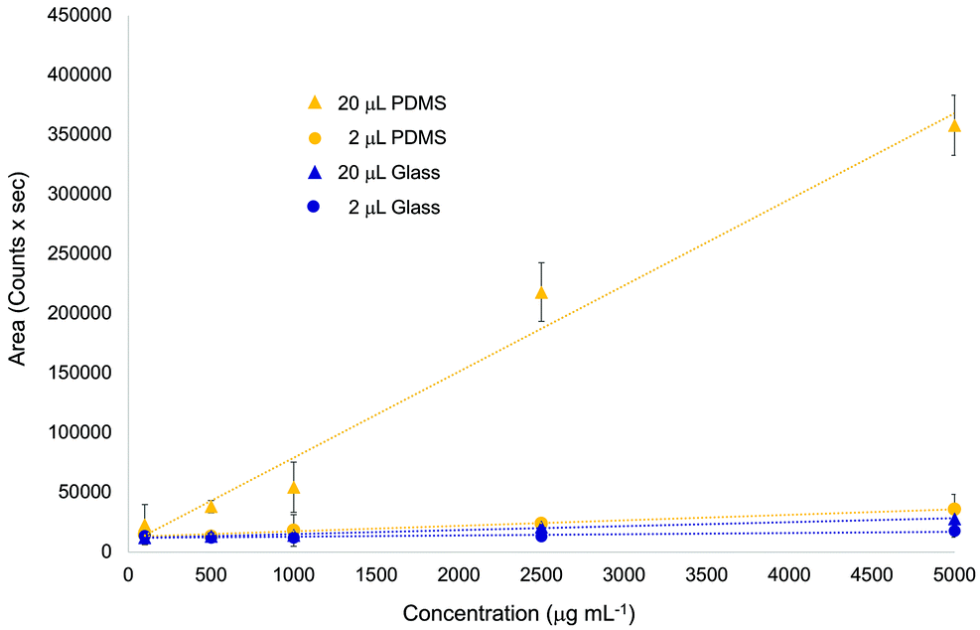

Figure 3.7 Calibration curve of 2 µL glass (blue circle), 20 µL glass (blue triange), 2 µL PDMS/glass (yellow circle), and 20 µL PDMS/glass (yellow circle)

Table 3.2 Computed limits of detection for Pb determinations based of support identity and volume of solution deposited

Support	Volume deposited (µL)	Regression analysis	LOD (µg mL^{-1})	LOD (µg, absolute)	%RSD (2500 µg mL^{-1})
Glass	2	Y = 1.01x + 11950 R^2 = 0.7575	1629	3.3	16.0
	20	Y = 3.33x + 11788 R^2 = 0.9878	528	10.6	24.4
PDMS	2	Y = 4.61x + 12840 R^2 = 0.98111	410	0.82	11.9
	20	Y = 72.2x + 6898 R^2 = 0.9794	24	0.48	11.3

Based on the response curves, the determined limits of detection (LOD = 3_{sblank}/m) are summarized in Table 3.2 in terms of the initial solution concentration as well as the absolute mass deposited on the respective surfaces. The mass-based LOD values are determined simply by adjusting for the total volume deposited. A couple of interesting aspects are realized in this tabulation. On a concentration basis, use of larger volumes results in improved LODs as greater quantities of solute are introduced into the microplasma. The level of improvement should roughly equate to the 10 greater amounts of sample, but clearly in the case of the glass substrate, this not realized, as the slope/yields only increases by ~3x. On the other hand, the increased sample volumes deposited on the PDMS yields ~15x greater intensity. As the standard deviations of the respective blanks are not appreciably different, the LODs respond accordingly. Clearly, the use of the hydrophobic surface to confine the solution droplets has achieved its goal with respect to more-quantitative sampling. Taken a step further, the process is also more reproducible as depicted in Table 3.2. In this instance, the percentage relative standard deviation for triplicate analyses of 2,500 µg mL^{-1} test solutions. As depicted, depositions on the glass

surface, particularly for the larger volume, are appreciably less reproducible than the applications on the PDMS surfaces.

3.5 Conclusion

The liquid sampling-atmospheric pressure glow discharge (LS-APGD) microplasma has demonstrated impressive versatility in terms of sample forms and potential analytes species.[22] One possible type of sample form is a solution residue, having various applications in the fields of forensics, medicine, archaeology, and more. Indeed, solution residues are one subset of forms that may be encountered in an ambient desorption (AD) protocol. The LS-APGD is the only such device that has proven applicability to AD with optical emission spectroscopy (OES) analysis. A 25-component matrix of experimental variables was evaluated in a design-experiments (DOE) approach to identify critical elements controlling AD-LS-APGD-OES performance; most prominently applied mass and the surface density of the residue material. Three primary difficulties have been identified and addressed in preparing residue samples for AD analysis in general; sample visualization, limited sample utilization, and overall imprecision. The issue of residue visualization was addressed by the simple addition of a simple dye (such as food coloring) to the test solution. Issues of poor utilization and irreproducibility were addressed through the implementation of a hydrophobic support (PDMS-coated glass), which limits non-uniform wetting of the surface along with constricting the liquid/residues to smaller regions. Ultimately, sub microgram quantities of Pb could be detected reproducibly. While better yet precision (and sensitivity) are still desired, it is clear that the implementation of the hydrophobic supports is working towards the proper direction. While this study was

done with LS-APGD as the source, the sample preparation method here would be expected to benefit other ambient desorption techniques as well. Though the difference in sampling/ionization mechanism would require further studies. Additional means of increasing the capabilities of the method will involve the use of spatially-resolved sampling of the microplasma, the potential use of carriers/releasing agents akin to those if graphite furnace atomic absorption, or perhaps radio frequency (rf) powering of the microplasma.

3.6 Acknowledgements

This work was supported by the Defense Threat Reduction Agency, Basic Research Award #HDTRA1-14-1-0010, to Clemson University. Thanks to Ms. Paige Reed of the research group of Professor Carlos Garcia in this department for the preparation of PDMS coated glass slides. Additionally, to Mr. Russell Reynolds of the Physics Department instrument shop at this university for the preparation of metal wells.

3.7 References

1. X. D. Hou and B. T. Jones, *Microchem. J.*, 2000, **66**, 115-145.
2. V. Karanassios, *Spectrochim. Acta B*, 2004, **59**, 909-928.
3. R. Costa, *Crit. Rev. Anal. Chem.*, 2014, **44**, 299-310.
4. S. v. Le Gac and A. v. d. Berg, *Miniaturization and mass spectrometry*, RSC Publishing, Cambridge, UK, 2009.
5. R. B. Cody, J. A. Laramee and H. D. Durst, *Anal. Chem.*, 2005, **77**, 2297-2302.
6. J. T. Shelley and G. M. Hieftje, *J. Anal. At. Spectrom.*, 2011, **26**, 2153-2159.
7. S. Ehlert, J. Holzer, J. Rittgen, M. Putz, R. Schulte-Ladbeck and R. Zimmermann, *Anal. Bioanal. Chem.*, 2013, **405**, 6979-6993.
8. R. M. Alberici, R. C. Simas, G. B. Sanvido, W. Romao, P. M. Lalli, M. Benassi, I. B. S. Cunha and M. N. Eberlin, *Anal. Bioanal. Chem.*, 2010, **398**, 265-294.
9. G. A. Harris, A. S. Galhena and F. M. Fernandez, *Anal. Chem.*, 2011, **83**, 4508-4538.
10. Z. Takats, J. M. Wiseman and R. G. Cooks, *J. Mass. Spectrom.*, 2005, **40**, 1261-1275.
11. J. M. Wiseman, D. R. Ifa, Y. X. Zhu, C. B. Kissinger, N. E. Manicke, P. T. Kissinger and R. G. Cooks, *P. Natl. Acad. Sci. USA*, 2008, **105**, 18120-18125.
12. P. M. Kumara, A. Srimany, S. Arunan, G. Ravikanth, R. U. Shaanker and T. Pradeep, *Plos One*, 2016, **11**.
13. B. Nickerson, *Sample preparation of pharmaceutical dosage forms: challenges and strategies for sample preparation and extraction*, Springer, New York, 2011.
14. A. E. Contini, A. J. Bellamy and L. N. Ahad, *Propell. Explos. Pyrot.*, 2012, **37**, 320- 328.
15. A. Uuskula, R. Heimer, J. DeHovitz, K. Fischer and L. A. McNutt, *J. Infect. Dis.*, 2006, **193**, 455-457.
16. D. R. Parkinson, J. M. Warren and J. Pawliszyn, *Anal. Chim. Acta.*, 2010, **661**, 181-187.
17. M. R. Webb and G. M. Hieftje, *Anal. Chem.*, 2009, **81**, 862-867.
18. P. Jamroz, K. Greda and P. Pohl, *Trac-Trend Anal. Chem.*, 2012, **41**, 105-121.
19. P. Pohl, P. Jamroz, K. Swiderski, A. Dzimitrowicz and A. Lesniewicz, *Trac-Trend Anal. Chem.*, 2017, **88**, 119-133.
20. W. C. Davis and R. K. Marcus, *J. Anal. Atom. Spectrom.*, 2001, **16**, 931-937.
21. W. C. Davis and R. K. Marcus, *Spectrochim. Acta B*, 2002, **57**, 1473-1486.
22. R. K. Marcus, B. T. Manard and C. D. Quarles, *J. Anal. At. Spectrom.*, 2017, **32**, 704-716.
23. E. D. Hoegg, C. J. Barinaga, G. J. Hager, G. L. Hart, D. W. Koppenaal and R. K. Marcus, *J. Am. Soc. Mass. Spectr.*, 2016, **27**, 1393-1403.
24. R. K. Marcus, C. D. Quarles, C. J. Barinaga, A. J. Carado and D. W. Koppenaal, *Anal. Chem.*, 2011, **83**, 2425-2429.
25. L. X. Zhang and R. K. Marcus, *J. Anal. Atom. Spectrom.*, 2016, **31**, 145-151.
26. L. X. Zhang, B. T. Manard, B. A. Powell and R. K. Marcus, *Anal. Chem.*, 2015, **87**, 7218-7225.

27. R. K. Marcus, C. Q. Burdette, B. T. Manard and L. X. Zhang, *Anal. Bioanal. Chem.*, 2013, **405**, 8171-8184.
28. R. K. Marcus, H. W. Paing and L. X. Zhang, *Anal. Chem.*, 2016, **88**, 5579-5584.
29. H. W. Paing and R. K. Marcus, *J. Anal. At. Spectrom.*, 2017, **32**, 931-941
30. A. Bodzon-Kulakowska, A. Drabik, M. Marszalek, J. H. Kotlinska and P. Suder, *J Mass. Spectrom.*, 2014, **49**, 613-621.
31. Y. S. Shin, B. Drolet, R. Mayer, K. Dolence and F. Basile, *Anal. Chem.*, 2007, **79**, 3514-3518.
32. N. E. Manicke, J. M. Wiseman, D. R. Ifa and R. G. Cooks, *J. Am. Soc. Mass. Spectr.*, 2008, **19**, 531-543.
33. K. J. Kim, Y. W. Kim, H. G. Park, C. H. Hwang, I. Y. Park, K. Y. Choi, Y. H. Yang, Y. H. Kim and Y. G. Kim, *J. Ind. Eng. Chem.*, 2017, **46**, 150-156.
34. C. A. Schneider, W. S. Rasband and K. W. Eliceiri, *Nat. Methods*, 2012, **9**, 9671-675. 35.
35. D. R. Ifa, C. P. Wu, Z. Ouyang and R. G. Cooks, *Analyst*, 2010, **135**, 669-681.
36. D. C. Montgomery, *Design and analysis of experiments*, John Wiley, New York, 5th edn., 2001.
37. A. Pasqualato, V. Lei, A. Cucina, S. Dinicola, F. D'Anselmi, S. Proietti, M. G. Masiello, A. Palombo and M. Bizzarri, *Cell Adhes. Migr.*, 2013, **7**, 450-459.

CHAPTER IV

RAPID DETERMINATION OF URANIUM ISOTOPIC ABUNDANCE FROM COTTON SWIPES: DIRECT EXTRACTION VIA A PLANAR SURFACE READER AND COUPLING TO A MICROPLASMA IONIZATION SOURCE

4.1 Abstract

The collection of solid particulates and liquids from surfaces by the use of cloth swipes is fairly ubiquitous. In such methods, there is a continuous concern regarding the ability to locate and quantitatively sample the analyte species from the material. In this effort, we demonstrate the initial coupling of an Advion Plate Express plate reader to a liquid sampling – atmospheric pressure glow discharge (LS-APGD) microplasma ionization source with an Orbitrap mass spectrometer to perform uranium isotopic analyses of solution residues on cotton swipes. The Plate Express employs a sampling probe head to engage and seal against the swipe surface. Subsequentially, the analyte residues are desorbed and transported within a 2% HNO_3 electrolyte flow to the ionization source. Quantitative recoveries were observed following a single 30 s extraction step, with the absolute mass sampled per extraction being ~100 ng. While the intrasample variability in the analytical responses for triplicate sampling of the same swipe yield ~30% RSD, this lack of precision is offset by the ability to determine isotope ratios for enriched uranium specimens with a precision of better than 10% RSD. Pooled, inter-sample precision (n=9) was found to be <5 %RSD across the various sample compositions. Finally, 235U/238U determinations (ranging from 0.053 – to – 1.806) were accurate with errors of <10%, absolute. The ^{234}U- and ^{236}U-inclusive ratios were determined with similar accuracy in enriched samples. While the driving force for the effort is in the realm of nuclear non-

proliferation efforts, the ubiquitous use of cloth swipes across many application areas could benefit from this convenient approach, including the use of versatile, reduced-format mass spectrometer systems.

4.2 Introduction

Direct sampling of solids for elemental or isotopic spectrochemical analysis offers the possibility of eliminating lengthy sample preparation techniques such as simple dissolution, acidic/heat driven digestion, and chemical separation commonly employed for trace analysis.[1-2] Among the widely applied direct solids methods, laser ablation (LA) sampling is considered the most versatile in terms of the scope of materials that can be sampled. LA involves the focusing of a pulsed laser onto the solid sample surface, forming a plasma which subsequentially removes a small portion of the material present.[3-4] This plasma can be optically characterized for elemental analysis via laser induced breakdown spectroscopy (LIBS),[5-9] or the ablated particles can be sent into an inductively coupled plasma - mass spectrometer (ICP-MS)[10-12] for elemental and isotopic analysis. The ability to obtain point-by-point elemental and isotopic maps of virtually any material is applicable to diverse areas, ranging from geology[13-14] to electronic materials[15-16] and neurobiology.[17-18] One particularly attractive use of LA sampling is in the analysis of discrete particles, such as found on filters of various form; i.e. single particle analysis in biological[19-20] and nuclear safeguard samples.[12, 21-22]

While spatial mapping is one of the inherent advantages of LA-based methods, the ability to find species of interest on a surface can prove challenging. There is also an issue of the overall level to which such microanalyses are representative of a "bulk" sample.

Automated laser rastering methods[23-25] have been developed that offer "total" coverage over a certain area of a sample, increasing the likelihood of identifying relevant species. Here, there may well be tradeoffs in terms of moving from a situation of under-sampling (small spot size vs. large sample area) to one of over-sampling (consuming large amounts of open space). Indeed, there are situations where particle populations need to be characterized as an ensemble, not requiring a per particle assay. In these situations, some form of homogenization or digestion may be the most expeditious approach. The development of a liquid probe that can directly sample material on a surface and subsequently transport it to an ionization source for elemental/isotopic analysis, without the need for bulk digestion and purification, would provide a much-needed tool for inorganic analysis. Bypassing chemical digestion steps would drastically speed up analysis and possibly open up the option of in-field measurements of environmental samples.

As part of its verification mission under the Nuclear Non-Proliferation Treaty, the International Atomic Energy Agency (IAEA) utilizes environmental sampling during onsite inspections of nuclear facilities to verify declared activities and to detect the presence of undeclared nuclear activities and materials.[26-28] A typical environmental sample consists of a 4" x 4" cotton swipe that is wiped over surfaces to collect trace amounts (particulates) of nuclear material that are indicative of activities that have occurred in the facility. (While the example here deals with nuclear safeguards, the general approach of swipe sampling is common in many industrial and environmental scenarios.[29-33]) These swipe samples are then distributed to IAEA's international Network of Analytical Laboratories (NWAL) for analysis, with a focus on quantification and isotope ratio

measurements of the uranium and plutonium on the swipe using multi-collector inductively coupled plasma mass spectrometry (MC-ICP-MS), multi-collector thermal ionization mass spectrometry (MC-TIMS), or large geometry secondary ion mass spectrometry (LG-SIMS).[34] The very nature of these instruments requires their housing in laboratory facilities that may be far-removed from collection locations, posing challenges in terms of sample transport and overall time-to-results. Ultimately, these methods yield highly accurate and precise results, but the chemical purification steps necessary prior to analysis of swipes by both methods are time consuming.[35] Methods which would provide more facile sampling of the swipes would be advantageous. While the focus here is on an IAEA application, other agency/associations address the use of swipe sampling of radiological materials (i.e., α and γ-emitters),[36-37] but are not directly relevant to trace/isotope ratio analysis of long-lived U species. The liquid-sampling atmospheric glow discharge (LS-APGD) microplasma, when coupled to Orbitrap-type mass spectrometers, has proven to be capable of meeting various requirements for determining uranium isotope ratios for the purpose of nuclear safeguards.[38-40] The LS-APGD's low power, small footprint, and low sample consumption makes it readily adaptable with mass analyzers normally employed in the realm of molecular mass spectrometry,[41] providing greater flexibility in sampling options. Likewise, the device uniquely operates as a combined atomic and molecular (CAM) ionization source.[42-44] In particular, Orbitrap instruments can provide mass resolution far higher than multi-collector systems (m/Δm of ~70,000 vs. 10,000) on a tabletop format. A recent multi-laboratory comparison including the LS-APGD/Orbitrap instrument, MC-TIMS, and scanning sector-field ICP-MS showed very comparable isotope ratio (IR)

performance in terms of the measurement uncertainties, particularly in the case of enriched uranium isotopic analyses.[40] In all, the operational overhead and operator sophistication are far reduced for the LS-APGD/Orbitrap versus the benchmark instruments, making the requirements of the housing laboratories far less stringent, potentially eliminating the need to transport critical samples to NWAL facilities.

The LS-APGD/Orbitrap combination is evaluated here towards the analysis of swipes as necessary for safeguards applications. There have been two previous approaches to direct surface analysis utilizing the LS-APGD. Analyte surfaces can be probed through the use of laser ablation (LA-LS-APGD)[45-46] or the surface can be sampled directly through an ambient desorption (AD) process.[47-48] LA into the microplasma suffers the same disadvantages as other laser-based techniques such as small sampling area and increased complication. While AD-LS-APGD is capable of directly analyzing the surface with a reasonably large sampling area (~4 mm^2), the thermal component of the plasma causes the cotton swipes to burn. Therefore, an alternative approach to the direct swipe sampling into the ionization source is required. Specifically, we demonstrate for the first time the use of an Advion Plate Express thin layer chromatography (TLC) plate reader to sample immobilized uranium particulates directly from a cotton swipe. The Advion Plate Express is an automated solvent extraction probe that is typically utilized to extract solutes from TLC plates into a mobile phase that is fed to electrospray ionization sources. Here the particulate material is dissolved from the swipe surface by the standard 2% nitric acid carrier solvent flow into the LS-APGD microplasma coupled to an Orbitrap mass spectrometer for uranium isotope analysis. The preliminary operational and analytical

characterization of this coupling is presented for the rapid (<1 min) determination of $^{235}U/^{238}U$ ratios for various uranium isotopic standards deposited on relevant swipe materials. Detection of the $^{234}U/^{238}U$ and $^{236}U/^{238}U$ minor isotope ratios was shown to be feasible in the case of enriched samples. Given the ubiquitous use of cloth swipes across many application areas, this convenient approach to sampling could find diverse applications.

4.3 Methods and materials

4.3.1 Instruments

4.3.1.1 LS-APGD ionization source

The LS-APGD and Plate Express coupling, shown in Fig. 4.1, is interfaced to a Thermo Scientific Q Exactive Focus (San Jose, CA, USA) mass spectrometer. The operations and geometry of the LS-APGD has not changed since previous iterations.[39-40] A Spellman high-voltage power supply (Spellman High Voltage Electronics Corporation, Hauppauge, NY, USA) provides a positive potential at a fixed current of 30 mA to the solid stainless steel counter electrode (MDC Vacuum Products, Hayward, CA, USA) that sits perpendicular to the grounded cathode (solution electrode). The solution electrode is composed of a stainless steel outer capillary (880 µm i.d., 1600 µm o.d., Restek Corporation, Bellefonte, PA, USA) with a nested fused silica inner capillary (280 µm i.d., 580 µm o.d., Restek Corporation, Bellefonte, PA, USA). Flow of helium gas is delivered at a rate of 0.5 L min-1 between the stainless steel outer capillary and the silica inner capillary and regulated by a mass flow controller (Alicat Scientific MC Series, Tucson, AZ). Electrolytic solution consisting of 2% (v/v) HNO_3 is prepared by diluting

concentrated nitric acid (Trace metal grade, Sigma-Aldrich, St. Louis, MO, USA) with DI - H2O (Purelab Flex, ELGA WaterLab, High Wycombe, UK). The solution is pumped through the silica inner capillary at a constant flow rate of 30 µL min^{-1} by a syringe pump (Chemyx Fusion 100, Stafford, TX, USA). Based on previous efforts in uranium isotope ratio determinations,[39-40] the discharge conditions were held constant across these experiments: He sheath gas flow rate = 0.5 L min^{-1}, discharge current = 30 mA, and an interelectrode gap = 2 mm

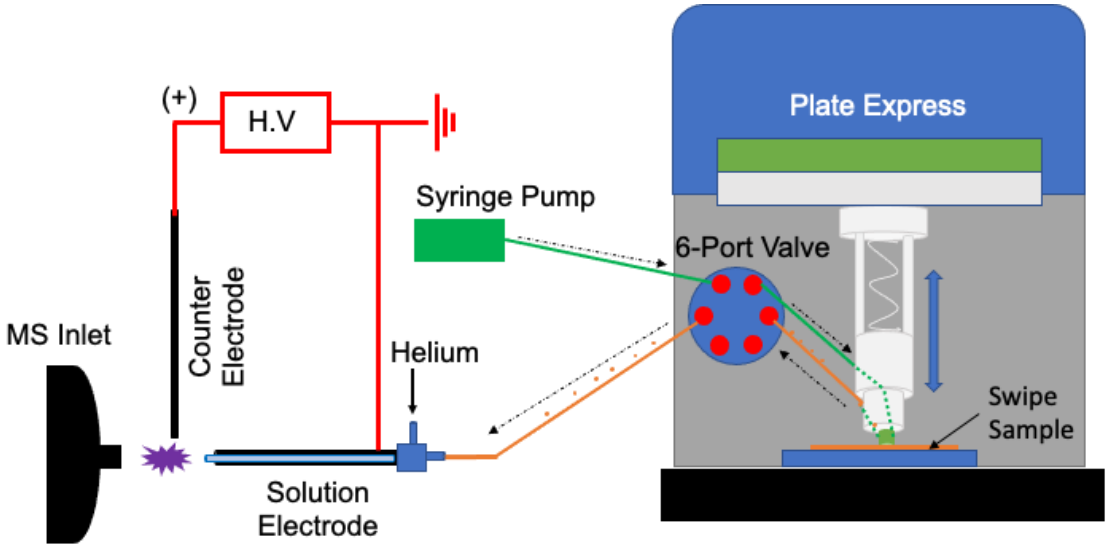

Figure 4.1 A diagrammatic representation of the LS-APGD-MS source components coupled to the Plate Express. Plasma conditions are 30 µL min^{-1} solution flow, 0.5 L min^{-1} gas flow, 30 mA, and ~ 2 mm electrode gap with the plate express during an extraction event where the solution is diverted towards the extraction assembly.

4.3.1.2 Advion Plate Express

The Advion (Ithaca, NY) Plate Express is utilized for the sampling of swipes (4 x 4", Texwipe, Kernerville, NC, USA) and positioned between the LS-APGD and the syringe pump, with the normal electrolytic solution used here as the extraction solvent. In non-sampling operations the electrolytic solution enters the 6 – port valve of the Plate Express

and exits to the LS-APGD without interacting with the swipe. During the extraction event, as depicted in Fig. 4.1, the microextractor probe head presses down onto the sample (swipe), creating a seal between probe head and the surface. The flow of electrolytic solution is diverted towards the probe head where it exits out of an orifice and interacts with the swipe surface and analyte particles where the acidic solvent effectively dissolves the particulates before flowing up into a different capillary of the elution head. The electrolytic solution flows to the LS-AGPD, carrying the extracted analyte, in much the same way as a standard sample injection loop would be employed. A gas purge is applied to clear remnant solution from the pump head in between sampling events. To minimize contamination and clogs in the elution head, the frit located in the elution head was washed after each swipe's assay was completed. The operational parameters of the Plate Express (extraction force, extraction time) are controlled though the Mass Express software (Advion, Ithaca, NY,USA) and the extraction event is initiated through an external switch connected to the Plate Express.

4.3.2 Materials

Three isotopic standard swipes were prepared utilizing U050, U500, and U630 solutions (New Brunswick Laboratory (NBL), Argonne, IL). A set of three native swipes (without solution) were employed as blanks. The samples and their uranium concentration, deposited uranium mass, and $^{235}U/^{238}U$ isotope ratios are given in Table 4.1. Four sets (NBL U050, U500, U630, and a blank) of three replicates (A,B,C), of uranium isotope swipes were prepared by pipetting 100 µL of uranium isotopic solutions of varying enrichments onto TX304 cotton swipes at the Oak Ridge National Laboratory in the

following manner. The center of the individual cotton swipes was suspended over the opening of plastic beakers and secured on top of each beaker by wrapping a clean elastic band around the peripheral of the swipes. The wipe assembly was tared on a 5 – decimal analytical balance. After slowly pipetting the 100 µL solution to the center of the swipe, the solution wicked to a circular shape with a radius of ~1.7 cm. It is important to note that the solution boundary never came into contact with the edge of the beakers. Thus, an assumption is made that no uranium solution is lost to the beaker. The wipe assembly was then allowed to dry overnight. The measured uranium loading is provided in Table 4.1. The dried swipes were then removed from the beakers, folded inward into quarters, and placed in polypropylene zip-bags.

Table 4.1 Sample name of uranium swipes, total uranium mass, their associated concentration on swipe, and isotope ratio. The mass deposited was determined gravimetrically rather than relying on the volume-based value.

Sample #	Total U Mass (µg)	~ U concentration (µg cm^{-2})	^{235}U µg/ ^{238}U µg
NBS U050 - A	73.6	7.65	0.05
NBS U050 - B	73.6	7.65	
NBS U050 - C	73.5	7.65	
NBS U500 - A	40.9	4.26	1.00
NBS U500 - B	40.8	4.24	
NBS U500 - C	41.0	4.26	
NBL U630 - A	19.6	2.04	1.807
NBL U630 - B	19.7	2.05	
NBL U630 - C	19.7	2.05	

Five swipes doped with depleted uranium, prepared at Clemson University, were employed in the method development stages of the effort. A 100 µL aliquot of 1000 mg L-1 uranium solution, prepared from uranyl nitrate hexa-hydrate salt (International Bio-analytical Industries, Inc., FL, USA), was pipetted onto TX304 cotton swipes suspended

over beakers, as described above. This procedure gives an approximate mass of 100 µg on the swipe with a concentration of 10.41 µg cm^{-2}. Standard food-color dyes were added to the test solutions to visually determine the location of the deposited residues to allow proper positioning under the probe head.

4.4 Results and discussion

4.4.1 Plate Express elution parameters

The Plate Express control software allows the user to vary the applied force of the probe head and the extraction time. The applied force of the elution head is the detected force applied by the engaged probe head during the course of the extraction event. The necessary applied force depends heavily on the type of substrate being sampled; the force must be high enough for the knife edge to seal to the sample, and thus ensure continuous, quantitative solution flow, yet it cannot be so high as to create a leak by cutting/cracking the substrate or damaging the knife edge itself. The applied force was empirically set to 100 N at the beginning of the experiments based on its being the lowest force providing a significant seal to the swipes without damaging the probe knife edge.

The optimal extraction time was determined based on the integrated intensity of the $^{238}UO_2$ at 270 m/z transient peaks during the extraction of depleted uranium on multiple method development swipes. An example set of transients for $^{238}UO_2$ at extraction/sampling times of 5 – 60 s is shown in Fig. 4.2. In each trace, an initial pulse is seen in the spectral background, which corresponds to the switching of the valve from the by-pass mode to the probe head. The slight variations in the temporal profiles reflects differences in the probe head and transfer line dead volumes that are filled with solvent as

the head is engaged. (Note: based on the solution flow rates, these differences are on the 10 μL.) The onset of the analyte response is seen to occur ~1.5 minutes after the engagement, reflective of the transport path as the solution goes through the probe head and to the ion source. The increased responses in extraction times from 5-to-30 s are very pronounced. Beyond 30 s, the average intensity increases slightly with extraction time. Thus, there may be very little benefit to using extraction time above 30 sec. As presented in the included table, the extraction-to-extraction varies from ~20 - 30 %RSD for the transients at extraction times of 30 s and above. The main cause in the variability is likely the heterogeneity of the sample deposition process and probing of different locations within the sample. As the extracted mass of uranium is dependent upon the location sampled on the swipe, the main contribution of standard deviation comes from the distribution of the

analyte across the swipe. That said, as the purpose of this effort is to obtain precise U isotope ratios, this variability in raw signal for a single isotope may be of no consequence.

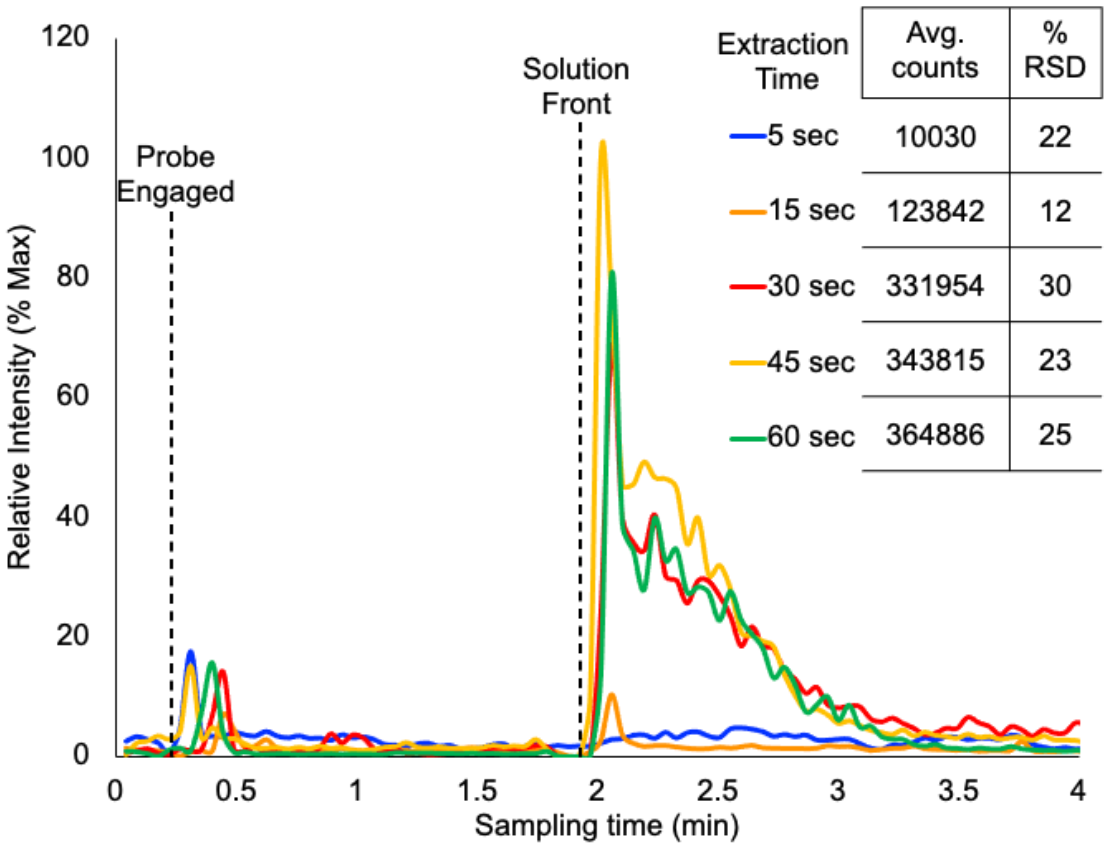

Figure 4.2 Example transients at an extraction time of 5 s (blue),15 s (orange), 30 s (red), 45 s (yellow), and 60 s (green) of m/z = 270 ($^{238}UO_2$) from depleted uranium swipes. Average integrated response and repeatability for triplicate samplings provided.

There are two different factors to consider when discussing the influence of extraction time. First, the elution head must be in the extraction position long enough for the extraction solution to not only interact with the sample but also for the analyte-containing solution to travel across the elution assembly "loop" and into the flow path leading to the LS-APGD, i.e., long enough before the automated valving switches the flow of the carrier solution away from the elution probe loop. It was empirically determined that the 5 s sampling here was too short to allow any eluted uranium to pass the loop to the

microplasma flow. Second, the extraction solution must interact with the sample long enough for the uranium to be quantitatively removed from the swipe. It is not clear at this point whether or not analyte removal is a two-step process wherein whole particulates are removed via turbulent flow and then dissolved, or if the particles are dissolved in-place.

Regardless of the specific mechanism of analyte extraction, it appears that an extraction time of 30 s is sufficient to achieve high recoveries under this set of solvent flow conditions. Here again, it is emphasized that the flow rate of 30 μL min^{-1} is chosen for the sake of expediency as that is the preferred electrolyte flow rate for high precision isotopic analysis. That said, the use of different flow rates/times/solvent compositions during the extraction process might yield improved recoveries or higher throughput. Under such a situation, one could envision a two-step process to optimize both the extraction and the analysis steps. Certainly, future parametric studies on the coupling of the Plate Express to the LS-APGD should lead not only to further understanding of the extraction process, but also improved analytical response.

4.4.2 Recovery of uranium residues from swipes

As suggested by the shapes of longer transients presented in Fig. 4.2, it appears that there is a reasonable certainty that the removal of material from the swipes may be close to quantitative. For practicality sake, it is imperative to know whether or not the uranium content on the swipe is exhausted after a single extraction event or if multiple extraction events are required. To test for this, swipe U500 - A was sampled five times in the same probing position. The elution head was examined after each extraction to ensure no clogging occurred. Figure 4.3 shows a "stitched" transient measurement over the five

consecutive extraction events at m/z 267, corresponding to $^{235}UO_2$ peak. The transients are not blank subtracted. Clearly, the first extraction event closely mimicks those Fig. 4.2, with the transient response retreating to background levels in ~1 min. Each of the subsequent extraction events lead to no significant signals above background levels. This indicates that the vast majority of the uranium deposited in that location has been removed through the first extraction event. In addition, the lack of significant signals in the subsequent extractions suggests that there is minimal carryover of the analyte. The possibility of uranium memory effects might have been expected as previous work utilizing the LS-APGD coupled to the Q-Exactive Focus for direct injections of uranium-containing solutions did suffer from carryover for time frames of minutes.40 In fact, uranium sorption to metal surfaces, such as mass spectrometer ion lenses, is well known.[49]

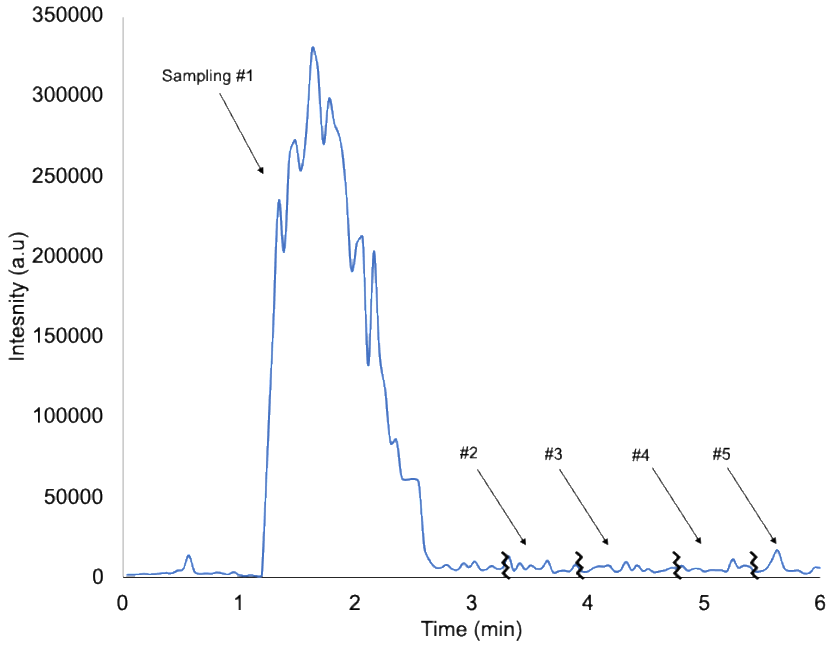

Figure 4.3. A stitched transient at m/z = 267 ($^{235}UO_2$) from swipe NBS U500 – A from five consecutive extraction events on the same location of the swipe.

To ensure that background influences on the acquired spectra were minimized, a blank swipe was sampled in between consecutive analyses of each uranium swipe, such that the sequence of analysis was blank- U630 swipe A – blank –swipe A – blank - swipe A - blank. This was followed by the same progression for U630 swipes B and C, then U500 A-C, and U050 A-C. The blank response was subtracted from the analyte response for all studies. The blank before the analysis of the first U630 swipe had a $^{235}U/^{238}U$ ratio of 0.002, reflecting a presence of the ^{238}U from previous analyses and a ^{235}U signal very close to the LOD. The isotope ratio of the blanks in between the U630, U500, and U050 samples were approximately 0.1, 0.04, and 0.1 indicating a slight memory/carryover effect as the enriched-ratio swipes were analyzed.

4.4.3 Intra- and Intersample Isotope Ratio Characteristics Determined from NBL U630, U500, and U050

One of the primary driving forces for this development was the ability to rapidly determine uranium isotope ratios from swipes. Gold standard methods used for the determination of U isotope ratios in swipes typically have on roughly 1% accuracy and precision; however, these methods require labor-intensive preparation methods that take days to weeks to complete. For the method described herein, the target levels for this proof of concept work were on the order of ~5%, values commensurate with sampling directly from collection media with no a priori radionuclide separation. Sufficient data was collected to allow for determination of accuracy and precision as illustrated subsequently.

Figure 4.4a presents typical mass spectra acquired for swipes prepared by depositing solutions of U630 (yellow), U500 (red), and U050 (blue), decreasing in order

of the extent of enrichment. As expected from utilizing a high-resolution mass spectrometer such as the Orbitrap, the peaks are well defined with no spectral interferences. Figure 4.4b provides an approximately 50x scale expansion of the U630 spectrum (designated as U630-A), highlighting the ^{234}U and ^{236}U oxide species' signals. Here again the spectra are clean in composition, with the level of sensitivity of the measurements suggested by the high signal-to-background levels. Given that the Plate Express probe head has an approximate sampling area of 8 mm^2 (~4 mm x 2 mm), versus the original deposition area of ~908 mm^2 and the total mass of deposited uranium is 19.6 µg, the spectrum shown correlates to ~0.001, 0.103, 0.002, and 0.058 µg of ^{234}U,^{235}U,^{236}U, and ^{238}U, respectively. This is of course under the assumption of an even distribution of analyte across the sampling area and that the entirety of the uranium mass was extracted. However, depending upon the location on which the swipe was sampled, the actual mass of uranium

extracted can be expected to vary. Even with these caveats, the sensitivity demonstrated here for this coupling is very encouraging.

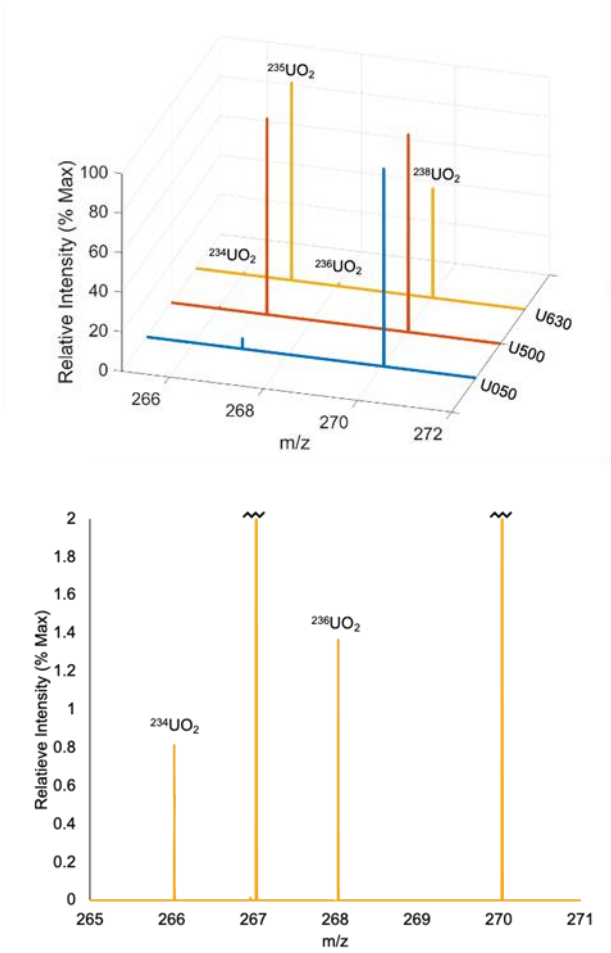

Figure 4.4. a) Mass spectra of extraction of swipes NBL U630 – A (yellow), NBS U500 – A (red), and NBS U050-A (blue). Labeled are isotopes $^{235}UO_2$, and $^{238}UO_2$. b) ~50 x expansion of NBL U630 – A mass spectrum highlighting minor $^{234}UO_2$ and $^{236}UO_2$ responses.

While the deposition and sampling of the deposited uranium may be subject to a high level of variability in the absolute recoveries, the intention here is the ability to obtain the targeted isotope ratio performance. Table 4.2 shows the comparison between the expected isotope ratio and the average isotope ratios of $^{234}U/^{238}U$, $^{235}U/^{238}U$ and $^{236}U/^{238}U$ across three extractions of the sample U630 – A. To determine the isotope ratio, an

averaged spectrum was acquired from the 20 individual mass spectra taken during the extraction event. The spectral processing range across the transient was initiated at the point wherein the $^{238}UO_2$ signal reach 15% of the eventual maximum and likewise terminated when it decreased to that level. Experimentally determined isotope ratios were calculated by taking the area of the uranium peak of interest over the area of the peak of $^{238}UO_2$ from the averaged spectrum of each extraction event. The average isotope ratio was determined by averaging the isotope ratio of interest of the three individual extraction events on sample U630 – A, with a standard deviation of the values calculated across the triplicate samplings. The percentage absolute error in the determined values of the isotope ratios was calculated as

$$\%\ Error = \left(\frac{|Expected\ isotope\ ratio - Average\ isotope\ ratio|}{Expected\ Isotope\ Ratio}\right) * 100$$

with the magnitude of the error reflecting the over- or under-estimation. It is demonstrated here that each of the target uranium isotope ratios fell around or below 10% error without correction for mass bias, with each ratio slightly underestimated. Importantly, the technique also demonstrates an intrasample relative standard deviation (RSD) of less than 10% for the triplicate measurements of sample U630 - A. As would be desired, and anticipated, the precision of the determined isotope ratios is far better than the single-isotope ($^{238}UO_2$) analytical recoveries presented in Fig. 4.2 (<10 %RSD vs. 20 – 30% RSD). Finally, the determined isotope ratios for triplicate analyses of these swipes are very respectable, with the greatest errors being only 11.1% for the ratios inclusive of the ^{234}U and ^{236}U isotopes.

Table 4.2. The expected and determined isotope ratios of ^{234}U,^{235}U,^{236}U to ^{238}U isotopes for triplicate extractions of sample U630-A.

	Expected Ratio	Average Isotope Ratio	% Error	Standard Deviation	%RSD
$^{234}U/^{238}U$	0.018	0.016 ± 0.0006	-11.1	0.001	6.25
$^{235}U/^{238}U$	1.807	1.679 ± 0.0808	-7.03	0.140	8.25
$^{236}U/^{238}U$	0.027	0.024 ± 0.0012	-11.1	0.002	8.0

The key $^{235}U/^{238}U$ isotope ratios were determined for triplicate extraction sampling events across three swipes prepared from U630, U500, and U050 solution aliquots. The determined isotope ratios for each measurement (dots), expected isotope ratio (dashed line), and average determined isotope ratio (n=9) (solid line) for U630 (orange), U500 (red), and U050 (blue) swipes is shown in Fig. 4.5. Table 4.3 presents the cumulative isotope ratio statistics for the pooled analyses of the three swipe sample compositions. Generally, the average percentage RSD values within the triplicate samplings of each swipe were ~7%, while the determined ratios between the three swipes of the same isotopic composition varied by <5 %RSD. Finally, the percentage error in the determined isotope ratios falls below 10% for each of the samples. In every case, the percentage error is less than the 10% target value, with the determined precision of the measurements better than 5 %RSD. The determined $^{235}U/^{238}U$ values for the U500 samples are somewhat overestimated, while those for U050 and U630 are underestimated, with no clear determinate trend. As a reminder, each set of isotopic measurements was blank-corrected, with those intensities not appearing to be correlated with sample type, indicating the cause of error is not likely related to blank or instrument memory effect. That said, the use of the blank correction seems not to have adverse effects regarding the measurement precision. The specific sources of these errors are not known at this point, but in general, this level of

accuracy without the explicit use of any sort of mass bias correction or isotope dilution approaches as are typical in isotope ratio mass spectrometry, is quite encouraging.

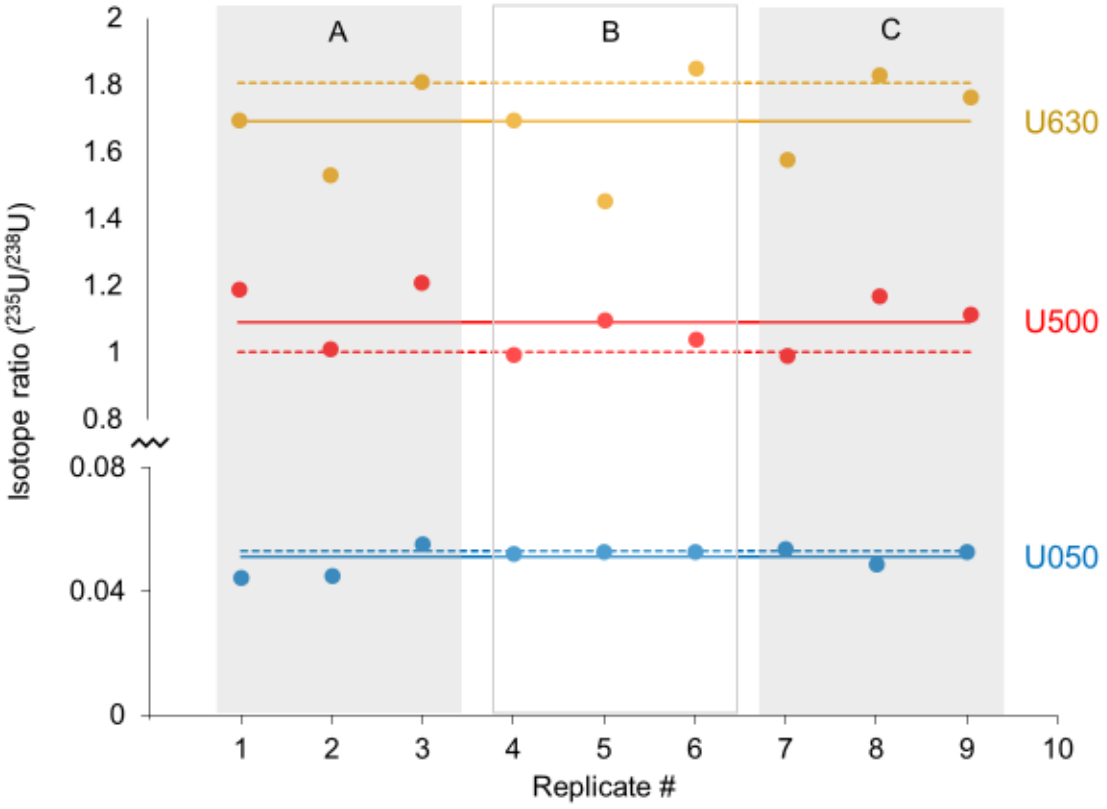

Figure 4.5 Plot of isotope ratios for triplicate samplings (plotted individually) of swipes A, B, C of U630 (orange), U500 (red) and U050 (blue). Filled lines represent the average across all nine extraction events while the dashed lines represent the expected values.

Table 4.3 Cumulative isotope ratio figures of merit for triplicate plate reader extractions each across three swipe samples prepared from isotopic standards U630, U500, and U050. (n=9 measurements).

Standard	Expected $^{235}U/^{238}U$	Determined $^{235}U/^{238}U$	% Error	Standard Deviation	% RSD
U630	1.807	1.690 ± 0.0100	-6.45	0.030	1.77
U500	1.000	1.091 ± 0.0155	9.07	0.047	4.31
U050	0.053	0.051 ± 0.0008	-3.82	0.002	3.92

4.5 Conclusion

The collection of solid particulates and liquids from surfaces by the use of cloth swipes is fairly ubiquitous. In such methods, there is a continuous concern about the ability to locate and quantitatively sample the analyte species from the material. In this effort, an Advion Plate Express is coupled to a LS-APGD microplasma ionization to perform uranium isotopic analyses of solution residues deposited on cotton swipes. The Plate Express employs a probe head to engage and seal against the swipe surface, with the analyte residues desorbed and carried to the ionization source in the standard 2 % HNO_3 electrolyte flow to the source. Quantitative recoveries were observed following a single 30 s extraction step, with the mass sampled per extraction step being on the order of 0.17 μg. While the intrasample variability in the analytical responses for triplicate sampling of the same swipe yield was ~30 %RSD, this lack of precision is offset by the ability to determine isotope ratios for enriched uranium specimens with a precision of better than 10% RSD. Pooled, intersample precision (n=9) was found to be <5 %RSD across the various sample compositions. Finally, $^{235}U/^{238}U$ determinations (ranging from 0.053 – to – 1.806) were accurate with errors of <10%, absolute. It is fully acknowledged that far greater experimental rigor and repetitions will be needed to provide a full assessment of sources of error and variability. Only after such an evaluation can the true applicability within the safeguards tool-box be determined.

Based on the demonstrated capabilities of this technique in these preliminary studies, future studies will focus on improving the sampling aspects as well as further methods to improve analytical performance. The extraction conditions used here were

fixed to those used in the standard LS-APGD-MS analysis of solutions. The mechanism of the extraction event will be further explored by varying solvent composition, flow rates, and chemical imaging the surface of the swipe after the extraction event. Further understanding of the mechanism could lead to not only improvement in terms of accuracy and precision, but potentially means of speciation of the uranium analytes. Ultimately, a design-of-experiment protocol approach could be applied to determine the best combination of extraction and analysis conditions.

There exists a number of options to improving the analytical performance of the plate reader/microplasmas coupling in general, and for the application in isotope ratio mass spectrometry in particular. In this regard, one could project sampling particulates directly by this method as opposed to the solution residues employed here. In such a situation, there would be questions as to how representative the probe sampling event might be in quantitative terms. The addition of an internal standard to the eluent flow could be a very effective means of improving the sample-to-sample variability, or at least to understand differences between sample homogeneity and ion source stability contributions. Likewise, standard addition method could be used for enhanced quantification without the need for extensive preparation of analytical standards. Of course, this approach naturally extends to use of isotope dilution (ID) mass spectrometry. Finally, one could include isotopic species which might allow for on-the-fly mass bias corrections. In the realm of nuclear non-proliferation efforts, this approach could be utilized as a screening tool to determine if further NWAL-based testing is required, significantly speed up the workflow process by testing on-site and reduce the need for the sample transport to specialized laboratories. The

ubiquitous use of cloth swipes across many application areas could surely benefit from this convenient approach, including the use of reduced-format mass spectrometer systems. Likewise, the sampling approach itself might be of use in other methods such as ICP-MS analysis. Finally, the approach could be employed with the CAM ionization source to affect analysis of "molecular" species in particulate swipes.[43]

4.6 Acknowledgements

The Clemson University portions of this effort were supported through a collaboration with Advion Inc. This work was supported by the Oak Ridge National Laboratory, managed by UT-Battelle for the Department of Energy under Contract DE-AC05-000R22725.

4.7 References

1. R. C. Machado, D. F. Andrade, D. V. Babos, J. P. Castro, V. C. Costa, M. A. Speranca, J. A. Garcia, R. R. Gamela and E. R. Pereira, *J. Anal. At. Spectrom.*, 2020, **35**, 54-77.
2. M. Resano, F. Vanhaecke and M. T. C. de Loos-Vollebregt, *J. Anal. At. Spectrom.*, 2008, **23**, 1450-1475.
3. B. N. Chichkov, C. Momma, S. Nolte, F. vonAlvensleben and A. Tunnermann, *Appl. Phys. A-Mater.*, 1996, **63**, 109-115.
4. E. G. Gamaly, A. V. Rode, B. Luther-Davies and V. T. Tikhonchuk, *Phys. Plasmas*, 2002, **9**, 949-957.
5. D. W. Hahn and N. Omenetto, *Appl. Spectrosc.*, 2010, **64**, 335a-366a.
6. A. Williams and S. Phongikaroon, *Appl. Spectrosc.*, 2018, **72**, 1029-1039.
7. B. T. Manard, M. F. Schappert, E. M. Wylie and G. E. McMath, *Anal. Methods*, 2019, **11**, 752-759.
8. J. E. Barefield, E. J. Judge, K. R. Campbell, J. P. Colgan, D. P. Kilcrease, H. M. Johns, R. C. Wiens, R. E. McInroy, R. K. Martinez and S. M. Clegg, *Spectrochi.m Acta B*, 2016, **120**, 1-8.
9. R. E. Russo and A. W. Miziolek, *LASER-INDUCED BREAKDOWN SPECTROSCOPY (LIBS) Fundamentals and Applications Preface*, Cambridge Univ Press, Cambridge, 2006.
10. L. Dorta, R. Kovacs, J. Koch, K. Nishiguchi, K. Utani and D. Gunther, *J. Anal. Atom. Spectrom.*, 2013, **28**, 1513-1521.
11. S. Kappel, S. F. Boulyga, L. Dorta, D. Gunther, B. Hattendorf, D. Koffler, G. Laaha, F. Leisch and T. Prohaska, *Anal. Bioanal. Chem.*, 2013, **405**, 2943-2955.
12. A. L. Ronzani, F. Pointurier, M. Rittner, O. Borovinskaya, M. Tanner, A. Hubert, A. C. Humbert, J. Aupiais and N. Dacheux, *J. Anal. At. Spectrom.*, 2018, **33**, 1892-1902.
13. P. K. Mukherjee, A. K. Souders and P. J. Sylvester, *J. Anal. At. Spectrom.*, 2019, **34**, 180-192.
14. L. Arroyo, T. Trejos, P. R. Gardinali and J. R. Almirall, *Spectrochim. Acta B*, 2009, **64**, 16-25.
15. P. Harte, M. Evertz, T. Schwieters, M. Diehl, M. Winter and S. Nowak, *Anal. Bioanal. Chem.*, 2019, **411**, 581-589.
16. S. J. M. Van Malderen, J. T. van Elteren and F. Vanhaecke, *J. Anal. At. Spectrom.*, 2015, **30**, 119-125.
17. J. S. Becker and D. Salber, *Trac-Trends Anal. Chem.*, 2010, **29**, 966-979.
18. M. Cruz-Alonso, B. Fernandez, A. Navarro, S. Junceda, A. Astudillo and R. Pereiro, *Talanta*, 2019, **197**, 413-421.
19. D. Metarapi, M. Sala, K. Vogel-Mikus, V. S. Selih and J. T. van Elteren, *Anal. Chem.*, 2019, **91**, 6200-6205.
20. D. Drescher, C. Giesen, H. Traub, U. Panne, J. Kneipp and N. Jakubowski, *Anal. Chem.*, 2012, **84**, 9684-9688.

21. A. Donard, F. Pointurier, A. C. Pottin, A. Hubert and C. Pecheyran, *J. Anal. At. Spectrom.*, 2017, **32**, 96-106.
22. B. T. Manard, C. D. Quarles, E. M. Wylie and N. Xu, *J. Anal. At. Spectrom.*, 2017, **32**, 1680-1687.
23. D. C. Perdian, S. J. Bajic, D. P. Baldwin and R. S. Houk, *J. Anal. At. Spectrom.*, 2008, **23**, 325-335.
24. D. M. Chew, J. A. Petrus, G. G. Kennya and N. McEvoy, *J. Anal. At. Spectrom.*, 2017, **32**, 262-276.
25. B. Jackson, S. Harper, L. Smith and J. Flinn, *Anal. Bioanal. Chem.*, 2006, **384**, 951-957.
26. D. J. Donahue, T. H. Zabel, A. J. T. Jull, P. E. Damon and K. H. Purser, *Radiocarbon*, 1983, **25**, 719-728.
27. D. L. Donohue, *J. Alloys. Compd.*, 1998, **271**, 11-18.
28. D. L. Donohue, *Anal. Chem.*, 2002, **74**, 28A-35A.
29. R. Chinni, D. A. Cremers and R. Multari, *Appl. Opt.*, 2010, **49**, C143-C152.
30. B. T. Manard, M. F. Schappert, E. M. Wylie and G. E. McMath, *Anal. Methods*, 2019, **11**, 752-759.
31. E. Minogue, D. Ehler, A. Burrell, T. McCleskey and T. Taylor, *J. ASTM Int.*, 2005, **2**, 1-10.
32. J. P. Gorce and M. Roff, *Journal of Occupational and Environmental Hygiene*, 2015, **12**, 699-707.
33. S. C. Metzger, K. T. Rogers, D. A. Bostick, E. H. McBay, B. W. Ticknor, B. T. Manard and C. R. Hexel, *Talanta*, 2019, **198**, 257-262.
34. S. Boulyga, S. Konegger-Kappel, S. Richter and L. Sangely, *J. Anal. Atom. Spectrom.*, 2015, **30**, 1469-1489.
35. S. C. Metzger, B. W. Ticknor, K. T. Rogers, D. A. Bostick, E. H. McBay and C. R. Hexel, *Anal. Chem.*, 2018, **90**, 9441-9448.
36. United States Environmental Protection Agency, *Uses of Field and Laboratory Measurements During a Radiological or Nuclear Incident National Air and Radiation Environmental Laboratory*, 2012.
37. United States Environmental Protection Agency, *Sample Collection Procedures for Radiochemical Analytes in Environmental Matrices National Homeland Security Research Center*, 2012.
38. E. D. Hoegg, C. J. Barinaga, G. J. Hager, G. L. Hart, D. W. Koppenaal and R. K. Marcus, *J. Anal. At. Spectrom.*, 2016, **31**, 2355-2362.
39. E. D. Hoegg, R. K. Marcus, D. W. Koppenaal, J. Irvahn, G. J. Hager and G. L. Hart, *Rapid. Commun. Mass. SP.*, 2017, **31**, 1534-1540.
40. E. D. Hoegg, B. T. Manard, E. M. Wylie, K. J. Mathew, C. F. Ottenfeld and R. K. Marcus, *J. Am. Soc. Mass. Spectrom.*, 2019, **30**, 278-288.
41. R. K. Marcus, B. T. Manard and C. D. Quarles, *J. Anal. At. Spectrom.*, 2017, **32**, 704-716.
42. L. X. Zhang and R. K. Marcus, *J. Anal. At. Spectrom.*, 2016, **31**, 145-151.
43. E. D. Hoegg, S. Godin, J. Szpunar, R. Lobinski, D. W. Koppenaal and R. K. Marcus, *J. Am. Soc. Mass. Spectrom.*, 2019, **30**, 1163-1168.

44. T. J. Williams and R. K. Marcus, *J. Anal. At. Spctrom.*, 2020, submitted for publication.
45. C. D. Quarles, J. Gonzalez, I. Choi, J. Ruiz, X. L. Mao, R. K. Marcus and R. E. Russo, *Spectrochim Acta B*, 2012, 76, 190-196.
46. A. J. Carado, C. D. Quarles, A. M. Duffin, C. J. Barinaga, R. E. Russo, R. K. Marcus, G. C. Eiden and D. W. Koppenaal, *J. Anal. At. Spectrom*, 2012, **27**, 385-389.
47. R. K. Marcus, H. W. Paing and L. X. Zhang, *Anal. Chem.*, 2016, **88**, 5579-5584.
48. C. Q. Burdette and R. K. Marcus, *Analyst*, 2013, **138**, 1098-1106.
49. A. J. Francis, G. Halada, J. Gillow and C. Clayton, *Mechanisms of Radionuclide-Hyroxycarboxylic Acid Interactions for Decontamination of Metallic Surfaces*, 2002.

CHAPTER V

COUPLING OF LASER ABLATION AND THE LIQUID SAMPLING – ATMOSPHERIC PRESSURE GLOW DISCHARGE PLASMA FOR COMPREHENSIVE MAPPING: ATOMIC, MOLECULAR, AND SPATIAL ANALYSIS

5.1 Abstract

Atomic and molecular species distributions are vital information for a broad number of applications such as materials development and pharmaceutical discovery. There is currently no single analytical method that can acquire atomic, molecular, and spatial information from a single sample. This paper presents the coupling and development of an NWR213 laser ablation (LA) system to the liquid sampling – atmospheric pressure glow discharge (LS-APGD) microplasma for combined atomic and molecular (CAM) analysis from laser ablated particles. The work demonstrates a fundamental balance that must be considered between the extent of fragmentation of molecules and ionization of atoms for CAM analysis. Detailed studies showed that the interelectrode gap to be a critical parameter for controlling the ionization of atomic and molecular species. Utilizing Design-of-Experiment (DoE) procedures, the discharge current was also found to be a significant parameter to control. Atomic lead, caffeine, and simultaneous lead and caffeine analysis via LA-LS-APGD-MS was made possible through improved understanding of the influence of plasma parameters on the product mass spectra of laser ablated particles. Finally, a chemical map of atomic lead and molecular caffeine, from lead nitrate and caffeine residues, was generated, demonstrating the comprehensive mapping capabilities of LA-LS-APGD-MS. It is believed that the LA-LS-APGD-MS could

be a valuable methodology for simultaneous mapping of atomic and molecular species from a variety of samples.

5.2 Introduction

The ability to obtain both physical and chemical images has progressed continuously over the past century since the discovery of x-rays in late 1800's.[1] The medical field in particular has benefited greatly from the development of imaging techniques, utilizing everything from simple x-rays to magnetic resonance imaging (MRI), to diagnose underlying medical conditions. These two methodologies illustrate a dichotomy that exists in many areas of science and technology; techniques which deliver either structural (x-rays) or chemical (MRI) information, but not both, simultaneously. Knowledge of both chemical and spatial information is becoming increasingly important as the location of specific elemental or molecular species within a sample can provide substantial insight into the function, or perhaps failure, of a system.[2]

Fields such as pharmaceutical development,[3,4] nanotechnology,[5,6] and phytoremediation[7,8] have advanced significantly from the improvements in imaging methodologies. As an example, through mapping of nanoparticles in animal models during the drug development process, the complex mechanisms of drug - cell interactions can be elucidated.[9,10] Similarly, for fields such as phytoremediation, mapping brings insights into the mechanism for toxic metal sequestrations, allowing researchers to develop improved remediation methods.[7,8] Understandably, the developments in a variety of chemical mapping/imaging techniques has provided new capabilities to obtain this type of information.[11-16]

Chemical imaging methods can be divided between two distinct categories of atomic or molecular species information. On one hand, there are elemental mapping/imaging techniques[17] such as x-ray fluorescence (XRF),[18] laser ablation (LA) – inductively coupled plasma - mass spectrometry (ICP-MS),[13] and glow discharge (GD) plasmas.[19] These techniques provide information on how certain elements are distributed across a structure. As an example, LA-ICP-MS has recently been utilized to determine the influence of Wilson's disease on distribution of copper in the liver of rats.[20] On the other end of the spectrum, the multiple molecular mapping/imaging techniques[21,22] include matrix assisted laser desorption ionization (MALDI) – MS,[23] surface enhanced Raman spectroscopy (SERS),[24] and desorption electrospray ionization (DESI) – MS.[25] Many of these techniques are utilized to understand biological functions though the mapping of proteins or their corresponding amino acids.[26] As a complement to the LA-ICP-MS example above, MALDI – MS has recently been utilized to determine the distribution of cannabinoids in aged cannabis leaves.[27] Of course the aforementioned techniques have their share of advantages and disadvantages. Typically, non-destructive techniques such as XRF and SERS tend to have higher detection limits relative to mass spectrometric techniques such as LA-ICP-MS and MALDI-MS. Non-destructive techniques, however, have the advantage that the sample structure is preserved throughout the analysis. While these powerful techniques provide either atomic or molecular information along with spatial information, they alone are not comprehensive in terms of providing simultaneous atomic, molecular, and spatial information.

Towards the goal of comprehensive chemical mapping, an assortment of either tandem or multimodal mapping/imaging techniques have been implemented.[28-31] The multimodal techniques can be categorized based on whether or not both the techniques are destructive. If one of the techniques is non-destructive, then the non-destructive technique is utilized first followed by the second technique which is employed to probe the same sample. For example, μXRF was followed by MALDI-MS to first determine the distribution of calcium, phosphorous, and sulfur , and then lipids in a chicken phalanx.[32] This type of sampling is faced with a number of challenges, the first being accurate and reproducible sample mounting and probing. In addition, the different techniques inevitably provide different pixel resolution, making spatial correlation from one technique to another difficult and leading to an overall lower resolution. In some circumstances, two destructive techniques are utilized due to the generally higher sensitivity provided by those methods in comparison to their non-destructive counterparts. In these cases, two samples from the same source are required, which poses difficulties for any samples where heterogeneity is expected between the samples. As an example, MALDI-MS has been utilized to investigate the distribution of the stromelysin-3, a gene that is expressed in human breast cancer, followed by LA-ICP-MS on a different sample to determine the elemental distribution of zinc in human breast cancer tissues.[28] Of course, there are also practical disadvantages of utilizing two different techniques such as cost of operation, instrument footprint, and resource consumption. Ideally, both atomic and molecular information would be obtained from a single sample utilizing a single probing event. Such a technique would ideally have

the potential advantages of decreasing the cost and complexity of the system while increasing the overall throughput.

Laser ablation techniques have been coupled to a handful of ionization sources for either atomic e.g. LA-ICP[33] or molecular analysis LA-ESI.[34] Key here is the fact that the laser is simply a sampling device, removing material in a spatially-selective manner for subsequent ionization as dictated by the type of desired information. This capability to sample for either atomic or molecular analysis makes it an excellent sampling mechanism for combined atomic and molecular (CAM) mapping. Laser ablation systems provide automated mapping capabilities and commercialized instruments have been on the market for decades. However, there are currently no instruments on the market that are capable of ionizing both atomic and molecular species simultaneously. For this purpose, we explore the liquid sampling – atmospheric pressure glow discharge (LS-APGD) microplasma as an ionization source for combined atomic and molecular (CAM) chemical analysis.[35-37] The previous demonstration of atomization and ionization of laser ablated particles[13,38] couples well with the CAM capabilities of the ion source. The LS-APGD also has practical traits such as low resource consumption and small footprint.[39] The development of an LA-LS-APGD-MS technique would be the first demonstration of comprehensive (atomic, molecular, and spatial) information being acquired via a single acquisition method.

Demonstrated here are studies which set the stage for the abilities for CAM imaging. The influence of LS-APGD parameters on the mass spectral features from laser ablated particles of organic and inorganic species were explored for the purpose of CAM analysis. Potential ionization/fragmentation pathways of these ablated particles were also

examined. A chemical map of atomic lead and caffeine was generated from lead and caffeine residues to demonstrate the basic CAM mapping capabilities of the LA-LS-APGD-MS. This capability to map atomic and molecular species was then tested for a complex biological matrix. It is believed that these initial demonstrations portend new problem-solving capabilities which will find application across many fields from biology to materials science.

5.3 Methods and materials

5.3.1 Instruments

The LS-APGD assembly utilized in this study is similar to previous LA iterations,[38] Fig.5.1. A Spellman high-voltage power supply (Spellman High Voltage Electronics Corporation, Hauppague, NY, USA) provides a positive potential at a fixed current to a stainless steel counter electrode (880 µm i.d., 1600 µm o.d., Restek Corporation, Bellefonte, PA, USA) that sits perpendicular to the grounded cathode (solution electrode). The solution electrode is comprised of a stainless steel outer capillary (880 µm i.d., 1600 µm o.d., Restek Corporation, Bellefonte, PA, USA) with a nested fused silica inner capillary (280 µm i.d., 580 µm o.d., Restek Corporation, Bellefonte, PA, USA). A flow of helium gas is delivered between the outer and inner capillaries using a mass flow controller (Alicat Scientific MC Series, Tucson, AZ, USA). A helium flow is also delivered to the NWR213 LA system (Elemental Scientific Lasers, Bozeman, MT, USA) with an identical mass flow controller. The electrolytic solution (2% HNO_3, v/v) is pumped though the silica inner capillary by a syringe pump (Chemyx Fusion 100, Stafford, TX, USA). For typical solution-based analysis with the LS-APGD, the solution electrode is held parallel to the

MS inlet. In the case of the LA implementation, the counter electrode is used to transport the ablated particles into the plasma, and is held in-line with the MS inlet for transportation of particles directly into the plasma, flowing toward MS entrance aperture.

A NWR213 LA system was fitted with a Two Volume 2 (TwoVol2), a 10 cm x 10 cm ablation chamber. The helium flow in to the TwoVol2 chamber, serving as the carrier gas between the ablation cell and the microplasma counter electrode, is regulated via the mass flow controller imbedded into the LA system and is set using the LA system software. Samples were ablated with a 213 nm ND:YAG laser, employing 100 µm laser spots and operating at 70% power (~ 10 J cm^{-1}) and a repetition rate of 20 Hz. During the studies of the roles of the plasma parameters, 10 laser pulses were fired for bulk metals and 1 laser pulse for residues. One shot of the laser was sufficient to ablate the entirety of the residue from the samples within the laser spot area. All optical images were acquired via a digital camera (15x-to-60x objective-to-camera magnification) that is mounted inside the NWR213 LA system.

A ThermoScientifc (San Jose, CA, USA) TSQ Quantum Access Max triple quadrupole mass spectrometer was employed for this work. The settings of the mass spectrometer were determined through the calibration and tuning of the test compound polytryosine – 1,3,6 (Fisher Scientific, Pittsburgh, PA, USA) ionized using a heated-capillary electrospray ionization (H-ESI) source. Due to the exploratory nature of this work, the mass spectrometer parent/daughter scan routines were utilized heavily to confirm the identity of various molecular species.

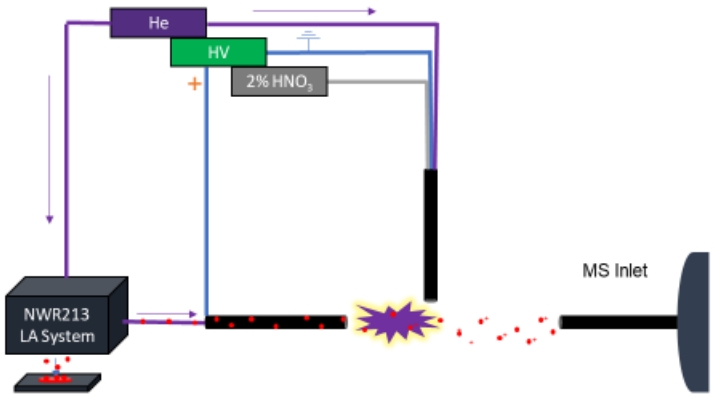

Figure 5.1 A diagrammatic representation of the LA-LS-APGD coupling during an ablation process. The LS-APGD is placed ~ 6mm away from the mass spectrometer.

5.3.2 Materials

Concentrated nitric acid (VWR, Atlanta, GA, USA) was diluted to 2% (v/v) with deionized water (DI-H_2O, 18.2 M cm^{-1}) from a water purification system (Purelab Flex, ELGA Waterlab, High Wycombe, UK). High purity bulk metal samples of lead (98% g g^{-1}) and copper (99.9 % g g^{-1}) were purchased from McMaster-Carr (Elmhurt, IL, USA). Lead was chosen due to its toxicity and high presence in the environment. Presence of lead is heavily tested and regulated by various government agencies. Similarly, copper is chosen due to its detrimental impact on solar-cell and semiconductor technologies.[40] Metal residues were prepared by dissolving the associated metal nitrate salt (VWR, Atlanta, GA, USA) in DI-H_2O. The salts were weighed on a mass balance so that the final concentration of solution was 1000 µg mL^{-1}. Afterwards approximately 1 mL was deposited onto a precleaned plain microscope slide (Fisher Scientific, Pittsburgh, PA, USA). This process was repeated until the microscope slide was mostly covered, taking care to ensure minimal overlap between droplets. The droplets were then left to dry under vacuum overnight. For

organic molecular analysis, residues of glutamic acid, caffeine, and urea were prepared from their respective solid compounds (VWR, Atlanta, GA, USA) by dissolving them in DI-H_2O. Glutamic acid is chosen due to its ubiquitous presence in most living systems.[41] Urea is an important nitrogen metabolite in plants[42] and caffeine is an easily ionizable molecule commonly analyzed by the LS-APGD as well as an influencer of pharmacokinetics of many drugs .[43] All analytes were chosen with the potential diversity of applications in mind. The compounds were weighed, dissolved, and deposited onto precleaned plain microscope slide then dried overnight in a vacuumed desiccator.

5.4 Results and discussion

5.4.1 Influence of LS-APGD parameters on atomic and molecular species' responses

Significant LS-APGD parameters were determined for atomic (metals), molecular (organic), and CAM analysis for the purpose of source optimization. A definitive screening Design of Experiments (DoE) generated by a predictive analytical software (JMP Pro, Cary, NC, USA) was used to generate the testing conditions and analyze the results. The boundaries of each of the LS-APGD operating parameters were set with the primary consideration of plasma stability and are presented in Table 5.1. Not all of the plasma operation variables were included in the DoE in order to decrease the experiment time and the computational costs. Of those parameters, two potentially significant parameters are the angle between the solution and counter electrodes as well as the plasma powering mode. Certainly, a more thorough investigation of the parameter space could provide further understanding and potentially improve the performance after this initial proof of concept. A transient spectrum was acquired via single ion monitoring mode (SIM) at m/z 208 for

lead, and m/z 195 for caffeine with a window of ± 1.5 m/z. Lead particles were ablated from bulk lead metal while caffeine was ablated from caffeine residues on a glass slide. To be clear, the bulk lead and caffeine residues are two separate samples that were tested at the same operating conditions but were not sampled simultaneously. From the results of the DOE, it was determined that electrode gap must be adjusted for the purpose of CAM analysis.

Table 5.1 High, center, and low values of microplasma operation parameters for definitive screening design utilized in DoE assessment.

Parameters	High Value	Center Value	Low Value
Current (mA)	50	38	25
Solution Flow (μL min^{-1})	50	30	10
Sheath Gas Flow (L min^{-1})	1.0	0.8	0.6
Counter Gas Flow (L min^{-1})	0.6	0.5	0.4
Electrode Gap (mm)	5	3	1

To study the influence of interelectrode gap on the analytical response, the interelectrode gap was varied from 1.4 to 5.0 mm, while other plasma parameters were kept constant at central values from Table 1. The relative intensity as a percentage of the maximum response across the range of interelectrode gaps is plotted for each analyte in Fig.5.2. The inorganic (elemental) analyte response from lead, copper, and silicon were tested from bulk materials. Lead analytes were monitored at m/z = 208, 224, and 270, each representing the most abundant isotopes of atomic lead, lead hydroxide, and lead nitrate species. Copper analytes was monitored as its atomic form and as copper nitrate, m/z = 63 and 125, respectively. The response for silicon was monitored at m/z of 60 corresponding to SiO_2. The analogous molecular species experiments were performed with residues of caffeine, glutamic acid, and urea, individually. Caffeine was monitored at its psuedomolecular ion

$M+H^+$ and the MH^+-CH_3CNO at m/z = 195 and 138, respectively. The latter is the most common fragment of the parent via most ionization methods. Glutamic acid was monitored at its common $M+H^+$ and MH^+-H_2O signatures at m/z = 148 and 130. Urea was monitored as its $M+H^+$ at m/z = 61. An average of 10 different ablated locations were used, with each location consisting of 10 laser pulses for metals and 1 for residues. The ablation locations were chosen at random across the sample surfaces while also ensuring that the sample material filled the entirety of the laser spot area. A transient spectrum was acquired via SIM at each aforementioned m/z with a ± 1.5 m/z window and the peak area of each sampling event was used as the measure of analyte response. The temporal integration period was begun when the intensity increased by 15% above the background level and was determined to have ended when the intensity fell to the same level. A spectrum was obtained per laser pulse.

As seen in Fig.5.2a, the highest response across all of the monitored inorganic analytes (and their related species) was at the largest interelectrode gap. This trend would suggest that the particles from ablated samples are fragmented more into their atomic form as the gap is increased. Simply put, the increase in gap also increases the residence time of these particles in the plasma. Which in turn increases the likelihood of fragmentation. Also as the interelectrode gap is increased, the potential across the plasma also increased (from 400 to 920 V across tested range) potentially increasing fragmentation through increased plasma energies. The error bars associated with 10 spots were left out of these plots for the sake of clarity, but generally, for all copper and lead species the RSD is ~30% around the

gap of 2 mm and ~10% for gap around 3.5 mm. For SiO_2 the RSD is ~20% throughout the gap range tested.

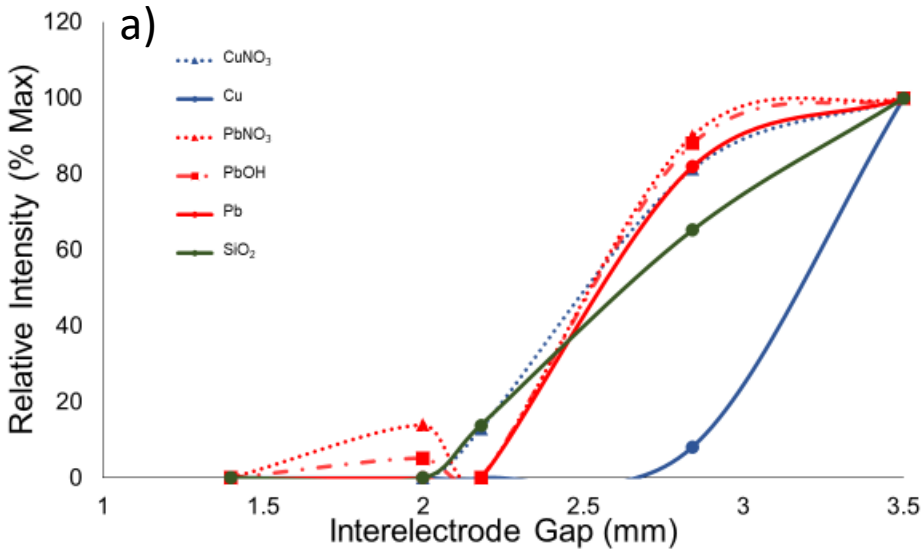

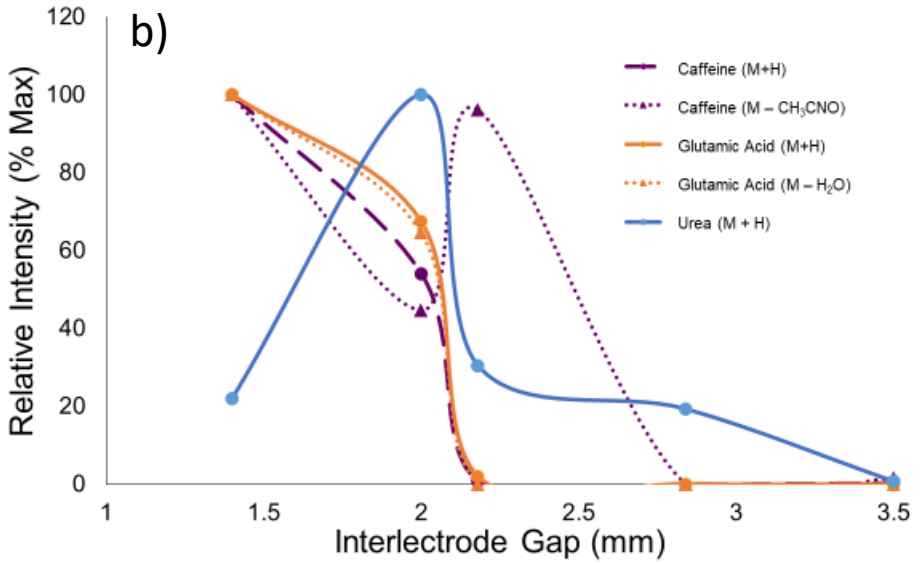

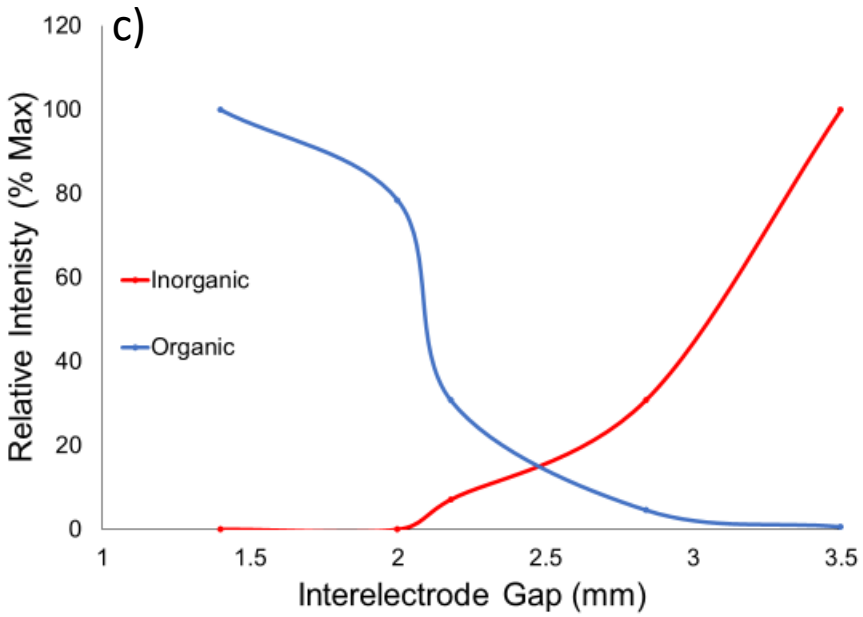

Figure 5.2 Response of relative intensity of a) inorganic analytes: $CuNO_3$ (blue color, dotted line, triangle marker), Cu (blue, solid, circle), $PbNO_3$ (red, dotted, triangle), PbOH (red, dot/solid, square), Pb(red, solid, circle), SiO_2 (green, solid, circle) and b) organic analytes: Caffeine (M+H) (purple solid, circle), Caffeine (M – CH_3CNO) (purple, dotted, triangle), Glutamic Acid (M+H) (orange, solid, circle), Glutamic acid (M-H_2O) (orange, dotted, triangle), Urea (M+H) (light blue, solid, circle) vs the change in the interelectrode gap. Demonstrating the influence of electrode gap on bulk materials and organic residues. C) Average of responses for inorganic (blue) and organic (red) vs the change in the interelectrode gap.

Figure 5.2b demonstrates that increases in the inter electrode gap corresponds to a decrease in analyte response for organic species. As mentioned previously, an increase in the electrode gap appears to cause an increase in fragmentation either from increased residence time and/or potential. This is seen as the caffeine MH^+- CH_3CNO peak is increased slightly at the middle electrode gap range. At extended electrode gaps however, the molecules fragment beyond the typically identified caffeine peaks. In the case of glutamic acid, where the common fragment ion is generally produced though thermal

dehydration,[44] the response from this fragment appears to follow the protonated molecular ion response. This indicates that longer residence times in the plasma do not increase the fragmentation to the M^+-H_2O species but that the pseudo molecular ion peak is broken into unrecognizable fragments beyond an electrode gap of 2 mm. Urea, on the other hand, had a maximum response around 2 mm in electrode gap, and the response decreased at larger electrode gaps until no response was detected at the largest electrode gap studied here. This is contrary to the results obtained for caffeine and glutamic acid where the molecular ion peaks were difficult to detect beyond 2 mm interelectrode gap. To determine if organic ionization improved overall, influence of gap on the combined intensities of MH^+ and the respective fragments (caffeine, glutamic acid) were examined. As gap increased the combined intensities decreased, indicating that ionization of caffeine and glutamic acid did not improve significantly. If the ionization efficiency did increase, it was not enough to compensate for the fragmentation of the caffeine and glutamic acid molecules into unattributable species. This stability of urea at the larger electrode gap could also be the reason the common M-NH_4^+ fragment is not detected in this work. Undoubtedly, the LS-APGD ionization/fragmentation is complex and requires extensive studies to deconvolute. Similar to Figure 2a, error bars were not shown in Figure 2b for clarity purposes. In general, the RSD of ten spots increases with increased gap for organic analysis of ~ 20 %RSD near 1.5 mm and ~ 50 %RSD near gap 2 mm. Urea, interestingly, remains between ~20 and ~30 %RSD across all gaps.

Figure 5.2c is the comparison between the average of all inorganic (red) responses and organic (blue) molecular responses as a function of increasing interelectrode gap. This

figure demonstrates the fundamental balance in the interelectrode gap that must be achieved for CAM analysis. As the electrode gap increases, fragmentation of particles/molecules increases, thus response from metal atoms increases. On the other hand, this increased fragmentation decreases the analyte response from organic molecular species due to the breakdown of the molecular structure. This would suggest that depending upon the application, the interelectrode gap can be tuned for increased atomic or molecular sensitivity and that a balance between the two can be reached for CAM analysis. Figure 5.2c shows that the crossover point between soft and hard ionization condition lies at an interelectrode gap of approximately 2.5 mm. This would be the recommended starting parameter for future studies involving new analytes. However, the interelectrode gap can be adjusted based upon individual analytes and applications.

Similar to previous work utilizing DoE, current is also found to be a significant factor in this work.[45,46] An increase in current causes higher potential across the electrodes (from 520V to 700V across DoE range), thus plays a significant role in both fragmentation and ionization. Counter intuitively, the carrier gas flow was not significant for either atomic or molecular species. This may come as a surprise due to the heavy influence of carrier gas flow on the transport of ablated particles.[47] However, the lack of significance could be due to the narrow range of values tested for the carrier gas flow. Here the range of values for the carrier gas flow are artificially limited due to the limitation of the mass spectrometer to pump down large amounts of He gas. Operating the LA-LS-APGD at lower carrier gas values than the values mentioned in the DoE range yield no analytical response from the ablated particle. Future studies on a different mass spectrometer with a larger range of

testing values for carrier gas flow may lead to the carrier gas flow appearing to be significant. Interestingly, even though interaction with the 2% nitric acid solvent is evident though the detection of lead and copper nitrate from pure bulk sample, it appears that the solution flow rate does not have any significant effect on analytical response. Certainly, a change in solvent identity may lead to a better understanding of the system and future studies with more complex parameters are warranted. The current understanding of the influence of both electrode gap and various other parameters allowed us to intelligently chose parameters for the best analytical performance by tuning the electrode gap then tuning the current.

5.4.2 Individual atomic, molecular and CAM analysis

To fully demonstrate the suitability of LA-LS-APGD for comprehensive analysis, atomic, molecular, and CAM samples were tested individually at the plasma conditions provided in Table 5.2. A small section ~ 5 mm x 5 mm square piece of bulk lead sheet (98% g g^{-1}) was ablated and a mass spectrum from 200 – 300 m/z was acquired for elemental analysis. An averaged spectrum of 10 ablated locations is shown in Fig.5.3a. A quick examination shows that the majority of the peaks detected were not atomic lead but adduct forms of lead. All of the adducts that were detected can be broken down into the respective isotope of the lead atomic peak via MS/MS experiments or applying in-source collision induced dissociation (CID). The primary adduct is the singly hydrated lead nitrate. While it is not surprising to see water adducts since the LS-APGD is primarily a water plasma, it may be surprising that the primary detected species are the nitrates. Initial examination of the detected species shows a spectrum that is quite different than previous

LA-LS-APGD work,[38] which mainly showed a maximum response from the atomic lead isotopes, followed by a minor (70%) lead hydroxide peaks. However, there are major differences between the current and previous work including the laser pulse width, plasma parameters, and the fact that CID was applied in the case of the previous work. While applying CID promotes the fragmentation of the nitrate adducts into the atomic peaks and is well understood,[48] it was not utilized here, as the primary interest of this work is to characterize the actual species formed without influence from the mass spectrometer. Two possible mechanisms are proposed, primary dissolution (R1-R3) or vaporization (R4-R6), for why the nitrate species are detected when the lead sheet is ablated. First, metallic lead readily dissolves in nitric acid though the following reactions:

$$Pb_{Particles} + HNO_{3_{(g,l)}} + H_2O_{(g,l)} \rightarrow (Pb^{2+} + 2(NO_3)^- + H_2O)_{(l)} \quad \text{(R1)}$$

$$(Pb^{2+} + 2(NO_3)^- + H_2O)_{(l)} \rightarrow Pb(NO_3)_{2_{(g)}} \quad \text{(R2)}$$

$$Pb(NO_3)_{2_{(g)}} \rightarrow Pb(NO_3)^+ \quad \text{(R3)}$$

It can be proposed that the particles are dissolved in a liquid-gas mixture, (R1). Afterwards the mixture desolvate, and lead nitrate gas is formed (R2). The resulting lead nitrate is then ionized to $Pb(NO_3)^+$ by the plasma (R3) and then detected by the mass spectrometer. The ionization process provided here closely mimicked those described by Zhang *et al.* utilizing the LS-APGD.[49] Second, the plasma itself might also cause the atomization of lead from the bulk lead. While this work and previous works have demonstrated that the LS-APGD is energetic enough to vaporize nanosecond laser ablated particles, it may also be possible to atomize and ionize the particles as well through a combination of thermal and electron influences. If this is the case, the following reactions could occur:

$$Pb_{particle} \rightarrow Pb^{0}{}_{(g)} \quad \text{(R4)}$$

$$Pb^{0}{}_{(g)} \rightarrow Pb^{+} \quad \text{(R5)}$$

$$Pb^{+} + NO_3^{\cdot} \rightarrow PbNO_3{}^{+} \quad \text{(R6)}$$

The lead particle is vaporized and atomized by the plasma (R3). Afterwards the neutral atom is ionized (R4) into Pb^+ by the plasma's thermal and electron energies. The resulting Pb^+ then interacts with radical NO_3 in the plasma to form $PbNO_3^+$ (R6), which is then detected by the mass spectrometer. Certainly, both the proposed mechanisms appear to be possible and a component of future works will focus upon deconvoluting the exact mechanism of lead nitrate formation by the plasma.

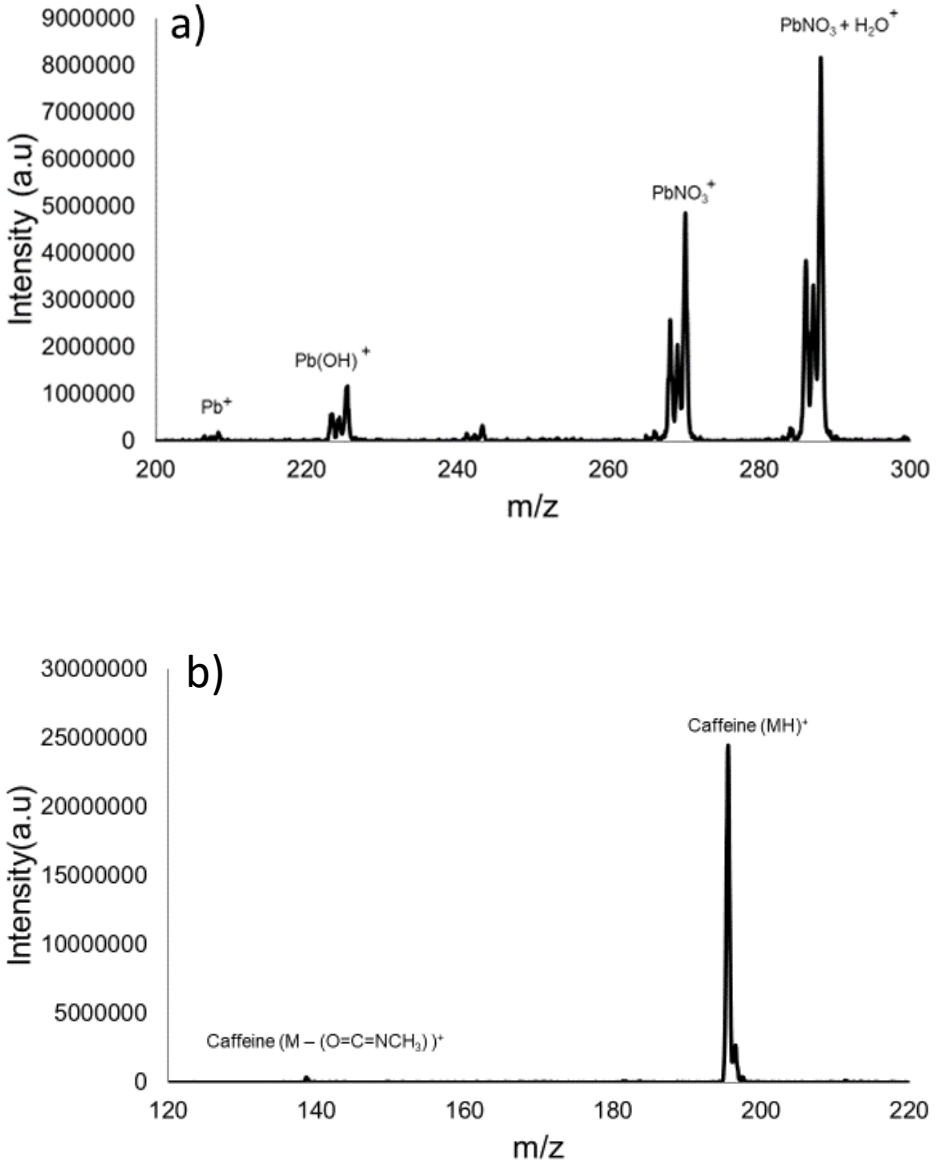

Figure 5.3 An averaged mass spectrum of 10 laser ablated spots on ablated a) lead metal sheet, and b) caffeine residue. Lead mass spectrum demonstrates a strong interaction with the 2% nitric acid solvent while molecular residue shows typical ESI like mass spectrum.

For organic molecular analysis, a 1000 µg mL^{-1} caffeine residue is ablated and the mass spectrum from 120 – 220 m/z is collected. An averaged spectrum of 10 ablated location is shown in Fig.5.3b. By far the most prominent peak is the protonated caffeine

peak that is also typically found in electrospray mass spectrometry. The neutral loss of methyl isocyanate ($O{=}C{=}NCH_3$) from protonated caffeine is seen at m/z 138. The observed protonated caffeine species are generated though the following reaction:

$$M + H_3O^+ \rightarrow MH^+ + H_2O \quad \text{(R7)}$$

Where M represents the neutral caffeine molecules entering the plasma. The protonated species are not surprising as the proton transfer from H_3O^+ (from LS-APGD electrolytic solution) to a neutral caffeine molecule is thermodynamically favored.[50] The major product ion at m/z 138 is generally due to rDA from the protonated caffeine as commonly seen in ESI.[51] This ,for the first time, demonstrates the capability of the LS-APGD for ionization of molecular and atomic species without the need to convert the solvent system.

Table 5.2. DoE-determined LS-APGD microplasma conditions utilized for atomic, molecular, and CAM analysis.

Parameter	Atomic	Molecular	CAM
Current (mA)	50	30	35
Solution Flow (μL min^{-1})	10	10	10
Sheath Gas Flow (L min^{-1})	0.6	0.6	0.6
Counter Gas Flow (L min^{-1})	0.6	0.6	0.6
Electrode Gap (mm)	4	1	2

To determine the suitability of the LA-LS-APGD for simultaneous CAM analysis, a residue was prepared by combining a 50/50 (v/v) solution of 1000 μg mL^{-1} of lead nitrate and caffeine, resulting in a solution that is 500 μg mL^{-1} of lead and 500 μg mL^{-1} of caffeine. The solution was then deposited onto a silica glass slide and allowed to dry at room temperature in a vacuum desiccator. Afterwards the dried residue was ablated using the NWR213 LA system. Figure 5.4 shows the mass spectrum from a single laser pulse, ablating the 50/50 lead and caffeine residue. As a proof-of-concept, a single mass spectrum

from a single laser pulse is utilized to eliminate possibilities that caffeine and lead may appear in different mass spectra or different shots from the laser. Because of the change in mass spec conditions, it is not a surprise that the analyte intensity is lower this spectrum compared to those from Figure 5.3. The species seen, however, remain the same even when utilizing lead residue instead of bulk lead. This is, to our knowledge, the first demonstration of simultaneous ionization and detection of atomic and molecular analytes.

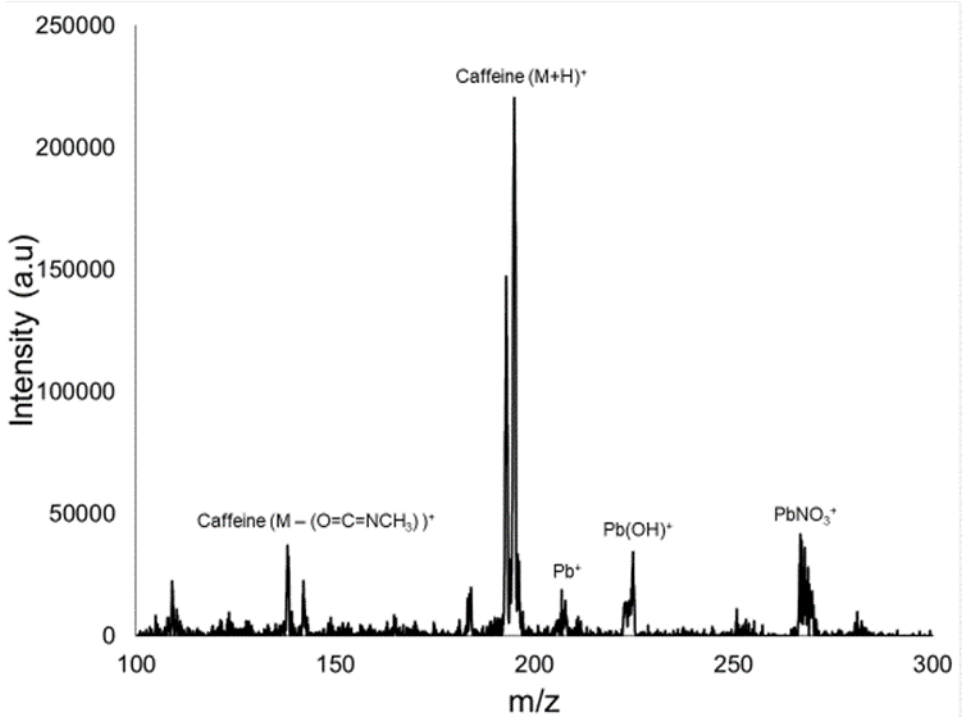

Figure 5.4 A mass spectrum of a single shot on a single spot of 500 μg L^{-1} lead: caffeine (50:50)(v:v) residue, demonstrating simultaneous CAM ionization and detecting capabilities.

5.4.3 Spatial determination of atomic and molecular species

Various LA-MS systems have demonstrated the capability of spatial determination by effectively converting the time of the mass spectrometer scans to position by correlating laser repetition rate, stage speed, and spot size. While LA systems have been shown to be capable of spatial determination, neither the TSQ nor the LS-APGD have been

demonstrated to be capable of spatial information collection. The questions remain of whether the TSQ can resolve time finely and accurately enough to be capable of temporally resolving individual particle clouds from LA; a required concept for LA mapping. Likewise, similar questions must be asked of the LS-APGD, whether the transit time in the plasma is fast enough to temporally resolve individual packets of particles. Previous LA work on the LS-APGD has indicated a residence time on the order of 5 – 30 ms in the plasma, which would make mapping difficult if the particles were to be retarded after introduction into the plasma.[45] To test the mapping capability of this coupling to acquire spatial information, two residues, one containing lead and one containing caffeine at 1000 μg mL^{-1}, were placed on a glass slide roughly separated at the center by approximately 5 mm. Next, the laser was fired across the top of the two residues at 400 μm s^{-1} stage speed and a 100 μm laser spot size. The transient spectrum of m/z 195 and m/z 208 for caffeine and lead peaks, respectively was monitored in SIM mode with a 3 m/z window. The total scan time/duty cycle was set to 25 ms. These laser parameters were chosen empirically by testing various single residues and determined based on signal intensity, experimental time, and ion cloud diffusion. The acquired transient is shown in Fig. 5.5. The transients provided are total ion count (purple), counts at m/z 208 (red) and m/z 195 (blue). Two key points are demonstrated in this figure. First, the increase in response from m/z 208 and m/z 195 were temporarily separated. As we are capable of discerning the lead and caffeine residue temporarily, we can discern the two residues spatially. Second, this figure also shows that no response in m/z 208 was seen when the laser is scanning across the caffeine residue and

vice-versa for the case of lead, such that we were able to obtain spatial and CAM information.

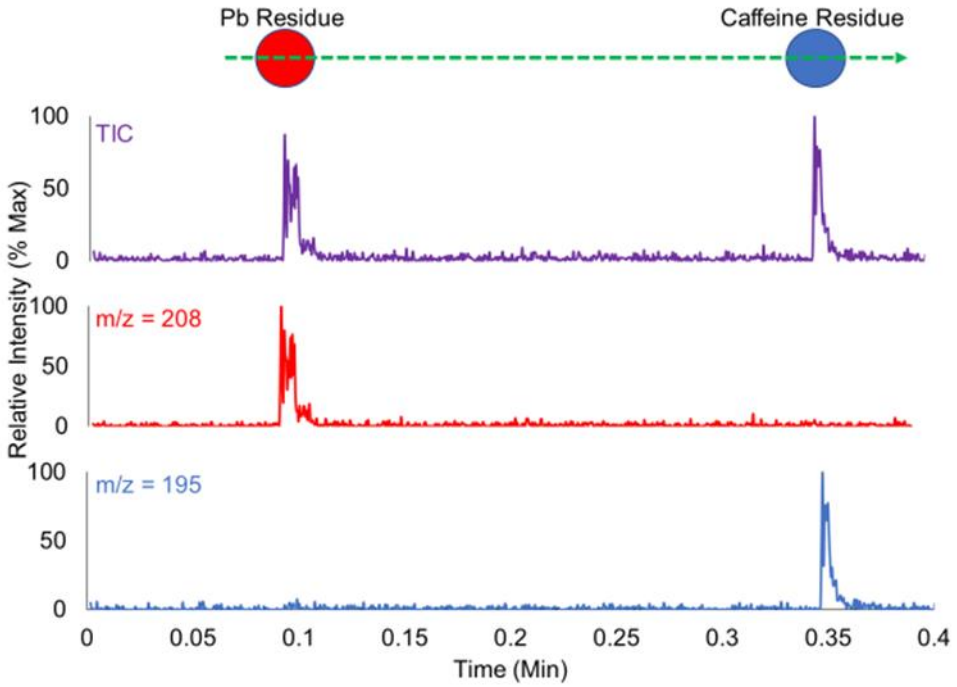

Figure 5.5 A transient of total ion scan (purple) and single ion monitoring at m/z 208 (red) and m/z 195 (blue) as laser is scanned across adjacent 1000 μg mL^{-1} lead and 1000 μg mL^{-1} caffeine residues at 400 μm s^{-1}. The red and blue circles are diagrammatic representation of the residues while the green arrow represents the laser ablation direction.

5.4.4 Evaluation of comprehensive mapping

To map atomic and molecular species, residues were prepared by utilizing either 1000 μg mL^{-1} solution of lead or caffeine to draw out distinct letters onto a standard microscope glass slide. The lead solution was used to draw out the letter "C" and the caffeine solution was used to draw out the letter "U" with a pipette. Along with the two letters, two residue dots containing a 50/50 (v/v) solution of caffeine and lead were also placed on the left side of the letters. The microscope slide is than left to dry in a vacuum desiccator overnight. The stitched microscope image of the dried residues, shown in

Fig.5.6a, was acquired via the NWR213 optical camera. The laser and MS conditions were the same from the previous section. The laser spot size is set to 100 μm, the laser power at ~10 J cm^{-2} fluence, and stage speed set to 400 μm s^{-1}. The MS scanned between m/z 195 and 208±1.5 in 25 ms. The image was analyzed using parallel laser raster lines that totaled an area of 10 cm^2 and utilized a 100 μm spacing between lines. The transient file acquired via MS was converted to an image utilizing an open source software developed by Robin Schmid from University of Münster. Most of the settings were left in default outside of the split point, which was adjusted for proper image formation, and background intensity was set to approximately 60% for better contrast between signal and background. The map formed from m/z 208 is shown in Fig.6b and the map formed from m/z 195 is shown in Figure 6c. As expected, the map of m/z 208 appears similar to letter "C", while the map of m/z 195 appears similar to the letter "U". Small details that arise during the drying process of the residue is also seen in Fig.6a, such as the small protrusion on the left side of the "C" , dashed red circle 1, and the right side of the "U", dashed red circle 2. Corresponding spatial features in the chemical maps, Fig.6 b-c, are marked with dashed white circles. The inclusion of these small features in the chemical maps indicates a strong spatial fidelity to the original residue. However, there are two points that must be addressed. First, it appears as though the maps are both slightly shifted and elongated. There could be multiple causes for this, but one of the most likely causes is the uncertainty in the time domain of the mass spectrometer. While the duty circle of the mass spectrometer can be set, the dwell time at individual masses were not controllable via the provided software. Second, when examining the m/z 195 map, one could notice a faint map of the letter "C". Ideally, it should

not respond in that region since caffeine was not deposited in that area. The primary cause of this is believed to be in the nature of caffeine not escaping the system entirely due to required low gas flow rates of the mass spectrometer. By pulsing gas through to the plasma, we discover that caffeine was adsorbed to various sections of tubing. Thus, the appearance of the "C" in m/z 195 could be the lead particles knocking off some of the caffeine that may have attached to the tubing of the experimental setup. Even with these considerations, we find the capability of mapping both molecular and atomic species simultaneously both novel and promising. Tremendous improvement in terms of map quality could be envisioned by coupling the LA-LS-APGD to a MS dedicated to mapping and with improved helium gas pumping capability.

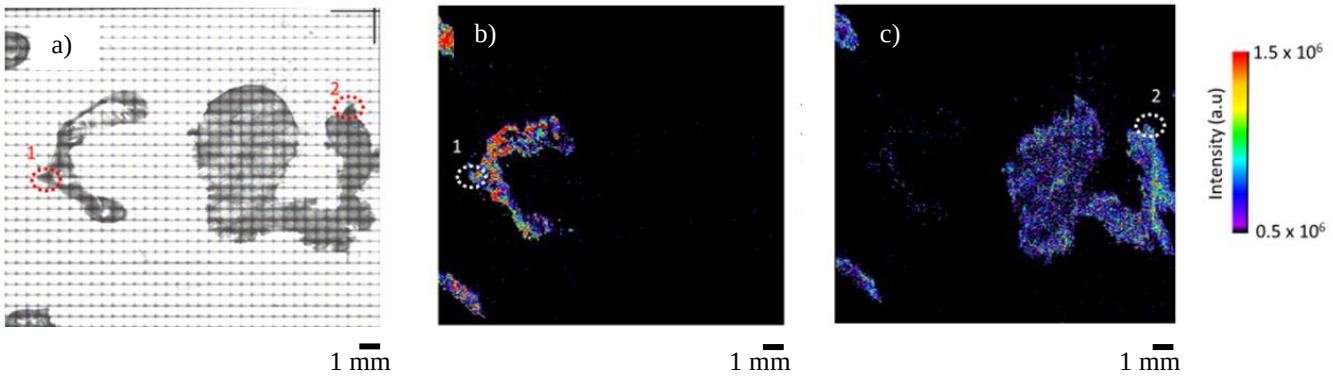

Figure 5.6. a) Stitched NWR213 optical image of dried "CU" residue written where "C" is written with 1000 µg mL^{-1} lead solution and "U" is written with 1000 µg mL^{-1} caffeine solution. The two dots on the left are 50/50 (v/v) mixture of lead and caffeine solution. Maps with SIM at b) m/z 208 and c) m/z 195 are presented. Maps were generated from transient spectra utilizing software from University of Münster. The SIM map at m/z 208 shows a distinct "C" shape while the SIM map at m/z 195 shows a "U" shape and the two dots on the left appears on both SIM maps. Distinct spatial features are marked with a) dotted red circle b-c) dotted white circle.

To further demonstrate the mapping capability of the LA-LS-APGD, a 20 µm thick cryosection of a chicken breast on a clean microscope slide with a thallium residue deposited onto the section is mapped. The stitched NWR optical image of

the chicken breast section is shown in Figure 7a. Noticeable in the figure is the tear in the center of the tissue that occurred during the cryosectioning process. A small discernable spatial feature, as indicated by a dashed red circle, appeared near the upper right corner of the previously mentioned tear in the center. Glutamic acid is monitored here at m/z 148 corresponding to the M+H peak. It is believed that glutamic acid is abundantly distributed throughout the chicken breast meat.[52] A 500 µg mL^{-1} solution of thallium is deposited near the center of the chicken section to mimic potential metal contaminate. Thallium is monitored at 205 m/z corresponding to the elemental atomic mass. The microscope slide is than left to dry in a vacuum desiccator overnight. The laser, MS, and imaging software parameters were the kept the same as described in the mapping of residue. The map of m/z 205, Figure 7b, shows a localized dried solution of thallium. Noticeably, the residue dried in a ring like fashion, in which the outer perimeter of the residue has a higher density of thallium compared to center of the residue. Also, it appeared as though the droplet did not coat over the chicken section, instead filling into the cut, this is especially noted by the similar spatial feature, dashed white circle, as seen in Figure 7a. The map formed at m/z 148, Figure 7c, showed glutamic acid to be distributed evenly throughout the chicken beast slice outside of the tear at the center of the tissue slice. This is to be expected as glutamic acid is one of the most representative amino acids in chicken breast meat.[52] The strong fidelity of the chemical maps that of the optical image of the chicken breast

demonstrates the potential of the LA-LS-APGD for comprehensive mapping of biological samples.

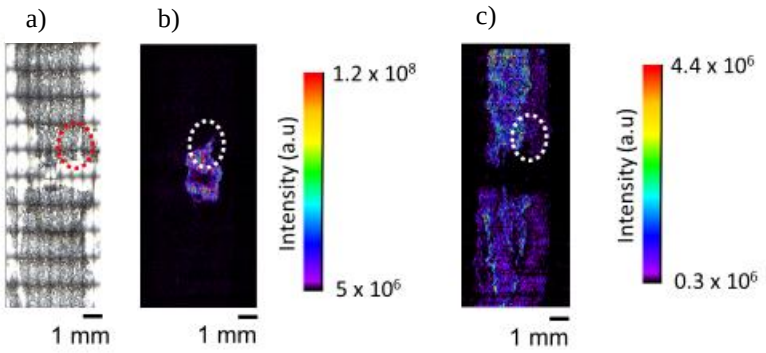

Figure 5.7. a) Stitched NWR213 optical image of a cryosection chicken breast marked with 500 ug L^{-1} thallium solution. Maps with SIM at b) m/z 205 and c) m/z 148. Maps were generated from transient spectra utilizing software from University of Münster. Distinct spatial featured is marked with a) a dotted red circle b-c) dotted white circle.

5.5 Conclusion

For the first time, we have demonstrated a comprehensive imaging technique that can acquire spatial, atomic, and molecular information simultaneously. This technique completely eliminates the need for multimodal techniques that requires the utilization of multiple instruments making pixel to pixel correlation difficult. These multimodal techniques often require multiple samples. By simply tuning the interelectrode gap and current of the LS-APGD, one could utilize this small footprint, inexpensive ionization source for the desired atomic and molecular analysis. The source can easily be tuned for either atomic, molecular, or simultaneous CAM analysis. This tunability can allow the LS-APGD to be used for multiple applications whether it is for trace atomic or molecular analysis. Finally, we were able to map residues and biological samples with reasonable

fidelity, demonstrating for the first time in literature, simultaneous atomic and molecular mapping.

After this initial demonstration, there are multiple paths forward in terms of research goals. Improvements for sensitivity and improved plasma understanding can be accomplished though coupling more parameters to DoE as well as varying analytes. By utilizing different solvents, further insight into the mechanism of fragmentation and ionization. One path of improvement could be the coupling of LA-LS-APGD to a mass spectrometer dedicated for mapping. Also, by utilizing a mass spectrometer with improved gas pumping capabilities, a better understanding of the influence of carrier gas flow may be achieved. This technique could also be applied to various real-world samples such as medical implants where both the implant itself and the surrounding biological molecules are mapped.

5.6 Acknowledgement

We would like to thank Ciaran O'Connor from Elemental Scientific Laser, LLC for lending the NWR213 LA system as well as instrument support throughout the experiments. We would also like to gratefully acknowledge Anthony R. Scavuzzo from Princeton University for scientific discussion on potential mechanism of molecular dissociation within the LS-APGD and Chad McMahan from Clemson University bioengineering department for support with cryosectioning of chicken breasts.

5.7 References

1. K. Sansare, V. Khanna and F. Karjodkar, *Dentomaxillofac. Rad.*, 2011, **40**, 123-125.
2. C. Petibois, *Anal. Bioanal. Chem.*, 2010, **397**, 2051-2065.
3. C. M. Hartshorn, Y. J. Lee, C. H. Camp, Z. Liu, J. Heddleston, N. Canfield, T. A. Rhodes, A. R. H. Walker, P. J. Marsac and M. T. Cicerone, *Anal. Chem.*, 2013, 85, 8102-8111.
4. H. Y. Xie, Q. C. He, Y. F. Zhao, H. J. Li, M. Zhao, X. F. Chen, Z. W. Cai, K. Z. Fang and H. X. Song, *Rapid. Commun. Mass. Sp.*, 2020, **34**.
5. J. T. S. Lum and K. S. Y. Leung, *J. Anal. Atom. Spectrom.*, 2017, **32**, 2127-2139.
6. J. Lim, S. H. Kim, R. A. Armengol, O. Kasian, P. P. Choi, L. T. Stephenson, B. Gault and C. Scheu, *Angew. Chem. Int. Edit.*, 2020, **59**, 5651-5655.
7. C. Do, F. Abubakari, A. C. Remigio, G. K. Brown, L. W. Casey, V. Burtet-Sarramegna, V. Gei, P. D. Erskine and A. van der Ent, *Chemoecology*, 2020, **30**, 1-13.
8. J. Kaiser, M. Galiova, K. Novotny, R. Cervenka, L. Reale, J. Novotny, M. Liska, O. Samek, V. Kanicky, A. Hrdlicka, K. Stejskal, V. Adam and R. Kizek, *Spectrochim. Acta B*, 2009, **64**, 67-73.
9. J. Yan, C. Y. Hu, P. Wang, B. Zhao, X. Y. Ouyang, J. Zhou, R. Liu, D. N. He, C. H. Fan and S. P. Song, *Angew. Chem. Int. Edit.*, 2015, **54**, 2431-2435.
10. A. S. Jeevarathinam, J. E. Lemaster, F. Chen, E. Zhao and J. V. Jokerst, *Angew. Chem. Int. Edit.*, 2020, DOI: 10.1002/anie.201914120.
11. J. Santner, M. Larsen, A. Kreuzeder and R. N. Glud, *Anal. Chim. Acta.*, 2015, **878**, 9-42.
12. T. Schmid, L. Opilik, C. Blum and R. Zenobi, *Angew. Chem. Int. Edit.*, 2013, **52**, 5940-5954.
13. M. Bonta, J. J. Gonzalez, C. D. Quarles, R. E. Russo, B. Hegedus and A. Limbeck, *J. Anal. Atom. Spectrom.*, 2016, **31**, 252-258.
14. P. Konarski, M. Misnik and A. Zawada, *J. Anal. Atom. Spectrom.*, 2016, **31**, 2192-2197.
15. B. Fernandez, *Anal. Bioanal. Chem.*, 2019, **411**, 547-548.
16. W. J. Perry, A. Weiss, R. Van de Plas, J. M. Spraggins, R. M. Caprioli and E. P. Skaar, *Curr. Opin. Chem. Biol.*, 2020, **55**, 127-135.
17. J. Pisonero, N. Bordel and V. S. Smentkowski, *J. Anal. At. Spectrom.*, 2013, **28**, 970-972.
18. M. Alfeld, M. Mulliez, P. Martinez, K. Cain, P. Jockey and P. Walter, *Anal. Chem.*, 2017, **89**, 1493-1500.
19. M. R. Webb, V. Hoffmann and G. M. Hieftje, *Spectrochim. Acta B*, 2006, **61**, 1279-1284.
20. J. C. Muller, J. Lichtmannegger, H. Zischka, M. Sperling and U. Karst, *J. Trace. Elem. Med. Bio.*, 2018, **49**, 119-127.
21. W. Du, Y. Wang, Q. M. Luo and B. F. Liu, *Anal. Bioanal. Chem.*, 2006, **386**, 444-457.

22. J. S. Fletcher and J. C. Vickerman, *Anal. Bioanal. Chem.*, 2010, **396**, 85-104.
23. K. Schwamborn, M. Kriegsmann and W. Weichert, *Bba-Proteins Proteom.*, 2017, **1865**, 776-783.
24. P. X. Wang, S. Pang, J. H. Chen, L. McLandsborough, S. R. Nugen, M. T. Fan and L. L. He, *Analyst*, 2016, **141**, 1356-1362.
25. J. P. Rodrigues, S. S. Prova, L. A. B. Moraes and D. R. Ifa, *Anal. Bioanal. Chem.*, 2018, **410**, 7135-7144.
26. K. Tanaka, S. Takenaka, S. Tsuyama and Y. Wada, *J. Am. Soc. Mass. Spectr.*, 2006, **17**, 508-513.
27. N. A. dos Santos, L. M. de Souza, F. E. Pinto, C. D. Macrino, C. M. de Almeida, B. B. Merlo, P. R. Filgueiras, R. S. Ortiz, R. Mohana-Borges and W. Romao, *Anal. Methods-Uk*, 2019, **11**, 1757-1764.
28. R. G. de Vega, M. L. F. Sanchez, N. Eiro, F. J. Vizoso, M. Sperling, U. Karst and A. S. Medel, *Anal. Bioanal. Chem.*, 2018, **410**, 913-922.
29. L. Matjacic, V. Palitsin, G. W. Grime, N. Abdul-Karim and R. P. Webb, *Nucl Instrum Meth B*, 2019, **450**, 353-356.
30. S. Trog, A. H. El-Khatib, S. Beck, M. R. Makowski, N. Jakubowski and M. W. Linscheid, *Anal. Bioanal. Chem.*, 2019, **411**, 629-637.
31. A. Retzmann, M. Blanz, A. Zitek, J. Irrgeher, J. Feldmann, M. Teschler-Nicola and T. Prohaska, *Anal. Bioanal. Chem.*, 2019, **411**, 565-580.
32. A. Svirkova, A. Turyanskaya, L. Perneczky, C. Streli and M. Marchetti-Deschmann, *Analyst*, 2018, **143**, 2587-2595.
33. K. Halbach, S. Wagner, S. Scholz, T. Luckenbach and T. Reemtsma, *Anal. Bioanal. Chem.*, 2019, **411**, 617-627.
34. J. K. Roman, C. M. Walsh, J. Oh, C. E. Dana, S. Hong, K. D. Jo, M. Alleyne, N. Miljkovic and D. M. Cropek, *Anal. Bioanal. Chem.*, 2018, **410**, 1911-1921.
35. L. X. Zhang and R. K. Marcus, *J. Anal. At. Spectrom.*, 2016, **31**, 145-151.
36. T. J. Williams and R. K. Marcus, *J. Anal. At. Spectrom.*, 2019, **34**, 1468-1477.
37. E. D. Hoegg, S. Godin, J. Szpunar, R. Lobinski, D. W. Koppenaal and R. K. Marcus, *J. Am. Soc. Mass Spectrom.*, 2019, **30**, 1163-1168.
38. A. J. Carado, C. D. Quarles, A. M. Duffin, C. J. Barinaga, R. E. Russo, R. K. Marcus, G. C. Eiden and D. W. Koppenaal, *J. Anal. At. Spectrom.*, 2012, **27**, 385-389.
39. R. K. Marcus, B. T. Manard and C. D. Quarles, *J. Anal. At. Spectrom.*, 2017, **32**, 704-716.
40. T. Buonassisi, M. A. Marcus, A. A. Istratov, M. Heuer, T. F. Ciszek, B. Lai, Z. H. Cai and E. R. Weber, *J. Appl. Phys.*, 2005, **97**.
41. S. Garattini, *J. Nutr.*, 2000, **130**, 901s-909s.
42. C. P. Witte, *Plant Sci.*, 2011, **180**, 431-438.
43. J. A. Carrillo and J. Benitez, *Clin. Pharmacokinet.*, 2000, **39**, 127-153.
44. I. M. Weiss, C. Muth, R. Drumm and H. O. K. Kirchner, *Bmc. Biophys.*, 2018, **11**.
45. B. T. Manard, S. Konegger-Kappel, J. J. Gonzalez, J. Chirinos, M. R. Dong, X. L. Mao, R. K. Marcus and R. E. Russo, *Appl. Spectrosc.*, 2015, **69**, 58-66.
46. K. A. Hall and R. K. Marcus, *J Anal Atom Spectrom*, 2019, **34**, 2428-2439.

47. Z. K. Wang, B. Hattendorf and D. Gunther, *J. Am. Soc. Mass. Spectr.*, 2006, **17**, 641-651.
48. T. J. Williams and R. K. Marcus, *J. Anal. At. Spectrom.*, 2019, **34**, 1468-1477.
49. L. X. Zhang, B. T. Manard, S. K. Kappel and R. K. Marcus, *Anal. Bioanal. Chem.*, 2014, **406**, 7497-7509.
50. H. Bahrami, M. Tabrizchi and H. Farrokhpour, *Chem. Phys.*, 2013, **415**, 222-227.
51. D. P. Demarque, A. E. M. Crotti, R. Vessecchi, J. L. C. Lopes and N. P. Lopes, *Nat. Prod. Rep.*, 2016, **33**, 432-455.
52. A. D. Zotte, R. Ricci, M. Cullere, L. Serva, S. Tenti and G. Marchesini, *Poultry Sci.*, 2020, **99**, 1797-1803.

CHAPTER VI

SHEATING OF LIQUID SAMPING – ATMOSPHERIC PRESSURE GLOW DISCHARGE MICROPLSMA FROM AMBIENT ATMOSPHERE AND ITS IMPLICATIONS FOR OPTICAL EMISSION SPECTROSCOPY

6.1 Abstract

The use of a borosilicate glass cylinder to sheath the operational area of the liquid sampling-atmospheric glow discharge (LS-APGD) microplasma from ambient atmosphere and its effects on optical emission spectroscopy (OES) is described. A positive influence of the glass sheath on analyte and background emission characteristics is realized, along with minor drawbacks in terms of analytical performance (i.e., repeatability) and physical restraint. Sheathing the plasma significantly reduces the ambient atmosphere background spectral contributions, especially those of nitrogen species, resulting in improved measurements of interfered Pb (I) and Ag (I) transitions. Qualitatively, the background reduction by means of glass sheathing is comparable to that of a post-acquisition, mathematical back-ground subtraction method. In addition, the noise associated with atmospheric background species is reduced as well, unlike what is observed in the post-acquisition background correction. Limits of detection (LOD) improvements for silver, lead, and cadmium are observed, while those of sodium and lithium were compromised. By virtue of the alleviation of N_2 emission from the background, the LOD of lead improved by multiple orders of magnitude after sheathing the plasma. Future development will be focused toward both improving the analytical performance of the LS-APGD-OES and better understanding the mechanism of the improvements seen by sheathing the plasma.

6.2 Introduction

For the past 40 years, the field of atomic spectroscopy has been dominated by inductively coupled plasma optical emission spectroscopy and mass spectrometry (ICP-OES/MS).[1,2] There have been great improvements over the last two decades to their use due to developments in terms of spectrometers/detectors and the implementation of separation techniques. However, there has been little change in terms of the design or operation of the excitation/ionization source itself. One particular challenge that is increasing in importance are analyses that require in-field assays/response due to either time constraints or potential hazards related to transporting samples back to the laboratory. To that end, even with the advances in ICP instrument de-sign, the size and operational overhead associated with the plasmas has not decreased over this time. As such, transportation of these instruments to remote locations is unfavorable and often infeasible. For this reason, miniaturized instruments (e.g., capable of transport in a suit-case) that would be ideal for either remote sites or for the on-line probing of process-related samples are of continuing interest.[3,4] In such cases, OES systems are more readily implemented than MS plat-forms, as the instrumental complexity of an optical spectrometer is significantly lower than that of a mass spectrometer.

Atmospheric pressure glow discharge (APGD) plasmas[4] have been of interest in this arena due to their small size, ability to operate without a vacuum, and low overall operational overhead/complexity. The basic design of these plasmas is based on the original concept of the electrolyte cathode atmospheric glow discharge plasma (ELCAD) developed by Cserfalvi *et al*.[5] Further innovation regarding these excitation sources has

shown promising results, that are described in various reviews.[4,6] One variation of the basic design is the solution cathode glow discharge (SCGD) developed by Hieftje et al., that is noted for its relatively small size and low injection-to-injection variability (1–2% RSD).[7] The extension of the use of the SCGD as an ionization source has been described recently.[8] While both of these designs (ELCAD and SCGD) have operational aspects that bode well for in-field deployment, their high solution feed rates (generally >2 mL min^{-1}) and correspondingly high volumes of waste, limit those applications.

Another promising APGD is the liquid sampling-atmospheric pressure glow discharge (LS-APGD) microplasma developed by Marcus and co-workers.[9-11] There are various unique characteristics of the LS-APGD plasma source, one of which is the lack of liquid waste, stemming from its low solution flow rates (<100 μL min^{-1}) combined with the relatively high-power density (>10 W mm^{-3}) of the small plasma volume (~ 1 mm^3).[12] The LS-APGD apparatus comprises a small footprint (<250 mm × 250 mm platform), making it very well suited for field deployment. The LS-APGD also requires significantly less power (<50 W) and support gas flow (<1 L min^{-1}) than other commercial excitation sources such as the ICP, aiding portability. Another important advantage of the LS-APGD is its versatility.[12] The LS-APGD has been demonstrated to readily pair with OES[10] and MS[10] with samples introduced in a liquid flow, via an ambient desorption (AD) process ,[13-14] and particulates generated via laser ablation processes.[15,16] As is often the case with analytical instruments developed for portability, sacrifices are made relative to laboratory-scale instruments; i.e., the limits of detection (LOD) of the LS-APGD-OES are higher than commercial ICP-OES systems. Another potential limitation for field implementation of the

LS-APGD is that, unlike the other ELCAD or SCGDs, it requires the use of helium gas (<1 L min^{-1}) for sheathing/cooling purposes.[17]

It has been demonstrated in multiple cases that the environment in which any plasma is sustained can have a tremendous influence on the properties of said plasma [18,19]. Such effects have been exploited in a positive manner, almost routinely, in laser induced breakdown spectroscopy (LIBS) for affecting increased electron densities in the plasma to determine difficult elements such as fluorine and chlorine.[20-22] For example, Kompistsas et al. demonstrated that controlling the inert gas environment shows appreciable improvements for fluorine and chlorine signal recoveries.[23] In most cases, it has been demonstrated that addition of either Ar or He improved the analytical response of all analytes. In the case of microwave-assisted (MA) - LIBS, the use of a He atmosphere provided an order of magnitude improvement in the LOD for Ca.[24]

To this point, there has been relatively little presented in terms of modifying the atmosphere for ELCAD-type sources with the exception of a publication by Piepmeier et al. demonstrating that neither He nor Ar gas atmosphere had an significant effect on the emission response of the ELCAD plasma.[25] They attributed this effect to the saturation above the cathode surface with water vapors; i.e., the plasma volume is predominately H_2O. That said, incursion of ambient atmosphere gases (N_2, O_2, etc.) into the excitation volume would certainly act to com-plicate the spectral structure. Those species might also affect the ex-citation conditions experienced by analyte species. Another attempt at controlling the atmospheric composition around a liquid-sustained plasma was made by Manz et al. on a micro-fluidic chip by over pressuring with argon into the source.[26] However, nitrogen

bands were still prominent in the spectra due to less than optimal argon interface of the source and high amount of dissolved gases in the solution electrode. That mixture of argon/air atmosphere seems to have decreased the signal to noise ratio of the sodium line tested in that work. Since the mentioned publications[25-26] there has been, to our knowledge, no subsequent literature describing various ambient gases for ELCAD based sources. There is, however, a commercial version of the SCGD developed by Innotech Alberta utilizing an "emission cell" as a means to minimize the influence of atmosphere on the plasma.[27] The SCGD cell developed by Innotech is semi-enclosed, generating an atmosphere free of ambient N_2 by utilizing the high density of evolving solution vapors to eliminate N_2 from the cell.[28]

While there are certainly advantages in terms of operational simplicity by utilizing ELCAD/SCGDs and the LS-APGD in an open environment, there are also several disadvantages. By operating in an open atmosphere, the analyte is subject to react with many species that exist in the atmosphere.[29] While controlling the ambient atmosphere should improve analytical performance from plasma sources, its implementation might be impractical for most ELCADs as it would require the addition of a gas tank, further increasing the complexity of the system. In that respect, LS-APGD-OES is well-suited to test the benefits of atmosphere control as the current apparatus already employs helium as a sheath gas at rates of up to 1 L min^{-1}. The purpose of this study is to evaluate the analytical performance of the LS-APGD-OES by controlling the plasma's ambient environment, hopefully without sacrificing its advantages of small size and simple design. While studies have been done on the influence of the sheath gas identity and rate of the LS-APGD's

analytical performance and fundamental properties, [17,30] there have been none on the influence of extra-plasma environment on analytical performance. Also, various changes to the design of the LS-APGD have been made, such as the inclusion of counter gas flow.[12] It is natural that the existing He gas flows in the LS-APGD could be used to advantage to purge the regions surrounding the plasma. As such, the requirement of gas flow, typically seen as a disadvantage can now be utilized in a positive manner. The results of this study will hopefully further the field-readiness of the LS-APGD-OES, due to improved analytical response and protection from environmental air contamination of the plasma.

6.3 Methods and materials

6.3.1 Instruments

6.3.1.1 Liquid sampling-atmospheric pressure glow discharge

A diagram of the present LS-APGD-OES components is shown in Fig. 6.1. The plasma is sustained between a solution electrode (cathode) composed of a fused silica capillary (i.d = 280 μm, o.d = 580 μm)(Restek, Bellefonte, PA, USA) that is housed inside of a stainless-steel outer capillary (i.d = 500 μm, o.d = 700 μm), and a hollow stainless-steel counter electrode (anode) of the same dimensions. Electrolytic solution, providing conductivity, comprised of 5% v/v nitric acid is pumped through the silica capillary at a rate of 25 μL min−1 by a syringe pump (Fusion 100, Chemyx, Stafford, TX, USA). The discharge is maintained via a constant current power supply (Bertan 915, Spellman, Hauppauge, NY, USA) held at 55 mA. A 10 kΩ ballast resistor is placed in series, between the power supply output and the powered anode. Helium (ultrahigh purity, Airgas, Anderson, SC, USA) sheath gas flows between the fused silica and steel

electrode at a rate of 0.6 L min^{-1} and through the capillary forming the counter electrode at 0.2 L min^{-1}. The plasma is sustained between the solution tip of the inner capillary and the counter electrode, with a gap of 2 mm. A diagram of the electrodes displaying solution flow, He gas flow paths, and the arrangement of the various capillaries is shown in Fig. 6.2a.

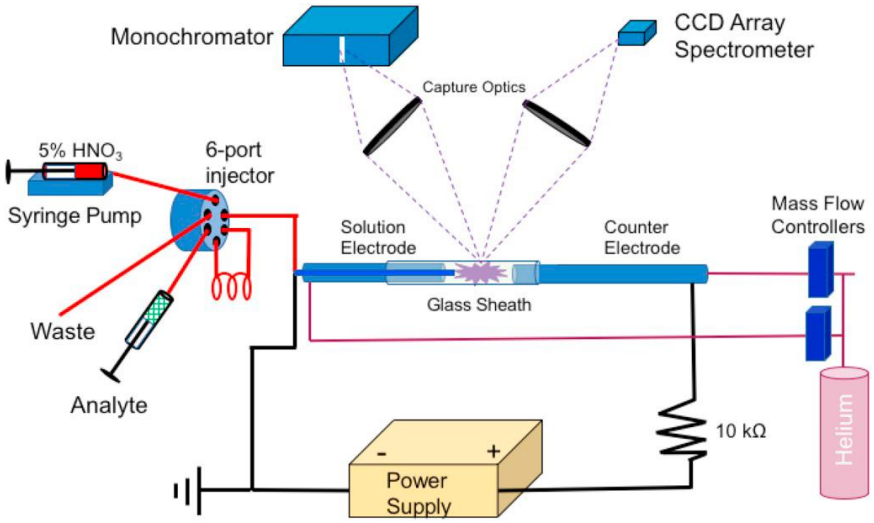

Figure 6.1 A diagrammatic representation of the LS-APGD-OES source components coupled to two different optical spectrometers. Operating conditions are 55 mA, 25 µL min^{-1} solution flow rate, 0.6 L min^{-1} sheath gas flow rate, 0.2 L min^{-1} counter gas flow rate, and 2 mm gap.

6.3.1.2 Plasma sheathing

The plasma is sheathed by an open-ended borosilicate glass tube (i.d. 4 mm, 7 mm o.d.; Kimble Chase, Rockwood, TN, USA). As is typical, the borosilicate glass has a very uniform transmittance value of ~90% across all of wavelengths monitored in these experiment (300–800 nm). In the unsheathed mode, no extra attachment is added to the apparatus as described the previous section. When sheathed mode is engaged, the glass tube is slid over the opposing ends of the two electrodes with an accompanying glass bushing, covering the discharge area. The bushings are utilized to ensure the expansion of

the plasma does not come into contact with the glass sheath. In the case of the glass sheathing with an optical window, a 2 mm diameter diamond tipped drill bit was used to drill a hole into the glass tube. Due to the large inner diameter of the glass tube and the bushing utilized, there is no visual indication that the extends through the hole. Figure 6.2b presents a diagram of the glass-sheathed mode with an optical window. As depicted, the two He gas flows effectively purge the discharge volume so that atmospheric species are not able to ingress the plasma volume. As a reflection of the gross impact of the gas sheathing/purging, Figure 6.2c displays the broadband emission spectra obtained for the cases of the unsheathed (blue line) and sheathed (red line) operating modes.

6.3.1.2 Optical emission spectrometers

A CVI Laser (Digikrom 240, Spectral Products, Putnam, CT, USA) 0.24 m focal length with 1200 grooves mm^{-1} monochromator system equipped with a photomultiplier tube (PMT) (Model R928, Hamamatsu photonics, Bridgewater, NJ, USA) as the detector was employed for moderate-resolution spectral measurements. Emission from the source was focused onto the 50 μm wide entrance slit (20 mm height) of the monochromator by a 50 mm focal length CaF_2 bi-convex lens with a diameter of 25 mm. The lens was placed approximately 100 mm from the plasma and 10 mm from the entrance of the monochromator entrance slit. The image was focused so as to allow the capture emission from the vast majority of plasma volume. Spectral scans were acquired at a rate of 100 nm min^{-1}, with a signal integration time of 6 ms per 0.01 nm wavelength step. The PMT voltage was set to 500 V unless otherwise noted.

A second, array-based spectrometer (Flame, Ocean Optics, Wesley Chapel, FL, USA) was utilized to acquire simultaneous, broadband (wide range) spectra. Source emission was focused by a tube lens assembly, with a 150 mm focal length lens (25.4 mm diameter) capturing the plasma and a 40 mm focal length lens (25.4 mm diameter) focusing the photons onto the entrance of the fiber optics coupled to the spectrometer slit (50 μm wide and 1 mm high). The lens was placed such that the image was focused onto the coupling optic to capture emission from entirety of the plasma. Spectral data was acquired at a rate of 0.1 spectra ms^{-1}. The purpose of utilizing the array – based spectrometer, especially the Flame, is to demonstrate the capability of the excitation source coupled to an inexpensive and portable (89 mm × 64 mm × 32 mm) spectrometer. However, when attempting to quantify the emission response, a monochromator and PMT was utilized to provide a more precise and accurate representation of the analytical responses since the monochromator and PMT has a significantly improved resolution (0.2 nm vs 2 nm).

6.3.2 Materials

6.3.2.1 Chemicals

Concentrated nitric acid (VWR, Atlanta, GA, USA) was subsequently diluted to 5% (v/v) with deionized water (DI-H2O, 18.2 M cm^{-1}) from a water purification system (Purelab Flex, ELGA Waterlab, High Wycombe, UK). All analyte solutions were prepared by dissolving the desired metal nitrate salts (Fisher Scientific, Hampton, NH, USA) in 5% HNO3 to make 500 μg mL^{-1} stock solution of the desired analyte. The desired concentration was reached by diluting the stock solution with 5% HNO_3.

6.3.2.2 Plasma sheathing

The plasma is sheathed by an open-ended borosilicate glass tube (i.d. 4 mm, 7 mm o.d.; Kimble Chase, Rockwood, TN, USA). As is typical, the borosilicate glass has a very uniform transmittance value of ~90% across all of wavelengths monitored in these experiment (300–800 nm). In the unsheathed mode, no extra attachment is added to the apparatus as described the previous section. When sheathed mode is engaged, the glass tube is slid over the opposing ends of the two electrodes with an accompanying glass bushing, covering the discharge area. The bushings are utilized to ensure the expansion of the plasma does not come into contact with the glass sheath. In the case of the glass sheathing with an optical window, a 2 mm diameter diamond tipped drill bit was used to drill a hole into the glass tube. Due to the large inner diameter of the glass tube and the bushing utilized, there is no visual indication that the extends through the hole. Figure 6.2b presents a diagram of the glass-sheathed mode with an optical window. As depicted, the two He gas flows effectively purge the discharge volume so that atmospheric species are not able to ingress the plasma volume. As a reflection of the gross impact of the gas sheathing/purging, Figure 6.2c displays the broadband emission spectra obtained for the cases of the unsheathed (blue line) and sheathed (red line) operating modes.

6.4 Results and discussion

6.4.1 Influence of sheathing on plasma background emission

When a plasma is exposed to ambient air, constituents may interact at the periphery of the plasma and become excited. As such, emission from species such as N_2 and NH from the atmospheric components are seen in the optical spectra. By sheathing

the plasma, it is expected that the glass tubing will be flushed with the He from the sheath/counter gas flows. Thus, the background emission from nitrogen-related species in particular is expected to be substantially reduced. The emission spectrum taken with the array-based spectrometer of the neat 5% HNO_3 electrolytic solution in the unsheathed mode of operation (Fig. 6.2c, blue line) shows the prominent N_2 molecular system extending from ~ 340 to 450 nm, along with responses related to NH and the He sheath gas. Also present are the OH band, and the atomic O(I) and H (I) species, as expected, due to the introduction of the aqueous solution. Upon implementation of the sheathing/purging arrangement, the N_2 and NH bands are seen to decrease substantially (Fig. 6.2c, red line). In raw count terms, those species decrease by ~ 80–90%. On the other hand, the OH band is slightly reduced while the H (I) increases. As those two species are both water originating, the respective changes suggest that the plasma has become more efficient at breaking down the OH to H; inferring that the plasma energetics may be affected in a positive manner by exclusion of ambient atmosphere. This point will be elaborated explicitly in later portions of this report.

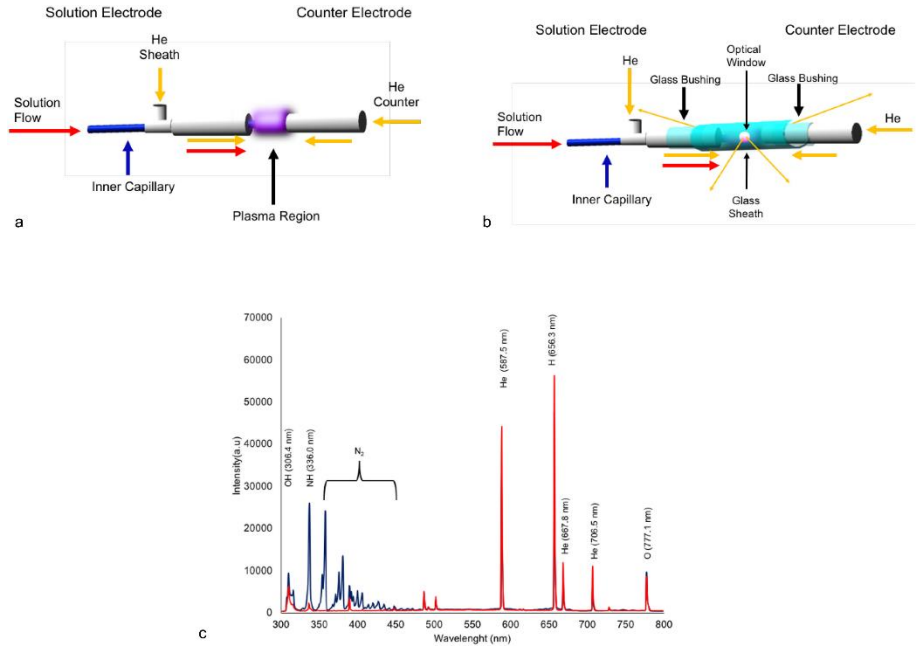

Figure 6.2. Representation of the electrode configuration and solution and gas flow paths for a) unsheathed configuration and b) glass-sheathed configuration. c) Broadband emission spectra depicting the background species present while sampling a 5% HNO_3 solution with the plasma region is unsheathed (blue) and sheathed (red).

The spectra presented in Fig. 6.3 provide a more detailed look at the effects of ambient atmosphere exclusion from the plasma; in all cases, the open source spectra are plotted in blue, and the sheathed case in red. A closer look at the N_2 emission band head (inclusive of the NH radical), Fig. 6.3a, shows a substantial decrease in the N_2 emission. This was anticipated as the plasma region is under continued purging from both the sheath and counter gas flows, thus preventing ambient atmosphere from entering the plasma region. A reduction is also noted for the OH molecular band, Fig. 6.3b. In this case, however, a substantial reduction is not expected as the primary source of OH would arise from the solution flow and not from the atmosphere. Note as well, that in this spectral region, the N2 band component is virtually removed versus the water-related background. The lessened OH response is reconciled by the fact that while the OH band

does decrease, the hydrogen line at 656.5 nm (Fig. 6.3c) increases by ~20%, perhaps reflecting enhanced OH dissociation into its respective constituents. Along with the increased H (I) emission, there was also a slight increase in He (I) emission at 587.5 nm as seen in Fig. 6.3d. In this case, the glass cylinder would tend to confine the He sheath/cooling flows in the vicinity of the plasma. Other plasmas, such as those produced in LIBS, also yield a higher emission intensity, typically for metals, when comparing He to ambient atmospheres.[19,31,32]

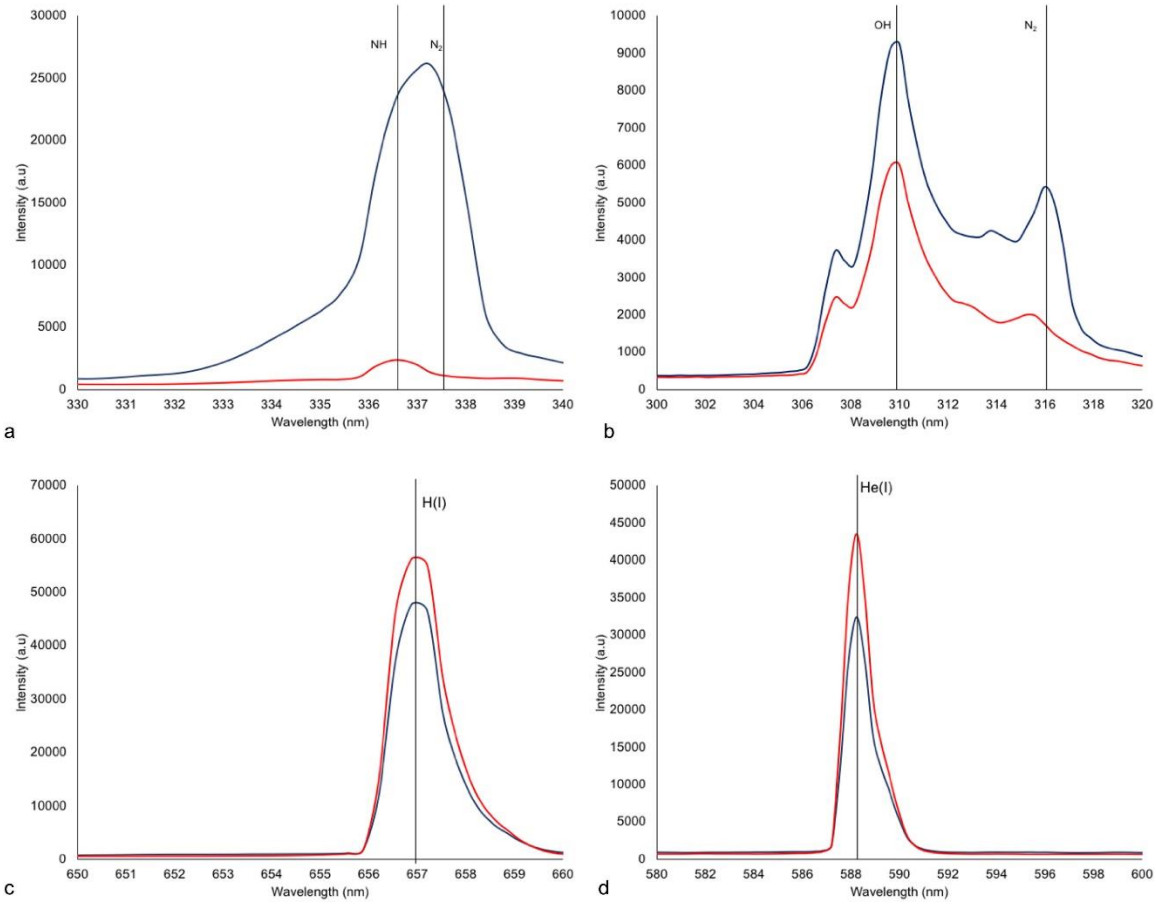

Figure 6.3. Spectral responses of key background species: a) NH and N_2, b) OH and N_2, c) H (I), and d) He (I) under unsheathed (blue) and sheathed (red) conditions while sampling aqueous 5% HNO_3. The array-based spectrometer with a spectral acquisition rate of 0.1 spectra ms^{-1} and a total of 100 recordings was employed

6.4.2 Contamination of the inner glass surface upon introduction of solute-containing solutions.

An obvious consideration when enclosing the plasma volume in close proximity to the evolving solution vapor is condensation on the inner surface of the glass tube. In addition, when injecting solutions containing metal analytes, the vapors containing the metal atoms could deposit onto the inner surface of the glass. As a result of either process, the transmittance from the plasma region through the glass tube will be compromised, thus leading to poor signal recoveries and reproducibility. This phenomenon is demonstrated across a series of sequential 25 μL injections of a 250 μg mL^{-1} Ag solution, with the transient responses monitored using the monochromator system. Table 1 pro-vides comparative data for the case of sheathed plasmas for 10 consecutive injections. For each data set, the responses are reported as a function of the highest observed response for that experimental condition. In the case of the un-sheathed (normal mode) operation, the recoveries vary by only 4.6% RSD, with no appreciable trends in emission response. On the other hand, the responses for the sheathed case decreases continuously (~38%) across the 10 injections, with an overall variation of 14.3% RSD. Clearly, this is an untenable situation.

Solute deposition was confirmed by removal of the material from the inner glass surface and analyzing the wash via ICP-OES. The leaching was accomplished by soaking the glass sheath in a solution of concentrated HNO_3 under light heating for ~ 2 h, then rinsing the glass with concentrated HNO_3. Very clearly, silver-containing condensates/vapors were deposited on the inner glass walls. Additionally, a non-zero

amount of iron was found in the coating on the inside of the glass sheath, suggesting that there may be some degradation of the electrodes occurring during source operation.

Clouding of the sheath glass tubing via solute deposition means that the glass sheath would have to be replaced after each injection, or after extended exposures to the plasma without solute due to potential electrode erosion. While borosilicate glass is not financially expensive, it would be ideal to use the same glass sheath for many injections. To address this problem, a 2 mm diameter hole was drilled into the glass tubing, permitting an open optical path to the spectrometer. To further isolate the viewing region to the open region, the rest of the glass tube was darkened using electrical tape and a marker pen. As demonstrated in the final column of Table 6.1, subsequent injections of the silver test solutions show a repeatability of ~3% RSD, with no clear trends in emission response variations. While there might have been some expectation of restricted optical sampling by limiting the observation volume, that did not occur. Thus, the arrangement of a glass sheath, with a 2 mm hole adjacent to the plasma region, and a blackened outer tubing was adopted for the remainder of the studies.

Table 6.1 Relative responses (100=max in each format) and relative standard deviation (%RSD) for sequential 25 μL injections of a 250 μg mL^{-1} Ag solution for the unsheathed, sheathed and sheathed with an optical sampling window formats. Discharge conditions: current=55 mA, solution flow rate=25 μL min^{-1}, sheath gas flow rate=0.6 L min^{-1}, counter gas flow rate=0.2 L min^{-1}, and 2mm electrode gap.

Trial	Unsheathed	Sheathed	Sheathed/windowed
1	94	100	99
2	91	95	97
3	91	97	95
4	88	91	94
5	85	92	93
6	93	77	94
7	100	73	100
8	99	74	90
9	96	62	93
10	94	63	93
% RSD	4.6	14.3	3.1

6.4.3 Ability to isolate analyte from background emission using the sheathed plasma

Sheathing from the atmosphere should provide a substantial de-crease in molecular background responses from ~300 to 450 nm. This is particularly beneficial as many analytical lines exist within that spectral region, including the 338.3 nm Ag (I) line and 405.7 nm Pb (I) line. To demonstrate the improved spectral clarity for analyte (atomic) transi-tions with the sheath method, broad spectral acquisitions were obtained for injections of 25 μL of 170 μg mL^{-1} Ag, 500 μg mL^{-1} Pb, and 500 μg mL^{-1} Cd using the array-based spectrometer. Again, the purpose of utilizing the Flame array spectrometer is to demonstrate the port-ability of the system (excitation source + spectrometer) as a whole. Not only that, the utilization of the Flame spectrometer demonstrates the efficacy of this sheath method when coupled to a relatively low-re-solution spectrometer (>1 nm). Figure 6.4a-c illustrate the differences in spectral character between sheathed and unsheathed modes when analyzing: Pb (where the

analytical line is engulfed by the N_2 emission band), Cd (where the analytical line exists in a complex background), and Ag (where one analytical line, 328.1 nm, is free of interference while the second analytical line 338.3 nm, is on the shoulder of a N_2 band). In the case of Pb (I) (Fig. 6.4a), the unsheathed emission spectrum (blue) reflects the case where the transition is not identifiable from the N_2 band. However, when sheathed, the Pb line (red) is easily seen and well above the background level. As for Cd (Fig. 6.4b), where the analyte line appears as a shoulder on another transition in the unsheathed case, the peak is resolvable in the case of purging of the excitation volume. Finally, in the case of Ag (Fig. 6.4c), where the two transitions exist in different spectral regions, pronounced changes are seen. In the first instance, the 328.1 nm transition is just-beyond the high energy end of the NH/N_2 system, in a relatively clear spectral region. Even so, changing from the open to sheathed arrangement results in an appreciable increase in S/B. In the second instance, the 338.3 nm transition, which exists within the band N_2 structure, exhibits increased emission response and a lowering of any band contributions. In these two in-stances, both lowering of spectral background and increased analyte emission yield is observed.

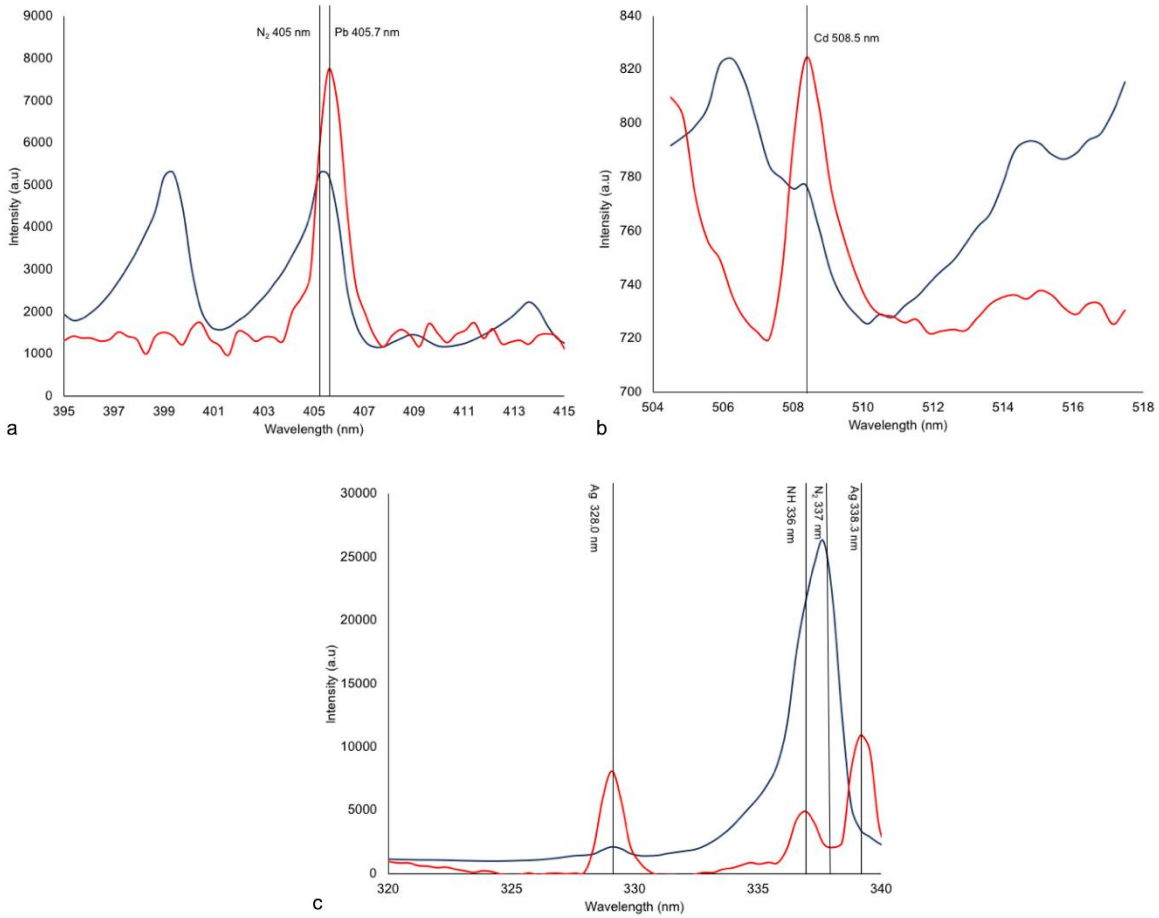

Figure 6.4 APGD-OES spectra obtained from 25 µL injections of a) 500 µg mL^{-1} Pb, b) 500 µg mL^{-1} Cd, c) 170 µg mL^{-1} Ag, under unsheathed (blue) and sheathed (red). All spectra were obtained with the CCD spectrometer at a rate of 0.1 spectra ms^{-1} and a total of 100 recordings.

Of course, one can readily perform spectral background subtraction for those cases, as here, when samples are injected as plugs into a continuous solvent flow; the continuous flow representing the background. As such, it is reasonable to assess the respective qualities of the sheathed system (clarifying spectra in real time), versus post-acquisition mathematical background subtraction. As a demonstration, Fig. 6.5a compares the Pb (I) 450.7 nm transition responses for the case of the sheathed system (red line, same as Fig. 6.4a) and that for the open system wherein the blank (background)

spectrum is subtracted from the case of a Pb injection (green line). As would be anticipated, so long as the background is temporally-stable, the background-subtracted spectrum reveals a clean atomic response. The two instances here show virtually the same analytical responses. Unlike background subtraction however, the sheath method removes background in real time, such that, any fluctuation in the background N_2 spectral contribution is removed in real time as well.

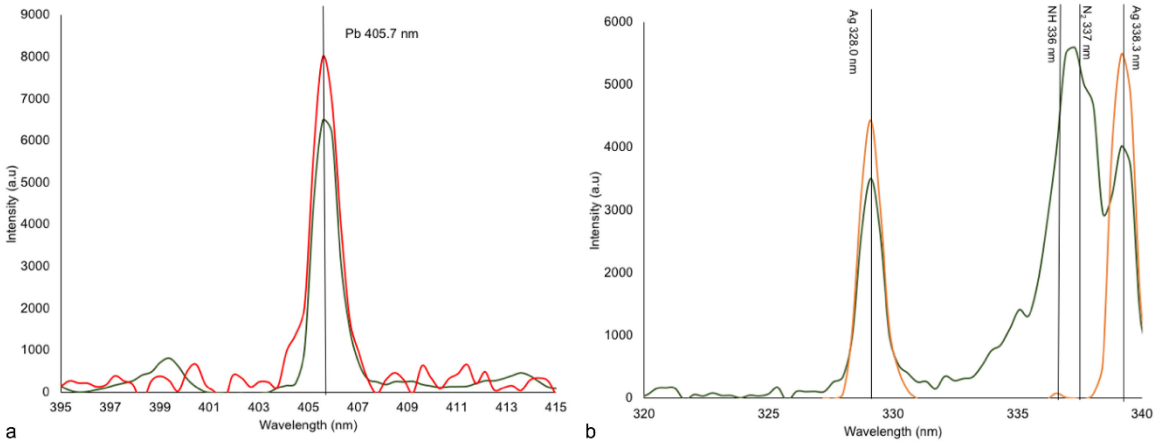

Figure 6.5 Spectra obtained for 25 µL injections of a) 500 µg mL^{-1} Pb for the sheathed (red) and unsheathed with background subtraction (green) and b) 170 µg mL^{-1} Ag unsheathed with background subtraction (green) and sheathed along with background subtraction (orange). All spectra were obtained with the CCD spectrometer at a rate of 0.1 spectra ms^{-1} and a total of 100 recordings.

It is also important to note that some background emissions are not derived from the atmosphere and, as such, are not removed by the glass sheath method. In such cases, the sheath operation can be coupled with background subtraction to eliminate such emission. One example where the background subtraction method may not be suitable is when the intensity of analyte is not significantly higher than the noise of the background. This case is demonstrated in Fig. 6.5b, where a background subtraction is taken of a 170 µg mL^{-1} solution of Ag in the spectral region 320–330 nm (green line). The 338.3 nm analyte line is still slightly obstructed by the N_2 band even after background subtraction

due to the slight deviation of the N_2 emission of the blank. On the other hand, the spectrum for background subtraction of the sheathed plasma, Fig. 6.5b (orange), shows two, clearly-resolved peaks for Ag (I), as any temporal variability associated with N_2 in the open system is significantly reduced by the accompanying reduction of N_2 in region surrounding the atmosphere upon sheathing.

6.4.4 Quantitative aspects of analyte emission using the sheathed plasma

Not only does sheathing the plasma decrease the structured spectral background, it appears to improve analytical response of certain elements even though less light is collected through a smaller window. To determine the differences in sensitivity for various elements, transient measurements (using the monochromator system) were taken and the response area under the curve calculated for 25 μL injections of Ag, Pb, Cd, Na, and Li at 137, 500, 500, 5, 1 μg mL^{-1} respectively. The elements where chosen from work done previously and their diversity in spectrochemical properties. The concentrations were determined empirically and chosen due to reasonable response above the background and without saturation of the detector response at the (admittedly-low) PMT setting. The monochromator was set at 328.0, 405.7, 508.5, 589.0, and 670.7 nm for Ag, Pb, Cd, Na, and Li respectively. The signal was calculated over 1 min, from the start of the injection to its completion, and the average over three trials was taken. The background was calculated as the area within the same time frame during a blank injection of 5% HNO_3. The noise was calculated as the standard deviation of the area of three independent blank injections. From there, a preliminary limit of detection was generated by two different methods. The

IUPAC method utilizes the background equivalent concentration (BEC).[33] The equations are given by;

$$BEC = \frac{S_{Blk}}{S_{analyte} - S_{Blk}}\,[M] \quad \text{(R1)}$$

$$LOD_{BEC} = \frac{3\ x\ BEC\ X\ RSDB}{100} \quad \text{(R2)}$$

where S_{Blk} is the signal of the blank and $S_{analyte}$ is the signal of analyte at the given concentration [M]. The RSDB is the relative standard deviation of the blank. The second method utilized is demonstrated by Boumans et al.[34] The method is described by the given equation.

$$LOD_{Bou} = \frac{(0.01)(3)(RSDB)([M])}{S_{analyte}/S_{Blk}} \quad \text{(R3)}$$

It should be noted that while there is a signal of the blank term in the dominator of Eq.(R1), that has as a related contribution in the RSDB term of Eq. (R3). Thus, the Boumans method does not consider the absolute intensity of the background and the simplified equation can be written as follows:

$$LOD_{Bou} = \frac{(3)(\sigma)([M]}{(S_{analyte})} \quad \text{(R4)}$$

In Eq. (R4), (σ) is the standard deviation of the background. The LOD as determined by Eqs. (R2) and (R4) are shown in Table 6.2 in terms of solution concentration and absolute mass. The LOD values obtained via the BEC are generally higher across all analytes compared to that of the Boumans method for the native plasma. This is due to the over-influ-ence of the background signal in the BEC method. The Boumans method, however, does not consider the absolute signal of the back-ground but rather the relative standard deviations of the background. The stability of the background in the microplasma

leads to the naturally low standard deviation of this parameter and by extension lower LODs. When considering the sheathed plasma state, there are marginal differences in LOD between the two methods because of the significant reduction in the signal of the spectral background.

Table 6.2 LOD in concentration (μg mL^{-1}) and mass (μg) based on Eq. (2) (BEC) and Eq. (4) (Boumans) for the case of open and sheathed LS-APGD-OES plasmas. Discharge conditions: current=55 mA, solution flow rate=25 μL min^{-1}, sheath gas flow rate=0.6 L min^{-1}, counter gas flow rate=0.2 L min^{-1}, 2mm electrode gap, n=3 injections.

Element	LOD_{BEC} Open	LOD_{BEC} Sheathed/Windowed	LOD_{Bou} Open	LOD_{Bou} Sheathed/ Windowed
Ag (μg mL^{-1})	30	4	1	3.1
(μg)	0.7	0.1	0.3	0.08
Pb (μg mL^{-1})	200	0.6	8	0.5
μg	6	0.01	0.2	0.01
Cd (μg mL^{-1})	10	9	3	4
μg	0.3	0.2	0.07	0.08
Na (μg mL^{-1})	0.005	0.08	0.003	0.03
μg	0.0001	0.002	0.00008	0.0008
Li (μg mL^{-1})	0.01	0.02	0.004	0.08
μg	0.0001	0.0004	0.0001	0.0002

When discussing the LOD determined by BEC method, there was an order of magnitude improvement in LOD for Ag and Cd in the case of the sheathed plasma, a three orders improvement for Pb, and an actual increase in LOD for both Na and Li. The tremendous improvement for Pb is expected due to the disappearance of the overlapping nitrogen peak (Fig 6.4a) through the use of glass sheathing, improving both the intensity of the Pb line and reducing the blank signal that arises from the nitrogen band emission. Similarly, the Ag and Cd atomic transitions experience a slight increase in intensity while also seeing a slight de-crease in background. While the exact mechanism for improved analytical performance is the subject of future investigation, there are a few possible

explanations. One possibility is that with confinement of gas, both the pressure and kinetic temperature increase, yielding more atoms in the excited state according to the Boltzmann equation. Also, the reduction of N_2 species means that there are fewer quenching probabilities on the periphery of the plasma, leading to a increase in signal response. Meanwhile, the signal intensity for both Na and Li are reduced by more than a factor of 2 leading to a higher LODs. The possible causes of this phenomena is discussed in a later paragraph.

The LODs as determined by the Boumans method also show improvements for Pb and Ag when the plasma is sheathed. Referring to Eq. (3), the signal of background is not a contributor to the LOD, thus the only differences are mostly likely due to improved excitation conditions and greater temporal stability. Interestingly, the LOD of Cd appears to be unchanged when utilizing Boumans equation suggesting that the LOD improvement of Cd from the BEC-based equation is due to the reduction in spectral background, and the slight increase in analyte intensity noted was not statistically significant. The signifance was determined using a two-sample t-test, with the hypothesis that the two intensities are equal with 99% confidence. Similar to that of the LOD determined though the BEC-based equation, the LOD for both Na and Li increased significantly employing Boumans equation due to a decrease in signal intensity of the analyte lines.

There could be multiple explanations as to why Na and Li emission responses are diminished while other elements tested increased. Both Na and Li are easily excitable/ionizable elements relative to that to Ag, Pb, and Cd. Thus, an increase in excitation conditions leads to a higher percentage of Na and Li becoming ionized, thus the

intensity of the neutral atomic transitions decreased. Interrogation at Na (II) and Li (II) wavelengths, 328.6 and 548.4 nm respectively, did not reveal appreciable emission above background levels in either case. The decrease in signal of Na and Li could potentially arise from the fact that different elements have different spatial emission profiles, as seen in an ELCAD-type excitation sources.[35,36] Due to this characteristic, the optical window created may have been selectively decreasing the capture angle of certain elements. In particular, Na potentially has a narrower spatial profile and emits closer to the solution cathode thus less light is captured from the emitting Na atoms.[35,36] Of course, further studies are required to deconvolute the specific reason for diminished Na and Li response, such as acquiring spatially resolved emission profiles of all the elements tested. In the end, though, the LODs realized for the alkali metals are still well below those of the other test elements.

It must be noted that the results presented here are contradictory to the study by Piepmeier et al., who showed that the emission intensity of metals was independent of the atmosphere in ELCAD. Piepmeier determined that this was due to the saturation of the cathode surface by water vapors, essentially to the exclusion of ambient gases. The LS-APGD, however, is vastly different in terms of operating conditions. Unlike Piepmeier's ELCAD, the solution flow rate is substantially lower (10 mL min^{-1} vs 25 μL min^{-1}), and gas flow higher (100 mL min^{-1} vs 600 mL min^{-1}). Thus, the saturation of cathode surface covered by water vapors cannot be assumed for the LS-APGD. In fact, the spectra between ~ 300 nm to 400 nm shows a small OH signal, relative to N_2 response, in comparison to the opposite case in Piepmeier's work.

6.5 Conclusion

The LS-APGD has many characteristics that make it an ideal instrument to address several current analytical challenges. Its small size, low resource consumption, and robustness make it a truly portable source for in-field or online analysis. When paired with an OES system, these advantages begin to shine and the capability of a completely portable system that can be taken to remote locations is demonstrated. While there are advantages in terms of portability and resource consumption, the LS-APGD-OES's analytical performance is relatively weaker than that of an ICP-OES. This present study focused on improving analytical performance by alleviating the influence of ambient air on the plasma, both in terms of background spectral complexity and discharge robustness. The improvements in spectral quality open the way for the use of compact, array-type optical spectrometers; thus the goal of portability is reinforced. The work shows improvement in two ways; by significantly reducing the atmospheric background and al-lowing for resolution of analytical lines without the need for increased spectrometer cost or post-acquisition background subtraction, and by increasing the emission intensity of certain analytes, which lowered their respective LODs. Unfortunately, easily ionizable elements de-creased in signal intensity when utilizing the sheath method and an increase in LOD is noted; though still at levels which are far below the transition metals. Coincidentally, the requirement of a sheath gas, once considered a disadvantage, was turned into an advantage by allowing for a controlled environment.

Future fundamental studies will determine the exact mechanisms by which these improvements and diminishment occurred. Surely, there are a multitude of effects that play

into the improved analytical performance, such as increased temperature and electron density. By utilizing a higher resolution spectrometer, the difference in electron density and kinetic temperature between sheathed and un-sheathed plasma can be determined by monitoring H_β emission and the OH molecular band. Combining the sheathed plasma with preconcentration methods could also improve the sensitivity of the LS-APGD-OES to push toward being as a truly portable device for qualitative and quantitative elemental analysis.

6.6 Acknowledgements

This work was supported by the Defense Threat Reduction Agency, Basic Research Award #HDTRA1-14-1-0010, to Clemson University.

6.7 References

1. G. L. Donati, R. S. Amais and C. B. Williams, *J. Anal. At. Spectrom.*, 2017, **32**, 1283-1296.
2. D. Beauchemin, *Anal. Chem.*, 2010, **82**, 4786-4810.
3. V. Karanassios, *Spectrochim. Acta B*, 2004, **59**, 909-928.
4. P. Jamroz, K. Greda and P. Pohl, *Trac-Trend Anal. Chem.*, 2012, **41**, 105-121.
5. T. Cserfalvi, P. Mezei and P. Apai, *J. Phys. D Appl. Phys.*, 1993, **26**, 2184-2188.
6. P. Mezei and T. Cserfalvi, *Appl. Spectrosc. Rev.*, 2007, **42**, 573-604.
7. M. R. Webb and G. M. Hieftje, *Anal. Chem.*, 2009, **81**, 862-867.
8. A. J. Schwartz, K. L. Williams, G. M. Hieftje and J. T. Shelley, *Anal. Chim. Acta*, 2017, **950**, 119-128.
9. R. K. Marcus and W. C. Davis, *Anal. Chem.*, 2001, **73**, 2903-2910.
10. W. C. Davis and R. K. Marcus, *J. Anal. At. Spectrom.*, 2001, **16**, 931-937.
11. R. K. Marcus, C. D. Quarles, C. J. Barinaga, A. J. Carado and D. W. Koppenaal, *Anal. Chem.*, 2011, **83**, 2425-2429.
12. R. K. Marcus, B. T. Manard and C. D. Quarles, *J. Anal. At. Spectrom.*, 2017, **32**, 704-716.
13. R. K. Marcus, C. Q. Burdette, B. T. Manard and L. X. Zhang, *Anal. Bioanal. Chem.*, 2013, **405**, 8171-8184.
14. H. W. Paing and R. K. Marcus, *J. Anal. At. Spectrom.*, 2017, **32**, 931-941.
15. A. J. Carado, C. D. Quarles, Jr., A. M. Duffin, C. J. Barinaga, R. E. Russo, R. K. Marcus and D. W. Koppenaal, *J. Anal. At. Spectrom.*, 2012, 27, 385-389.
16. C. D. Quarles, J. Gonzalez, I. Choi, J. Ruiz, X. L. Mao, R. K. Marcus and R. E. Russo, *Spectrochim. Acta B*, 2012, **76**, 190-196.
17. W. C. Davis and R. K. Marcus, *Spectrochim. Acta B*, 2002, **57**, 1473-1486.
18. S. Reuter, J. Winter, A. Schmidt-Bleker, H. Tresp, M. U. Hammer and K. D. Weltmann, *Ieee T. Plasma Sci.*, 2012, **40**, 2788-2794.
19. A. J. Effenberger and J. R. Scott, *Sensors-Basel*, 2010, **10**, 4907-4925.
20. L. St-Onge, E. Kwong, M. Sabsabi and E. B. Vadas, *Spectrochim. Acta B*, 2002, **57**, 1131-1140.
21. C. K. Williamson, R. G. Daniel, K. L. McNesby and A. W. Miziolek, *Anal. Chem.*, 1998, **70**, 1186-1191.
22. C. D. Quarles, J. J. Gonzalez, L. J. East, J. H. Yoo, M. Morey and R. E. Russo, J. *Anal. At. Spectrom.*, 2014, **29**, 1238-1242.
23. G. Asimellis, S. Hamilton, A. Giannoudakos and M. Kompitsas, *Spectrochim. Acta B*, 2005, **60**, 1132-1139.
24. A. Khumaeni, M. Miyabe, K. Akaoka and I. Wakaida, *J. Radioanal. Nucl. Ch.*, 2017, **311**, 77-84.
25. Y. S. Park, S. H. Ku, S. H. Hong, H. J. Kim and E. H. Piepmeier, *Spectrochim Acta B*, 1998, **53**, 1167-1179.
26. G. Jenkins, J. Franzke and A. Manz, *Lab Chip*, 2005, **5**, 711-718.
27. CA Pat., US 9989472, 2018.
28. S. Schroeder, Reno, NV 2017.

29. A. Schuetz, F. J. Lara-Ortega, F. D. Klutet, S. Brandt, M. Schilling, A. Michels, D. Veza, V. Horvatic, J. F. Garcia-Reyes and J. Franzke, *Anal. Chem.*, 2018, **90**, 3537-3542.
30. S. Konegger-Kappel, B. T. Manard, L. X. Zhang, T. Konegger and R. K. Marcus, *J. Anal. At. Spectrom., 2015, **30**, 285-295.*
31. Y. Lida, *Spectrochim. Acta B*, 1990, **45**, 1353-1367.
32. J. A. Aguilera and C. Aragon, *Appl. Phys. a-Mater*, 1999, **69**, S475-S478.
33. F. V. Silva, L. C. Trevizan, C. S. Silva, A. R. A. Nogueira and J. A. Nobrega, *Spectrochim. Acta B*, 2002, **57**, 1905-1913.
34. P. W. J. M. Boumans, *Anal. Chem.*, 1994, **66**, A459-A467.
35. A. J. Schwartz, S. J. Ray, G. C. Y. Chan and G. M. Hieftje, *Spectrochim. Acta B*, 2016, **125**, 168-176.
36. P. Mezei, T. Cserfalvi and L. Csillag, *J Phys D*, 2005, **38**, 2804-2811.

CHAPTER VII

SUMMARY

7.1 Summary

The liquid sampling – atmospheric pressure glow discharge (LS-APGD) microplasma has been studied extensively and applied towards a diverse array of analytical challenges. While tremendous efforts have been made towards both the application and fundamental study of the LS-APGD for aqueous samples, many fundamental questions remained for direct solid sampling since the initial demonstrations of the LS-APGD for ambient desorption (AD) – mass spectrometry MS,[1] AD – optical emission spectrometry (OES),[2] and laser ablation (LA) – LS-APGD-OES/MS.[3, 4] The advantages of solid sampling modalities for the LS-APGD are outlined in Chapter I. Some key points include the reduced solvent usage, increased throughput, and higher detectability that arises from elimination of the digestion step. This dissertation expands the current LS-APGD analytical capabilities as well as understandings and hoped to set up the stage for further solid sampling analysis utilizing the LS-APGD.

Efforts made to parameterize AD-LS-APGD-OES is presented in Chapter II. Through parameterization, sensitivity was improved 6-fold and reproducibility was improved 4-fold. Table 2.2 presents the improved parameters from the initial demonstration of LS-APGD-OES. Beyond improved analytical performance, Chapter II also described the heavy influence of solvent flow rate and identity on analytical performance, indicating a potential solvent-based desorption mechanism that made desorption of bulk metal possible at relatively low temperatures. This also expands on the

desorption mechanism proposed by Marcus *et al.* for AD-LS-APGD.[1] One major challenge of solid sampling when attempting to analyze residues is the spread of analyte beyond the sampling area. This is exacerbated by the fact that the aliquots typically dry in a non-uniform matter, consequently making quantitative analysis of residues problematic. Chapter III describes the effect of this non-uniformity as well as describing the means of controlling and visualizing the residues. With co-addition on food dyes in residue preparation, visualization of residues becomes trivial while not diminishing the analytical response. It is demonstrated in Chapter III that the utilization of hydrophobic substrates improved the uniformity and size of the residues (*i.e.* smaller residues), leading to improved sensitivity by an order of magnitude. In addition to AD – OES, the LS-AGPD sampling method of solvent extraction (Chapter IV) and LA (Chapter V) were examined. The coupling of an Advion Plate Express (PE) as a solid sampling step for samples to be ionized by the LS-APGD in the aqueous phase was presented in Chapter IV. This sampling modality was particularly useful when analyzing samples whose structure is prone to degradation from heat. This effect is partially described in Chapter III during the degradation of PTFE sheets. It was determined in Chapter IV that an extraction time of at least 30 seconds is needed for the complete extraction of uranium from cotton swipes. While intrasample variability in terms of analytical response is high (~ 30% RSD), it is offset by the capability to determine isotope ratios with precision better than 10% RSD and with absolute errors falling below 10%. The main analytical merit of this technique is the capability to acquire the uranium isotope ratio from a sample in less than 5 minutes, compared to the hours required for current MS isotope ratio analysis methods. To take

advantage of solid sampling's capability to discern spatial information, LA was coupled to the LS-APGD for the simultaneous acquisition of atomic, molecular, and spatial information in Chapter V. A key concept in simultaneous detection of atomic and molecular species was described, whereby the interelectrode gap must be tuned between "soft" and "hard" ionization. A map of organic (molecular) and inorganic (elemental) species was generated from both residues and biological samples to demonstrate the capability of simultaneous atomic, molecular, and spatial determination. A contribution to the analysis of aqueous samples via LS-APGD was described in Chapter VI. It is demonstrated that a reduction of background atmospheric species is achieved via sheathing of the plasma with a simple borosilicate glass. With the reduction of the background, improvements in terms of LOD for the elements Ag, Pb, and Cd are noted while elements Na and Li performed worse, possibly due to their spatial emission profile.

7.2 Outlook

The research presented in this dissertation expands the analytical portfolio of the LS-APGD for direct solid sampling as well as provides insight into a potential mechanism of sampling. Questions still remain in terms of mechanisms and potential applications. Regarding AD-LS-APGD, a question that can be asked is whether the solvent interaction mechanism can be exploited for higher selectivity towards certain applications. Moreover, it would be imperative to examine the AD – LS - APGD on a variety of analytes and substrates. The AD-LS-APGD provides substantial benefits in terms of low resource consumption and low footprint. In that aspect, coupling the AD-LS-APGD to a portable mass spectrometer could yield an analytical technique that can acquire a high density of

information for a small instrument. In terms of PE-LS-APGD, substantial analytical improvements can be envisioned via the optimization of the sampling process through a coupled Design-of-Experiment interrogation of the PE and LS-APGD plasma operating conditions. While Chapter IV was targeted towards nuclear non-proliferation, the use of swipes for analysis is ubiquitous throughout the analytical world, and one can envision the utilization of PE-LS-APGD for general-purpose analyses. Chapter V set the stage for a comprehensive imaging technique, but a multitude of questions remains in terms of understanding the process of ionizing laser-ablated particles. The pivotal role of the solvent vapors also remains in question. Of course, in terms of applications there are vast possibilities that have yet to be explored. As the field of analytical chemistry trends towards smaller and greener analytical tools, solid sampling techniques are becoming increasingly in demand.[5-8] The LS-APGD operating in a solid sampling modality could be a seminal instrument for these challenges.

7.3 References

1. R. K. Marcus, C. Q. Burdette, B. T. Manard and L. X. Zhang, *Anal. Bioanal. Chem.*, 2013, **405**, 8171-8184.
2. R. K. Marcus, H. W. Paing and L. X. Zhang, *Anal. Chem.*, 2016, **88**, 5579-5584.
3. A. J. Carado, C. D. Quarles, A. M. Duffin, C. J. Barinaga, R. E. Russo, R. K. Marcus, G. C. Eiden and D. W. Koppenaal, *J. Anal. At. Spectrom.*, 2012, **27**, 385-389.
4. C. D. Quarles, J. Gonzalez, I. Choi, J. Ruiz, X. L. Mao, R. K. Marcus and R. E. Russo, *Spectrochim. Acta B*, 2012, **76**, 190-196.
5. R. C. Machado, D. F. Andrade, D. V. Babos, J. P. Castro, V. C. Costa, M. A. Speranca, J. A. Garcia, R. R. Gamela and E. R. J Pereira, *J. Anal. At. Spectrom.*, 2020, **35**, 54-77.
6. C. Bendicho, I. Lavilla, F. Pena-Pereira and V. Romero, *J. Anal. At. Spectrom.*, 2012, **27**, 1831-1857.
7. S. Garrigues and M. de la Guardia, *Trac-Trend Anal. Chem.*, 2013, **43**, 161-173.
8. M. Koel, Green Chem, 2016, 18, 923-931.